Nonlinear Fluid-Structure Interaction in a Flexible Shelter under Blast Loading

Sangeon Chun

Dissertation submitted to the Faculty of the
Virginia Polytechnic Institute and State University
in partial fulfillment of the requirements for the degree of

Doctor of Philosophy
in
Aerospace Engineering

Dr. Rakesh K. Kapania, Chair
Dr. William Mason
Dr. Raymond H. Plaut
Dr. Joseph A. Schetz
Dr. Elaine P. Scott
Dr. Danesh K. Tafti

November 12, 2004
Blacksburg, Virginia

Keywords: Fluid-Structure Interaction, Finite Element Analysis, Computational Fluid Dynamics, Blast Loading, Blast Wave Propagation, Membrane Analysis

Nonlinear Fluid-Structure Interaction in a Flexible Shelter under Blast Loading

By

Sangeon Chun

ABSTRACT

Recently, numerous flexible structures have been employed in various fields of industry. Loading conditions sustained by these flexible structures are often not described well enough for engineering analyses even though these conditions are important. Here, a flexible tent with an interior Collective Protection System, which is subjected to an explosion, is analyzed. The tent protects personnel from biological and chemical agents with a pressurized liner inside the tent as an environmental barrier. Field tests showed unexpected damage to the liner, and most of the damage occurred on tent's leeward side.

To solve this problem, various tests and analyses have been performed, involving material characteristics of the liner, canvas, and zip seals, modeling of the blast loading over the tent and inside the tent, and structural response of the tent to the blast loading as collaborative research works with others. It was found that the blast loading and the structural response can not be analyzed separately due to the interaction between the flexible structure and the dynamic pressure loading. In this dissertation, the dynamic loadings imposed on both the interior and the exterior sides of the tent structure due to the airblasts and the resulting dynamic responses were studied. First, the blast loadings were obtained by a newly proposed theoretical method of analytical/empirical models which was developed into a FORTRAN program. Then, a numerical method of an iterative Fluid-Structure Interaction using Computational Fluid Dynamics and Computational

Structural Dynamics was employed to simulate the blast wave propagation inside and outside the flexible structure and to calculate the dynamic loads on it.

All the results were compared with the field test data conducted by the Air Force Research Laboratory. The experimental pressure data were gathered from pressure gauges attached to the tent surfaces at different locations. The comparison showed that the proposed methods can be a good design tool to analyze the loading conditions for rigid or flexible structures under explosive loads. In particular, the causes of the failure of the liner on the leeward were explained. Also, the results showed that the effect of fluid-structure interaction should be considered in the pressure load calculation on the structure where the structural deflection rate can influence the solution of the flow field surrounding the structure.

DEDICATION

To Heejin, my wife, Yo-On, my first daughter, So-On, my second daughter and Christ Jesus, my guard.

ACKNOWLEDGMENTS

I would like to express my sincere gratitude and appreciation to my advisor, Prof. Kapania, for his guidance and advice over years of my research and study. I am grateful for his support and for giving me the opportunity to be involved in many important projects. His encouragement, thoughtfulness, and supervision are deeply acknowledged. He will always be my guru.

I would also like to thank Dr. Plaut for valuable guidance, constructive ideas, and generosity in sharing his knowledge in this research. Above all, he showed me invaluable examples as teacher, research engineer, and person. I am very grateful to Dr. Schetz for his encouraging discussions and advice in this research. I learned a lot on unsteady aerodynamics from personal meetings. I would also like to thank Dr. Mason for his support and for giving me the opportunity to study at Virginia Tech. His teaching of configuration design and service on my committee were a valuable guidance and discipline for me to study here. I would also like to thank Dr. Scott for serving on my committee. I would also like to thank Dr. Tafti for sharing his knowledge and guidance in the field of CFD. I would also like to thank the Air Force Research Laboratory for the project, “Modeling the Response of Collective Protection Systems to Airblasts”, Grant No. F5ESCW234401, which allowed me to work on this topic of research. I would like to thank Hitesh Kapoor and Michael Motley for their collaborative work on this research.

Finally, I would like to express my deep appreciation to my beloved wife, Heejin, for her unconditional help, sacrifice and patience. I am forever grateful to my family and parents for their love and support. Finally, I would like to express my deep appreciation to my beloved wife, Heejin, for her unconditional help, sacrifice and patience. I am forever grateful to my parents, mother-in-law, brothers, sister, and relatives for their love

and support. I would also like to thank all my friends and their families in the Korean Blacksburg Baptist Chruch for their fellowships, support and encouragement.

Table of Contents

List of Tables

List of Figures

List of Symbols

a_0	The Speed of sound in the ambient atmosphere
a_r	The speed of a reflected shock
a_{refl}	Velocity of sound in reflected region
b	Decay coefficient as shown in Equation (2.16)
$[C]$	damping matrix
C_D	Local drag coefficient
C_j	Parameter in Equation (2.11)
D	Characteristic dimension as shown in Figure 2.3
E	Total energy of the explosive charge
$\{\mathrm{F}(t)\}$, $\{\mathrm{F}\}$	Applied load vector
F_x, F_y	Elastic forces due to in-plane deformation as shown in Figure 4.2
F_z	Bending force due to out-of-plane deformation relative to the neighboring nodes as shown in Figure 4.2
h or h'	Clearing height
I	Specific impulse defined by Kingery and Bulmash as shown in Equation (2.16) and in Figure 2.3

i_r	The magnitude of impulses in the reflected region in Figure 2.7
$[K]$	Stiffness matrix
K_j	Parameter in Equation (2.12)
L_{eo}	The initial element length
$[M]$	Mass matrix
M_x, M_y	Bending moments due to out-of-plane deformation relative to the Neighboring nodes as shown in Figure 4.2
N	Order of the polynomial fit through the data in Equation (2.11)
P_0	Ambient (or reference) pressure as shown in Figure 2.1
P_{l0}	Leeward-side peak overpressure
P_{qs}	Peak quasi-static overpressure
P_r	Reflected overpressure
P_{r0}	Reflected peak overpressure
P_s	Side-on overpressure
$P_s(t)$	Side-on pressure profile as shown in Figure 2.1
P_{s0}	Side-on peak overpressure (Amplitude) as shown in Figure 2.1 and Figure 2.3

P_{st}	Standard atmospheric sea-level pressure
q	Dynamic pressure
Q_1	Reference weight of one kilogram in Equations (2.6) - (2.9)
Q_2	Explosive mass (in kilograms) in Equations (2.6) - (2.9)
R	Distance from the origin of an detonation to a measuring point
R, S	Parameter introduced in Modified Friedlander's equation shown in Equation (2.18)
$\mathrm{RF}_{\mathrm{estimated}}$	Error function for the estimated reduction factors defined in Equation (2.19)
$\mathrm{RF}_{\mathrm{measured}}$	Error function for the measure reduction factors defined in Equation (2.20)
S_d	Scaling factor as defined in Equation (2.6)
S_i	Impulse scaling factor as defined in Equation (2.9)
S_p	Reciprocal of a pressure scaling factor as defined in Equation (2.8)
S_t	Reciprocal of a time scaling factor as defined in Equation (2.7)
T	Natural logarithm of the scaled distance in Equation (2.12)
t	Time as shown in Figure 2.1
t_0	Duration of the positive overpressure on the wall as shown in Figure 2.1 and Figure 2.3

T_{st}	Standard atmospheric temperature (288 K)
T_0	Ambient temperature in degrees K
t_a	Time when a blast wave arrives at a measuring point as shown in Figure 2.1
t_c	Time for clearing reflection effect
t_r	Duration time for reflected overpressure
$\{u\}$	Nodal displacement vector
$\dot{u}$	Nodal velocity
$\ddot{u}$	*N*odal acceleration
u, v	In-plane deformation in a local x-y-z axis system as shown in Figure 4.2
w	Out-of-plane deformation in a local x-y-z axis system as shown in Figure 4.2
Y	Natural logarithm of the parameter under evaluation in Equation (2.11)
$\dot{Y}_e$	Node velocity
Z	Scaled distance defined in Equation (2.2)
α, αi	Angle of incidence as defined in Figure 1.2

α_A	Angle of incidence at an arbitrary location on the front side as shown in Figure 1.2
α_B	Angle of incidence at an arbitrary location where angle of incidence is zero as shown in Figure 1.2
α_C	Angle of incidence at an arbitrary location on the the rear side as shown in Figure 1.2
γ	The ratio of specific heats
θ	Clockwise angle from horizon to the arbitrary location as defined in Figure 2.5
θ_x, θ_y	Rotational components used for out-of-plane deformation as shown in Figure 4.2
θ_z	Drilling degree of freedom rotational component used for coplanar deformation as shown in Figure 4.2
Θ	Modified decay coefficient as defined Equation (2.15)
λ	Length scale factor as shown in Figure 2.3
$\{\}^P$	In-plane action items
$\{\}^B$	Bending action items

Abbreviations

ALE	Arbitrary Lagrangian Eulerian
BKW	Becker-Kistiakowsky-Wilson
CCM	Computational Continuum Mechanics
CEL	Coupled Eulerian-Lagrangian
CFD	Computational Fluid Dynamics
CFL	Courant-Friedrich-Lewy
Comp. B	Composition B
CONWEP	Conventional Weapon Effects
CPS	Collective Protection System
CSD	Computational Structural Dynamics
CSM	Computational Structural Mechanics
CST	Constant stress-strain triangular element
DG	Discontinuous Galerkin
DKT	The Discrete-Kirchhoff Theory
DOF	Degree of Freedom
EFS	Elastic foundation stiffness

ENO	Essentially NonOcillatory
FCT	Flux-Corrected Transport
FDM	Finite Difference Method
FEM	Finite Element Method
FVM	Finite Volume Method
FSI	Fluid-Structure Interaction
HE	High Explosion
HMX	High Melting Explosive
HOB	Height of Burst
IDLH	One-Dimensional Lagrangian Hydrodynamics
IVP	Initial Value Problem
JWL	Jones-Wilkins-Lee
LAMS	Large-Area Maintenance Shelter
NATO	North Atlantic Treaty Organization
PDE	Partial Differential Equation
RDX	Rapid Detonating Explosive
SSS	Small Shelter System

TEMPER	Tent Extendable Modular Personnel
TNT	Trinitrotoluence
UAV	Unmanned Air Vehicles
UNHCR	The United Nations High Commisioner for Refugees
WENO	Weighted Essentially NonOcillatory
XM28	a type of material used in the collective protection system for the liner

Chapter 1
Introduction

1.1 Introduction

Recently, numerous flexible structures have been employed in various fields of industry.[1-5] An inflatable, lightweight, deployable shelter- or tent-type structure is an example which is used for both governmental and civilian facilities in various forms: temporary housing for people[6], emergency military hospital units[7] to protect people from hazardous conditions, transportable hangers[8] for aviation maintenance, *etc*. Cold-climate refugee tents[6] of the United Nations High Commissioner for Refugees (UNHCR), Tent Extendable Modular Personnel[7] (TEMPER), Small Shelter System[7] (SSS), and Large-Area Maintenance Shelter[8] (LAMS) under development by the U.S. Army are four tent-type structures currently used due to their low costs, high portability, and quick deployment. Most of these flexible structures can be described as a closed structure consisting of a flexible membrane (*i.e.,* fabric skin) supported over a solid frame. For these structures, dynamic loadings and the ensuing dynamic responses can be very important criteria for an efficient structural design.

Therefore, experimental and computational methods to analyze dynamic responses of flexible structures have been developed (see Section 1.2.3). However, in many cases where flexible tent-type structures are deployed, there is a lack of analytical methodology for engineers to understand and estimate the physical phenomena of blast loadings on flexible structures, which is one of the most important dynamic loadings and should be clearly defined qualitatively and quantitatively. This need for an analytical methodology encouraged the author to examine the current methods for defining and estimating blast loading, and to develop a new methodology for estimating the effects of such loading on flexible tent-type structures.

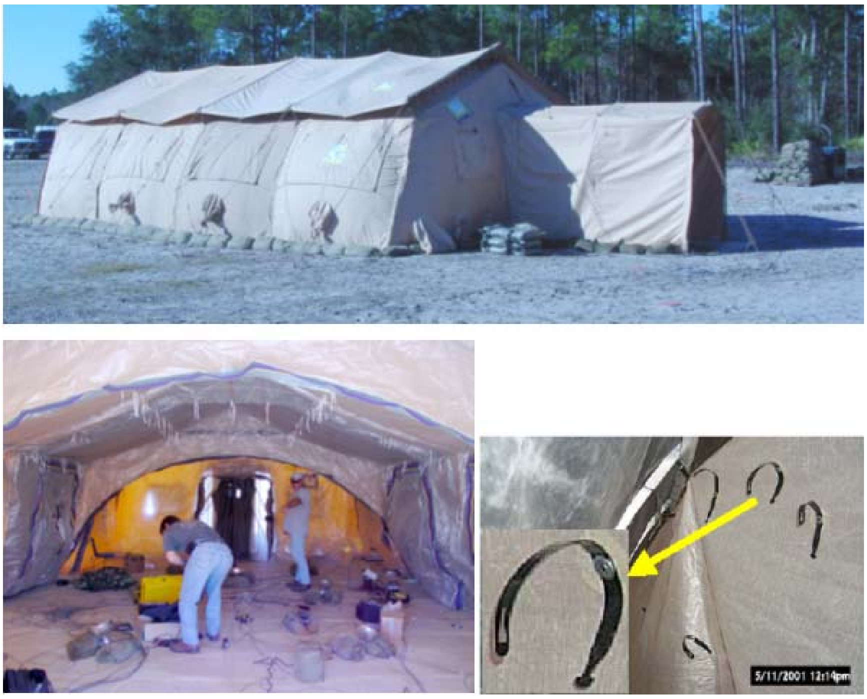

Figure 1.1 A Temper tent with CPS: (i) a typical TEMPER tent, (ii) XM28 liner, (iii) plastic straps with arrowhead type connectors, counterclockwise from top.

The specific case under consideration in this work is a TEMPER tent with a Collective Protection System[7] (CPS), which is a protective system from attacks by chemical and biological warfare agents (Figure 1.1). The CPS consists of an XM28 liner system and a filtered ventilation system. The XM28 liner system has 16-foot-long center sections, end sections, and entry vestibules, that are joined by airtight zip-type seals.[7] Each section has windows, opened and closed by the same zip-type seal on both sides (Figure 1.1). Plastic straps with arrowhead-type connectors are riveted to the outside of the liner and are attached to the tent frame to hold the liner up when it is not inflated by the ventilation system (Figure 1.1).[7] The filtered ventilation system supplies toxin-free air inside the liner and maintains a positive pressure slightly higher than the surrounding atmospheric pressure outside the tent.[7] This higher pressure prevents flow of contaminated air into the liner.[7] When this TEMPER tent was subjected to an external explosion, the XM28 liner material was severely ripped open in some locations, in addition to the partial or complete failure of the window zip-seals, nullifying the protective function of the CPS, even though the tent structure maintained its shape with insignificant damage.

To solve this problem, various tests and analyses have been performed, involving such as material characteristics of the liner, canvas, and zip seals, modeling of the blast loading over the test and the resulting dynamic pressure loading inside the tent, transient analysis of structural response of the tent to the blast loading as collaborated research works with others[9]. It was found that the blast loading and the structural response can not be analyzed separately due to the interaction between the flexible structure and the dynamic pressure loading. In this dissertation, the dynamic loadings imposed on both interior and exterior sides of the tent structure due to the airblasts and the following dynamic responses are mainly studied with a simple theoretical method of analytical/empirical models and a numerical method of an iterative Fluid-Structure Interaction (FSI) using Computational Fluid Dynamics (CFD) and Computational Structural Dynamics (CSD), as part of an investigation into the CPS failure mentioned above.

First, using the analytical/empirical methods, the external blast loading over a closed flexible structure and the internal blast loading inside the flexible structure was obtained. For the analytical/empirical model method, a computational program for estimating airblast pressure loadings was developed to accommodate shelter-type structures. The original program, BLAST.f[10], written by Chock and Kapania, calculated airblast wave loadings on a rigid wall due to an external explosion with incident angles[10] from 0 to 90 degrees, *i.e.*, the windward side of the cylindrical structure in Figure 1.2. A modified program, BLAST2.f, extended the range of incident angles from 0 to -90 degrees, *i.e.*, the leeward side of the cylindrical structure (the wall facing away from the incoming blast wave) in Figure 1.2 and adopted a newly-defined modeling equation and parameters to generate reflected overpressure profiles for structures with a flexible skin. With these changes, BLAST2.f is now capable of calculating the airblast pressure loading over an entire flexible structure including the leeward side. In addition, using the reduction factor method proposed in the present study, which models the reduced strength of the blast wave transmitted through the wall, and the BLAST2.f program, a transmitted blast wave loading on the leeward-side inside the tent was calculated.

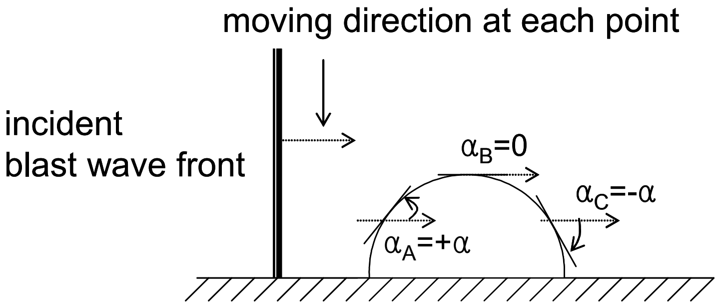

Figure 1.2 Definition of angle of incidence, α, with positive sign countclockwise

Results from BLAST2.f are provided as time-varying pressure profiles at various locations over the whole flexible structure. These results were compared with experimental data obtained from field tests conducted by the Air Force Research Laboratory. The experimental pressure data were gathered from pressure gauges attached to the flexible skin at different locations. The comparison shows that the methods developed in the present work can be a good design tool to analyze the loading conditions for rigid or flexible structures under an explosive situation.

Then, a numerical method of an iterative Fluid-Structure Interaction (FSI) using CFD and CSDynamics was employed to simulate the blast wave propagation inside and outside the flexible structure, and to calculate the dynamic loads on the flexible structure. For the numerical simulation using a commercial CFD program, Fluent, the dynamic flow field outside a rigid structure was solved numerically to simulate the propagation of the explosive wave over the structure. The external flow field outside the structure was discretized using unstructured conformal grids[11], and the Euler/Navier-Stokes equations were solved for the coupled, implicit/explicit, unsteady motion of the ambient air in the discretized flow field domain. A second-order upwind scheme was chosen for the Euler/Navier-Stokes solver and the Courant number was set to 0.1. Subsequently, the blast loading over the whole structure was obtained from this solution. CFD was particularly suited for this work due to the dynamic mesh model[11] implemented recently in the CFD software used in this work. The dynamic mesh model is updated at each time step by the motion of chosen moving boundaries which are defined as functions of time and location before the computation. In this work, the moving boundary was used to define the approximate propagation of a detonation front, formed by the boundary between the direct explosion-driven chemical reaction region and the induced flow field region surrounding the explosion. The motion of this boundary was sought by comparing the blast loading over the structure calculated from the CFD solution with the blast loading estimated by BLAST2.f.

Then, the transmitted wave pressure loading on the interior side of the tent structure due to the dynamic response of the structure to the external blast loading was estimated using iterative FSI algorithm[12-13], which is an interaction algorithm proposed by Bendiksen[14]. In this method, as a type of fully explicit partitioned[13] or staggered[15] algorithm, CFD and CSD based on the Finite Element Method (FEM) were performed iteratively at every intermediate time step to generate the transient boundary conditions during the interaction between the structure and the flow field. Boundary conditions, the pressure loading for CSD, and the movement of the boundary defining the flow field for CFD are the direct means by which the domains of the fluid and structure influence each other. After the exterior blast loading over the structure was estimated using BLAST2.f, CSD was performed for the transient analysis of the response of the structure to the external pressure loading to determine the deformation at the initial time step. This deformation was used as the boundary condition for solving the internal flow field inside the structure using CFD to calculate the interior pressure loading due to the movement of the internal flow field. Finally, the resultant pressure loading was calculated from the external pressure loading determined in advance and the internal pressure loading. This resultant pressure loading was then used as the boundary condition in CSD for the next time step. This staggered iteration was repeated until the transmitted wave pressure loading was obtained on the chosen wall.

For the CSD calculation, the tent structure was modeled with quadratic shell-type elements for the fabric and fixed geometric conditions for the frame. The shell–type elements have six degrees of freedom and are capable of modeling material and geometric nonlinearities. The full solution method with the Newton-Raphson method and the Newmark method was employed for the nonlinear transient analysis. For the CFD solution, the same numerical methods used for the external flow field were implemented for the internal flow field solution.

Finally, the numerical simulation of the blast wave propagation using the CFD and the deflection rates calculated through the FSI analysis for the transmitted blast wave loading was combined to simulate the blast wave propagation over the flexible structure and to calculate the pressure loads on the flexible structure.

All the results were compared with the field test data conducted by the Air Force Research Laboratory. The experimental pressure data were gathered from pressure gauges attached to the tent surfaces at different locations. The comparison showed that the proposed methods can be a good design tool to analyze the loading conditions for rigid or flexible structures under explosive loads. In particular, the causes of the failure of the liner on the leeward were explained. Also, the results showed that the effect of fluid-structure interaction should be considered in the pressure load calculation on the structure where the structural deflection rate can influence the solution of the flow field surrounding the structure. Finally, through these comparisons, the analytical/empirical methods and the numerical methods of the FSI analysis using CFD and CSD was validated.

1.2 Review of Literature

1.2.1 Blast Loading

Historically the analysis of explosion phenomena has been studied either through simplified analytical or empirical models, or using intensive numerical simulations involving computer technologies[16]. In this section, the literature related to the analytical and empirical methods is reviewed.

Due to an explosion's potential threat to military targets, much detailed work on explosive loading is inaccessible, but the general properties of explosive blast loadings over a structure are described in Norris *et al.*[17], Baker[18], Baker *et al.*[19], Smith and Hetherington[20], Bulson[21], and Tedosco, *et al.*[22], for example.

External explosions are divided into three types: free airblasts, airblasts, and surface (or mine) blasts. The free airblast is an explosion that occurs sufficiently above a structure that the shock wave due to the explosion hits the structure before it interacts with the ground surface. In the airblast, the interaction with the ground surface is considered for the shock wave. In the surface blast, an explosion occurs at or near the ground surface so that the shock wave is instantly reflected and strengthened by the ground surface.

When a shock wave developed by one of the three types of explosions hits a structure, it is reflected and magnified by the structure, depending on the incident angle between the moving direction of the wave and the surface of the structure. Srivastava[23] studied the interaction of shock waves. Blasts can impinge on a structure either normally or obliquely. In the case of oblique reflection, an event known as Mach reflection can occur, in which the incident and reflected shock waves are joined by a third shock wave called the Mach stem. The pressure imposed on the surface of the structure right after the shock wave is reflected is called the reflected pressure (*i.e.*, blast loads on the structure due to the explosion). This reflected pressure is compared with the incident (or side-on) pressure that is defined when the incident angle is 0°, *i.e.*, α_B in Figure 1.2. The reflected pressure is always higher than the incident pressure at the same distance from the origin of the explosion[18], with the highest difference at an incident angle of 90°. After impingement, the blast is diffracted around the structure. The pressure decays with distance from the explosion, and the form of the loading becomes more complex as the shock wave engulfs the structure[24].

The blast load imposed by an external explosion on a structure is generally described by time-varying pressure profiles at selected locations over the whole structure. The profiles usually have two phases: (i) positive phase, *i.e.*, overpressure period - a sudden rise in pressure (called a peak overpressure) above the pressure (called the reference or ambient pressure) before the explosion, then a quick decrease to the reference pressure, and (ii) negative phase, *i.e.*, underpressure period - a continuing slow decrease below the reference pressure, then an increase over the reference pressure. In most blast studies, only the overpressure profile is considered. There are, however, secondary shocks[19] after the negative phase, and this will be discussed later.

Methods for determining blast loads on structures based on experimental data are summarized by Doolittle[16]. They are also explained in TM 5-1300, an electronic version of the tri-service design manual, and in CONWEP (which stands for **Con**ventional **W**eapon **E**ffects **P**rogram), a program designed to perform weapon-effect calculations including airblast predictions. A computational program, BLAST.f, to determine external blast loads on a rigid structure such as one made of steel and concrete, was developed by Chock and Kapania[10] using empirical formulas based on the following references: Baker[18], U.S. Army's Engineering Design Handbook[25], Kingery and Bulmash[26], Army Technical Manual[27], and Bulson[21].

Baker[18] and U.S. Army's Engineering Design Handbook[25] cover the basics of explosive airblast analysis, theoretical computational methods, experimental blast analysis, and the equipment used in analysis and data gathering. While both cover similar topics, U.S. Army's Engineering Design Handbook[25] describes the calculation of reflected pressures after blast waves strike a flat surface at an arbitrary incident angle from 0 to 90 degrees. Kingery and Bulmash[26] present similar data that has been scaled for use with a different form of scaled parameters. They also provide some insight into ground reflection and the topic of critical incident angle for blast waves, while providing a specific set of results for that condition, and the application to nuclear weapons in ground burst. Bulson[21] presents a discussion of loadings that have been determined from nuclear tests as well as smaller scale conventional explosives. This reference specifically mentions a method for the determination of blasts in ground reflection which matched, with the exception of a factor, the method extrapolated from Ref. [18]. Finally, the Army Technical Manual[27] on the protective design of structures for conventional weapons effects, TM5-855-1, essentially presents methods found in Kingery and Bulmash[26] for calculation of blast loads, and provides some insight into what features should be considered in a design tool.

The present study revealed that in all the methods, the blast loading was computed with respect to a solid surface or structure. The capability of calculating the airblast pressure loading over an entire flexible structure including the leeward side (the wall facing away from the incoming blast wave), as considered in this study, will be valuable for design of a tent-type structure.

1.2.2 Numerical Simulation of Blast Wave

The advent of high-speed and large-memory computers has enabled CFD to solve various fluid flow problems including those that are compressible or incompressible, laminar or turbulent, chemically reacting or non-reacting. Therefore, it has now become possible to perform intensive numerical simulations for the analysis of explosion phenomena, even on personal computers.[16] The computational programs originally used to carry out these numerical studies were wave propagation codes capable of analyzing the highly nonlinear and time-dependent nature of explosions,[16] *i.e.*, simulating the blast (or shock) wave propagation. The blast wave characterizes the explosion, *i.e.*, the rapid and violent form of decomposition from the chemical reaction[16].

Numerical methods for compressible flows, which provide the groundwork for wave propagation codes, started in the 1940s-50s and can be classified into three universal methods[28]: (i) the method of finite-differences[29-31], (ii) the method of integral relations[28,32,33], and (iii) the method of characteristics[34-35]. The finite-difference method with artificial dissipative mechanisms[36-39] and the numerical method of characteristics[41-45] were commonly used methods in explosion wave calculations in the U.S. in the 1960s.[43] Due to the computational capability in those days, the former method, almost the same concept as used in the current finite difference method (FDM) to solve the flow field from the Euler/Navier-Stokes equations, used artificial dissipative mechanisms to improve the numerical results with coarse grid cells, and alternatively the numerical method of characteristics applied the approximated flow characteristics and solved the simplified differential equations numerically. In addition, the treatment of numerical errors and stability criterion[29], caused by replacing the partial differential equations (PDEs) by finite-difference equations, was one of the most important issues. The Courant-Friedrichs-Lewy (CFL) stability criterion and the von Neumann stability analysis were developed and have been the basis of stability of the solution to certain type of PDEs by numerical methods.[46] Tyler[47] discussed heuristic analysis of defining truncation error in using finite-difference techniques and utility conditions to be determined to give better computational results for convective flow equations involving shock wave propagation.

Belotserkovski and Chushikin[28], focusing on Soviet scientists and the method of integral relations in the 1950s-60s, presented a survey of numerical solutions of problems in gas dynamics and mentioned the numerical solutions of explosion phenomena using the method of characteristics, the method of integral relations, and the method of finite differences. Brode *et al.*[48] also reviewed the literature on blast wave pheonomena and numerical solutions in the 1960s and anticipated the features to be included in numerical programs, *i.e.*, current CFD features such as turbulent mixing, boundary layer growth, and 3-D flow characterizations as well as improved numerical techniques and hydrocode features of contact surfaces coupled with hydrodynamics.

Aside from the basic concept in numerical methods to compute the fluid flows, Hicks[49] developed the One-Dimensional Lagrangian Hydrodynamics (IDLH) solution scheme originated from the ingenious scheme of Godunov[31,50]. The hydrocode, as written in Ref. [49], could be extended to any continuum-mechanics flow problem[49,51] theoretically, and this point of view makes a difference with the numerical methods mentioned above, and Hicks *et al.*[52-53] developed several Lagrangian wavecodes and hydrocodes in their internal reports in the 1970s. Doolittle[16] summarized hydrocodes for simulating explosion phenomena and determining the transient response of structures, and mentioned the hydrodynamic codes developed at Los Alamos National Laboratory during the 1960s and 70s such as Fortran BKW[54] and 2DE[55]. Mader[56] also summarized and explained numerical modeling of explosives using BKW and SIN. The BKW (Becker-Kistiakowsky-Wilson) equation of state is well established in Ref. [56]. Zukas *et al.*[57] applied hydrocodes to visualize shock-wave phenomena, considering the case of hydrodynamic ramming on space structures. Mair[58] reviewed the various hydrocode methodologies (Lagrangian, Eulerian, Coupled Eulerian-Lagrangian, and Arbitrary Lagrangian-Eulerian) and defined the terminology of hydrocodes, separated from CFD and Computational Solid Mechanics (CSM, of which computational structural dynamics, or CSD, is a subset). Recently, Mahmadi *et al.*[59] investigated an air-blast simulation using an explicit finite element code, LS-DYNA, a hydrocode using Eulerian Multi-material and Arbitrary Lagrangian Eulerian formulations. They used the JWL (Jones-Wilkins-Lee)[59] equation of state for gaseous products of detonation. Although blast wave propagation was one of the important issues in hydrocodes, reviews are limited mostly to CFD-related blast wave propagation problems in this section.

Goldstine and von Neumann[38] introduced an artificial viscosity mechanism into the finite-difference method in Eulerian coordinates for the spherical blast wave problem, and Brode[39] solved this problem numerically using artificial viscosity. Lax[37] later solved this problem using finite-difference equations which conserve mass, momentum, and energy exactly, involving the implicit artificial viscosity concept[31,37]. Brode[39,40] established non-self-similar solutions of the decay of spherical blast waves driven by a solid, high-explosion (HE) charge. Sedov[41] , Sakurai[42], Chou *et al.*[43], and Oppenheim *et al.* [45] solved wave propagation problems in plane motion in addition to cylindrical and spherical motions with the numerical method of characteristics. Richtmyer[60], in his brief survey on computational methods for compressible fluids, explained the mathematical formulation of the initial value problem (IVP) and idealized physical modeling of the compressible flows. Korobeinikov *et al.*[61] discussed results from the numerical method of integral relations for gasdynamics problems associated with shock waves produced in various media by detonations. Point detonations in an ideal gas with counterpressure and in combustible gas mixtures, underwater explosions, detonation of a cylindrical charge of finite length, point detonation at a free surface, and the explosion of a flying meteorite were covered.

Erdos *et al.*[62] developed numerical methods for the unsteady compressible flow between the Mach disc and blast wave to solve the muzzle blast field, assuming spherical symmetry. The results obtained were in good agreement with experimental measurements of the motion of the blast wave, the contact surface, and the Mach disk for a 3200 ft/sec round fired from an M16 rifle. Glaz[63] applied Glimm's method to solve explosion problems numerically. Eidelman and Burcat[64] numerically solved the problem of a detonation in a two-phase reactive medium, *i.e.*, six nonlinear hyperbolic equations with initial conditions, using the flux corrected transport (FCT) algorithm.

Following those numerical studies of wave propagation codes capable of analyzing the highly nonlinear and time-dependent nature of explosions,[16] *i.e.*, simulating the blast (or shock) wave propagation, Colella *et al.*[65] and Glaz *et al.*[66,67] began to consider the necessity of accurate numerical simulation of the reflection of a blast wave from a plane surface, and discussed its characteristics (two-dimensional and non-self-similar) and the influential parameters (the scaled height of burst of the explosion, the blast source, and the equation of state of the medium) in the 1980s. Literature reviews for experimental/analytical results for blast wave reflection were covered in the previous section.

Colella *et al.*[65] solved 2-D axisymmetric reflection of a spherical (high-explosive-driven) blast wave, using the Euler equations that were solved with a nondiffusive numerical algorithm. The computational techniques of the second-order Godunov scheme, the equations of state, the initial conditions, and the grid dynamics were discussed. Harten *et al.*[68] introduced the ENO (essentially nonoscillatory) scheme and Jiang and Shu[69] established the high-order weighted essentially nonoscillatory (WENO) scheme for spatial discretization associated with a fourth-order Runge-Kutta method for time integration. Ofengeim and Drikakis[70] solved the Euler/Navier-Stokes equations using an adaptive grid method and a second-order Godunov scheme to simulate planar blast-wave propagation over a cylinder. Their results revealed that the blast-wave duration significantly influences the unsteady flow over the cylinder. Jiang *et al.*[71] numerically investigated micro-blast-wave propagation. They used a dispersion-controlled scheme for numerical simulation, and a similarity solution was used as an initial condition. Liang *et al.*[72,73] numerically investigated the problem of an unsteady cylindrical blast-wave interaction with a flat plate. They solved the two-dimensional Euler/Navier-Stokes equations in a finite volume fashion using a fifth-order WENO scheme for spatial discretization associated with a fourth-order Runge-Kutta method for time integration.

Flaherty *et al.*[74] reviewed several properties of the Discontinuous Galerkin (DG) method for solving hyperbolic systems of conservation laws including basis construction, flux evaluation, solution limiting, adaptivity, and *a posteriori* error estimation, and developed the DG code for unsteady, two-dimensional, compressible, inviscid flow problems. These include adaptive computations of Mach reflection and mixing-instability problems. Cler *et al.*[75] applied CFD and DG codes to gun muzzle blasts and compared the results from numerical methods with experiments.

1.2.3 Response of Flexible Structures to Blast Loadings

When the rigid or flexible structures are placed under the dynamic loading condition such as airblasts, the response depends on the duration of the loading, the peak load, and the shape of the pressure pulse. The blast parameters and the blast loading were already reviewed and explained in Section 1.2.1. In this section, some of the literature related to the dynamic response of the rigid or flexible structure to dynamic loading is reviewed.

There have been many studies involving explosive loads on plates. Nurick and Shave[76] and Nurick *et al.*[77] respectively studied the failure of square and circular plates at their edges. The failure mechanism may involve tension, shear, or a combination of tension and shear. Clamped circular plates were considered by Wierzbicki and Nurick[78], and also by Bland and Kapania[79]. The effects of the distribution and magnitude of the loading were examined. For small impulses, bending and shear resistance are important, whereas membrane stretching resistance dominates for large loads. Two main failure modes are described: one involves tensile necking at the outer edge of the loading area, and the other involves fracture at the clamped boundary. Liu and Stronge[80] treated a similar problem and determined the final deflection of a rigid-plastic plate. Turkmen[81], and Chock and Kapania[82] used a commercial finite element software, ANSYS, to study the structural response of isotropic plates subjected to blast loads. Türkmen and Mecitoglu[83] used the same approach to obtain the nonlinear response of laminated composite plates to blast loading. They replaced the prediction of blast loads with an experimental result by using a shock tube to generate a dynamic pressure shock which was measured by a wooden board with pressure transducers. These experimental results were used as a loading condition to a finite element model of a stiffened composite plate. This is notable because unlike the other works, Türkmen and Mecitoglu used an overpressure profile with a large negative phase. Using this, they were able to get good correlation with experimental results with the same type of dynamic loading. Their work showed the discrepancy between the experimental and numerical results in comparing the strain-time history for the nonlinear range, mainly due to the presence of membrane strains. Jacinto *et al.*[84] also described experimental and computational results for plates under airblasts. Similarly, Ramajeyathilagam *et al.*[85] studied the nonlinear transient response of rectangular plates subjected to underwater explosions. Wu and Chang[86] and Zhu[87] examined the transient deformation modes of square plates subjected to explosive loading. Louca and Harding[88] analyzed the nonlinear behavior of imperfect plates under transient lateral pressure loading. The response of stiffened and unstiffened plates subjected to blast loading was treated by Louca and Harding[89]. It is important to determine failure modes. Rudrapatna *et al.*[90] presented numerical results for a thin square plate, including geometric nonlinear effects, and proposed failure criteria for bending, shear, and tension.

With regard to shells, Yakupov[91] treated an infinitely-long rigid-plastic cylindrical shell subjected to an external spherical blast. Diffraction of a blast around a structure is described in Salvatorelli-D'Angelo[92]. Wierzbicki and Hoo Fatt[93] and Hoo Fatt[94] analyzed a ring-stiffened cylindrical shell, also infinitely long with rigid-plastic behavior, subjected to a decaying pressure pulse over the top of the shell. Each bay was modeled as a string on an elastic foundation. Transient blast response of a panel of an elastic toroidal shell was examined by Redekop[95], using a series approximation and time integration to compute the motion. Mohan and Kapania[96] studied the effect of large deformation-dependent pressure loading on shells and found that the pressure stiffness matrix affects the convergence of the solution in problems where large deformations are encountered. Gangadhara Prusty and Satsangi[97] examined the dynamic response of laminated stiffened shells. Koh *et al.*[98] studied the dynamic response of shell structures with a focus on blast-resistant doors. The finite element results showed that the outer skin (in direct contact with the blast) undergoes larger deformation than the inner skin.

The structural materials of interest in the present research are true membranes[99]. They have no resistance to bending when in their natural state, and do not have a given form in that state. There is extensive literature on textile composites, including Naik[100], Portanova[101], Suherman[102], and Cox and Flanagan[103]. There are some investigations of the dynamic response of membranes that are relevant. Farrar[104] examined a circular membrane subjected to a non-penetrating axisymmetric impact by a projectile. Elastic behavior was assumed in the analysis, and experiments were also carried out. In Ghosh *et al.*[105], an impulsive load was applied to clamped membranes, with application to explosive forming of metal sheets. A rigid-plastic constitutive law was adopted, and deflections in tests were up to 40 times the membrane thickness. Mutallimov[106] and Nuriev[107] considered the impact of a cone on an elastic membrane of infinite extent, and analyzed the ensuing radial wave. A circular membrane made of a Mooney-Rivlin material was studied in Haddow *et al.*[108], in which the responses to a suddenly-applied pressure and to normal impact by a projectile were determined. Tait and Zhong[109] investigated the influence of the initial tension on the response of a circular hyperelastic membrane to a flat circular projectile. Finally, a general discussion of the dynamic behavior of curved membranes was presented in Tabarrok and Qin[110].

Bonet *et al.*[111] considered finite element analysis of air-supported membranes. These structures derive integrity from the internal pressure which produces pre-stressed tensile structures capable of supporting external pressure. Their work took into account the change in the air pressure due to the application of the external pressure. Stanuszek[112] studied the large deformation of membranes with wrinkling using the FEM.

1.2.4 Fluid-Structure Interaction

With the development of CFD and CSM/CSD tools, the use of numerical simulations in understanding the complex interactions between coupled fluid-structure systems has had important engineering interest in many fields. The evolution of high-performance computers and parallel processing contributed in developing new techniques to solve complex problems in fluid-structure interaction as well as fluids and structures separately. In the present work, the literature will be reviewed roughly from a viewpoint of numerical algorithms for coupling mechanisms, and a literature review for two different applications of blast waves and aeroelasticity will follow.

To simulate fluid-structure interaction in the time domain, both the fluid and the structure have to be integrated in time simultaneously. This coupling mechanism can be invoked at different levels within the numerical methods, resulting in either more weakly or more strongly coupled procedures.[13] One extreme is a fully explicit partitioned coupling involving an alternating solution of solid and fluid problems with a simple interchange of boundary conditions. A staggered method, introduced by Park *et al.*[15], is an example of a fully explicit partitioned coupling. This approach is very flexible concerning the choice of the solvers of each solid and fluid field, but it often suffers from poor convergence due to the time lag between alternating solutions of solid and fluid. The other extreme is a fully implicit monolithic approach involving the simultaneous solution for all unknowns.[13] A monolithic algorithm[13,113] avoids the time lag related to staggered schemes since one single operator is applied to the fluid, structure, and mesh variables simultaneously. This approach is optimal for convergence, but a complex system is hard to model and solve.

The staggered method was used for transonic flutter calculations by Prananta *et al.*[114] Piperno[115] used staggering of fluid and structure solvers and the characteristic time scales in fluid and structure solvers by choosing different time steps for both solvers. Blom and Leyland[116,117] adopted this method for the aeroelastic problem of airfoils. Piperno *et al.*[118] examined different parallel versions of the staggered algorithm. A predictor-corrector iteration technique was presented by Prananta and Hounjet[119]. Giles[120] investigated staggered algorithms for aeroelastic problems and discussed the accuracy and numerical stability using several fluid and structure solvers.

Another interaction algorithm was proposed by Bendiksen[14] where the fluid and structure were coupled in the time domain by an explicit fourth-order Runge-Kutta scheme. In this method, the interaction is updated at every intermediate time step. He[121] applied this method to a cascade flutter problem. Due to the decrease of exchanging interval between fluid and structure, the accuracy of this algorithm was superior to the standard staggered algorithm.

Alternatively, implicit fully coupled algorithms have gained more interest. This interest is driven by the need for larger time steps to reduce the computation time. Alonso and Jameson[122] and Melville *et al.*[123] used an implicit algorithm to integrate the fluid and structure in time. The nonlinear system of equations was solved by an iterative Newton-Raphson solver. But this algorithm also remained essentially staggered. Blom[113] proposed a monolithic algorithm in order to avoid the time lag related to staggered algorithms and compared its results with those from several staggered algorithms.

Recently, a combination of a monolithic algorithm with a staggered one as a smoother or a preconditioner[124] was introduced, and Schafer *et al.*[13,124] applied this combination technique for several FSI problems. Also, an ALE multi-material formulation, originated from hydrocodes, was proposed by Souli *et al.*[125] for FSI problems.

1.3 Dissertation Outline

As shown in **Figure 1.3**, Chapter 2 will cover the empirical/analytical method for predicting the blast loading for side-on, reflected, and diffracted overpressure over a rigid and/or flexible structure. Also, using the Reduction Factor Method introduced in this chapter, the transmitted blast wave loading inside the tent will be estimated considering the effect of a flexural membrane on blast wave transmission into a structure. The program, BLAST2.f is developed by modifying BLAST.f, developed by Chock and Kapania. Capabilities of BLAST2.f will be described and applied to estimate the overpressure profiles over a flexible tent in the condition as pertained to a field test. The estimation from the BLAST2.f program will be compared with the field test data and thus will be validated.

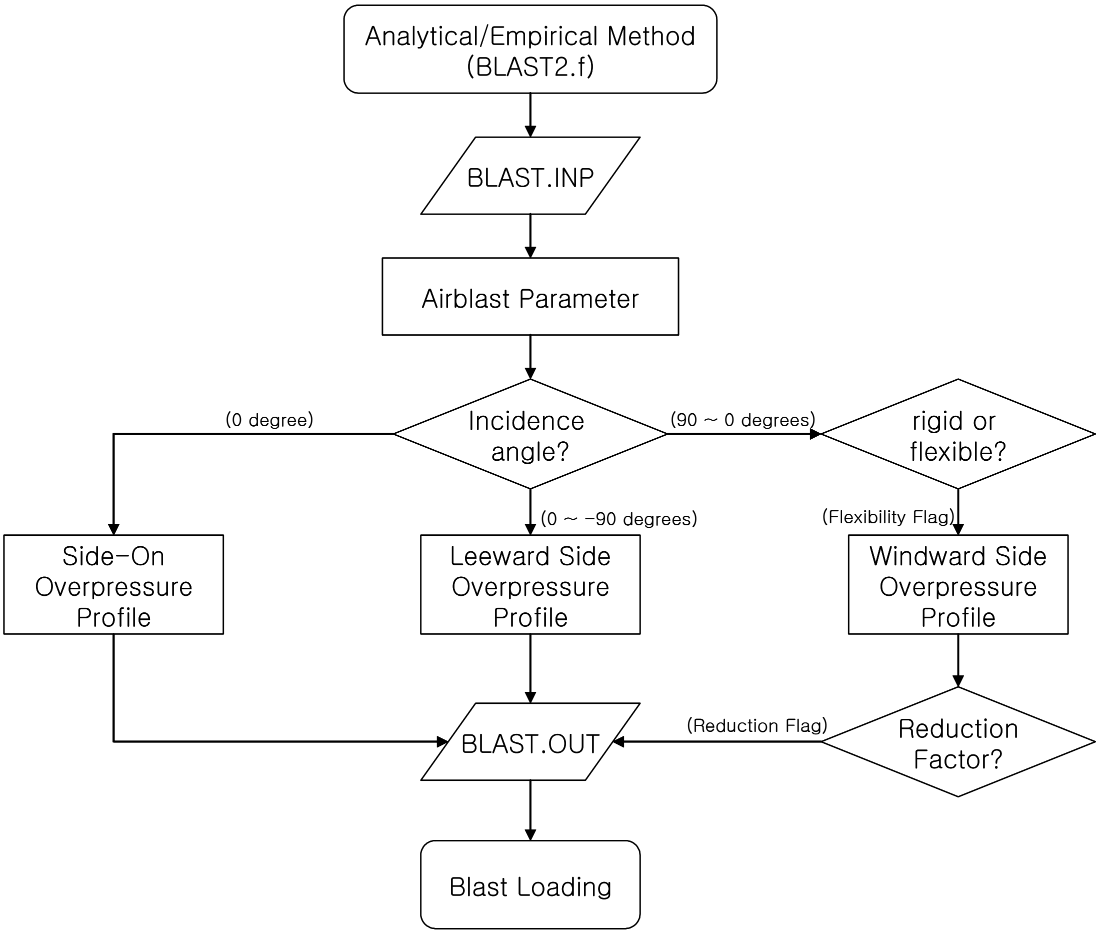

Figure 1.3 Flowchart of BLAST2.f program which predict the blast loading on rigid or flexible structures in analytical/empirical methods

Chapter 3 will cover the numerical simulation of blast wave propagation in air using a commercial CFD code, Fluent, and the blast loading of overpressure profiles on a rigid structure. For the blast wave propagation, recent examples using various numerical methods and boundary conditions will be reviewed and they will be compared with the numerical simulation done in the present work. Finally the overpressure profiles obtained from the numerical simulation will be compared with empirical/analytical results.

Chapter 4 will describe the FEM methods for flexible membrane structures and its dynamic response to blast loadings. For this purpose, the finite element models in ANSYS will be reviewed and a numerical test will be performed for the finite element model which can be used in the transient analysis. Then, an application of transient analysis to the tent structure under blast loading will be performed.

Chapter 5 will explain the iterative FSI algorithm and the algorithm will be applied to the FSI analysis for the transmitted blast wave and the blast loading inside the flexible tent as shown in Figure **1.4**. Then the results from the FSI analysis will be compared with both experimental and estimated data. Finally, the numerical simulation of blast wave propagation covered in Chapter 3 will be extended to the flexible structure by involving the results of the FSI analysis as shown in Figure **1.5**, and the blast loading of overpressure profiles on a flexible structure obtained from the numerical simulation will be compared with both empirical/analytical results and experimental data.

Chapter 6 will present the concluding remarks and recommendations for future work.

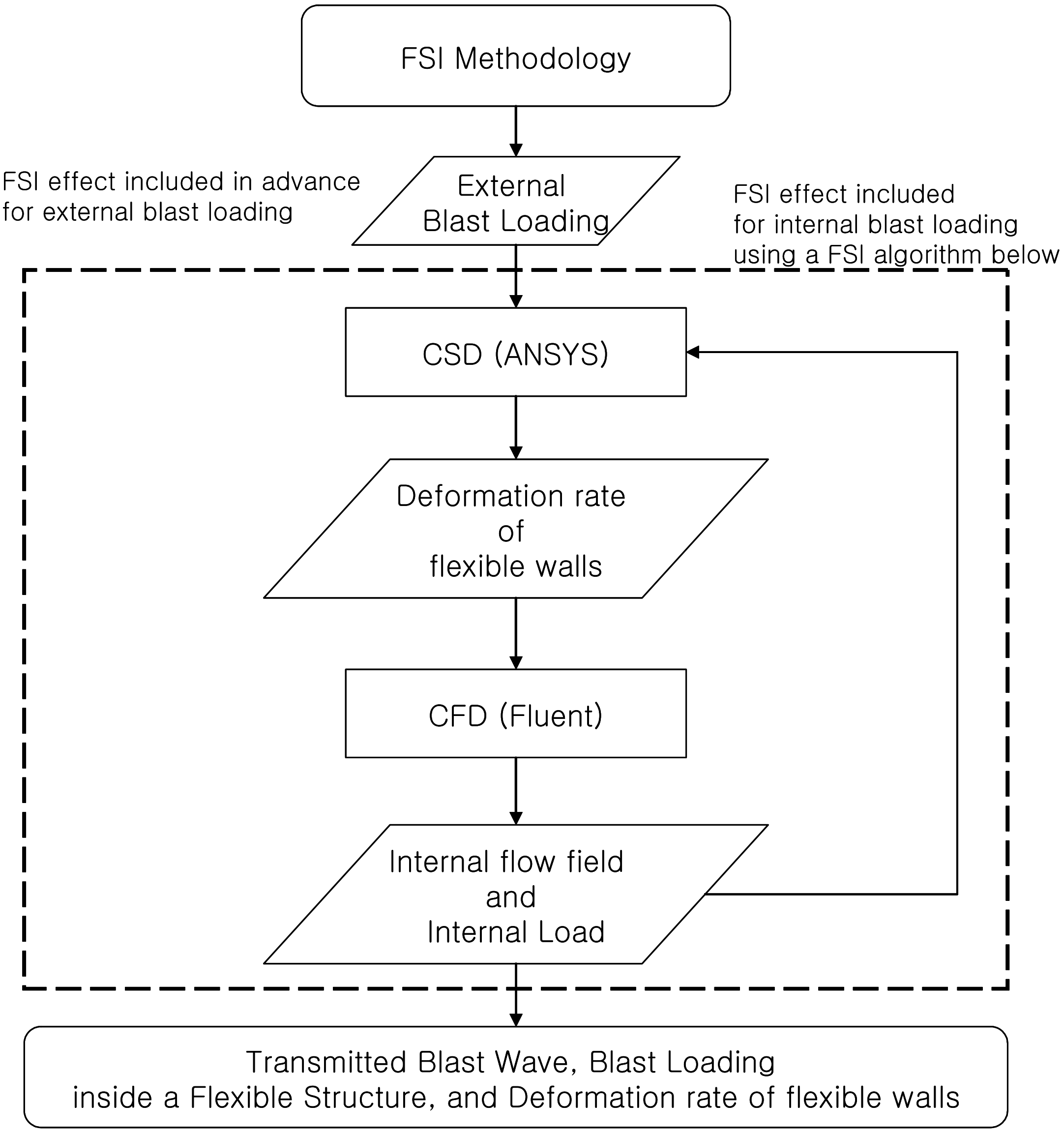

Figure 1.4 Flowchart of an iterative FSI algorithm which simulate the transmitted blast wave and predict the blast loading inside a flexible structure

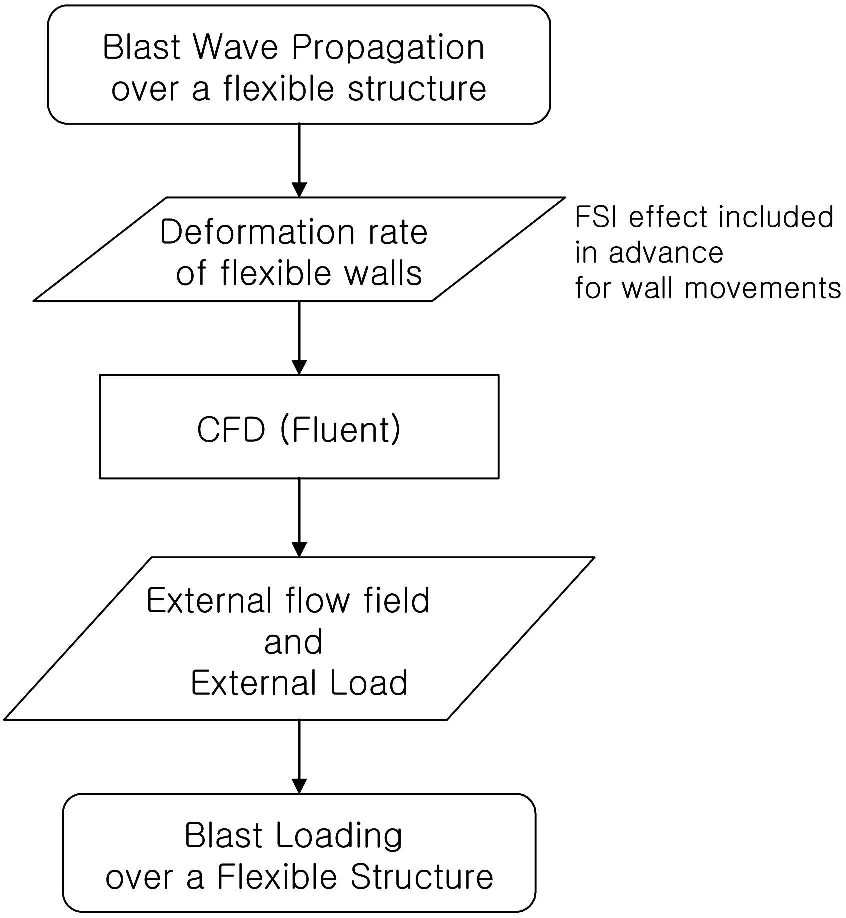

Figure 1.5 Flowchart of the numerical simulation of a blast wave propagation over a flexible structure

1.4 Contribution to the Field

The present work provides a way for both an engineer working in the design of flexible structures under blast loading and also an analyst examining the explosive blast itself to understand physical phenomena when a flexible structure is placed in a high-explosion situation. Thus, this work with the collaborative works done in material test and transient response analysis of the tent to the blast loading as a group research[9] reduces the required effort in the design of flexible structures which have some resistance or inherent protection to specific blast threats, and also allows the design of structures which would have qualities that would protect the structure's occupants.

From the field test and the analysis of a transmitted blast wave loading through a highly deformable structure which is performed in two ways of (i) an empirical reduction factor and (ii) the FSI analysis using a staggered algorithm, it was shown that the internal fluid behavior is an importnat factor in the design of the flexible structure under blast loading. Therefore, the method developed in the present research work can be used to predict the characteristics of the transmitted blast loading for the similar cases. In addition, the method of using the FSI analysis and a CFD codes to estimate blast loading over a rigid and/or flexible structure can be extended to estimate underwater blast loadings.

Then, the FSI analysis using CFD/CSD can be expanded into more general problems such as non-linear aeroelasticity problems, specially for morphing wings, low Reynolds number unmanned air vehicles (UAVs) or structural analysis in which unsteady response is a dominant effect. The advantage of the FSI analysis to aeroelasticity analysis is the capability of nonlinear aeroelastic analysis, *i.e.*, to predict the unsteady motion of a structure in the time domain as well as application of critical stability criteria such as flutter or divergence speeds, which is a main objective in classical aeroelasticity analysis.

This application of the FSI analysis is also a good example for taking advantage of parallel processing since the flow field domain can be divided by the flexible structure and so the application of parallel processing for the divided flow fields can save the computational time needed for the iterative FSI analysis.

Chapter 2

Prediction of Blast Loading

As shown in **Figure 1.3**, this chapter will cover the empirical/analytical method for predicting the blast loading for side-on, reflected, and diffracted overpressure over a rigid and/or flexible structure. Also, using the Reduction Factor method introduced in this chapter, the transmitted blast wave loading inside the tent will be estimated considering the effect of a flexural membrane on blast wave transmission into a structure. The program, BLAST2.f is developed by modifying BLAST.f, developed by Chock and Kapania. Capabilities of BLAST2.f will be described and applied to estimate the overpressure profiles over a flexible tent in the condition as pertained to a field test. The estimation from the BLAST2.f program will be compared with the field test data and thus will be validated.

2.1 Introduction

An explosion, *i.e.*, the rapid propagation of blast waves, is created by the sudden and violent release of energy in the gaseous products of detonation and this blast wave propagation causes the ensuing sharp rise in the pressure of the surrounding aero or hydro medium. When this blast wave propagations collide and then reflect or pass over a structure, the structure sustains the similar pressure loads varying over a very short time which can be represented by blast loadings[18,19], *i.e.*, time histories of pressure change at points caused by the propagation of an explosive blast waves over the points. This blast loading can be shown quantitatively by a pressure profile as shown in Figure 2.1.

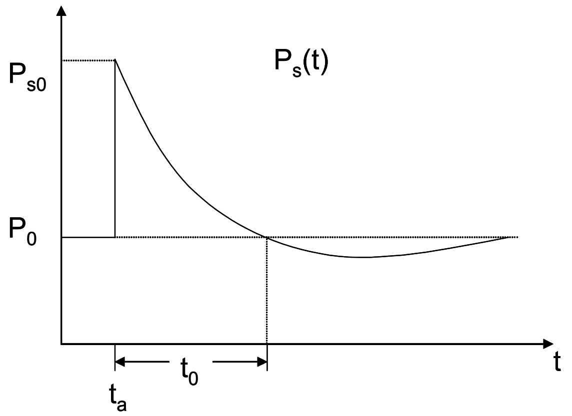

Figure 2.1 A general pressure profile, caused by the propagation of an explosive blast wave, where P_{s0} is a peak overpressure, t_0 is duration of the positive overpressure on the wall, t_a is the time when a blast wave arrives at a measuring point, and P_0 is ambient (or reference) pressure.

The pressure profile is usually defined by a few parameters such as a peak overpressure P_{s0}, a duration time of the positive overpressure t_0, and an arrival time of the blast wave front t_a, shown in Figure 2.1. These parameters are obtained experimentally or analytically and are functions of an explosive power—the magnitude of TNT or an equivalent amount of TNT, a distance from the origin of a detonation to a measuring point, and an angle of incidence which is defined as an angle between the moving direction of a blast wave and a surface on which the pressure is measured at a point (see Figure 1.2). These parameters will be explained in Section 2.2 in detail.

As shown in Figure 2.1, these pressure profiles usually have two phases: (i) positive phase, and (ii) negative phase. In most blast studies, the positive phase has been considered to be the more important of the two phases and has been the general concern in explosion-related engineering problems. This positive phase is usually known as an overpressure profile, and numerous model equations have been proposed for it. For example, Flynn proposed a linear decay of the overpressure, and Ethridge proposed a better form of an exponential decay of the overpressure.[10] In the present work, Friedlander's overpressure profile, Equation (2.1), which fits experimental results with a curve, is used as the basic profile equation:

$$P = P_{s0}\left(1 - \frac{t - t_a}{t_0}\right)e^{-\frac{t - t_a}{t_0}} \tag{2.1}$$

where P_{s0}, t_0, and t_a are explained in Figure 2.1. This Friedlander's equation is modified according to the property of a peak overpressure measured at a point on a surface and also the deforming rate of the surface (this is a effect of a fluid-structure interaction), and the modifications will be explained in detail in Section 2.3. The peak overpressure is generally divided into three groups according to the behavior against the structure: (i) side-on or incident overpressure, (ii) windward-side or reflected overpressure, and (iii) leeward-side or diffracted overpressure.

When a blast wave travels parallel to the surface, the initial highest overpressure is called a side-on or incident peak overpressure. Since a side-on overpressure is caused by an undisturbed blast wave, to measure this side-on overpressure the pressure probe hole should be placed on the surface parallel to the moving direction of the blast wave at the same point as shown in Figure 2.2 (a). When a blast wave is disturbed by a structure, the property of a peak overpressure at a point on the structure should be adjusted from a side-on peak overpressure which is measured at the same distance as the distance from the origin of an explosion to the measuring point on the surface in accordance with the incident angle at the point.[25]

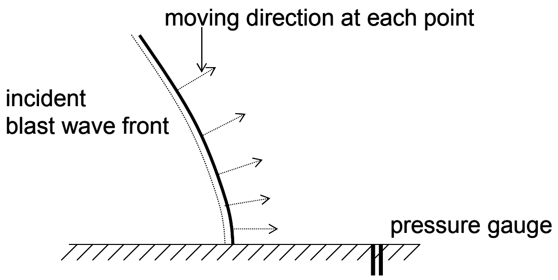

(a) side-on or incident overpressure

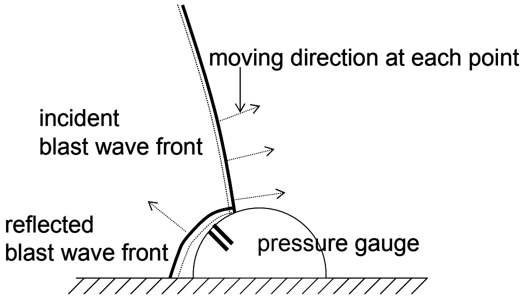

(b) windward-side or reflected overpressure

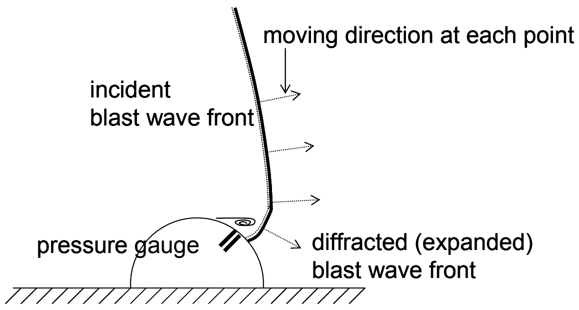

(c) leeward-side or diffracted overpressure

Figure 2.2 Comparison of overpressures measured at various incident angles

As shown in Figure 2.2 (b), when a blast wave front is reflected by the surface, the peak overpressure is much higher. Therefore, this windward-side overpressure has been called “reflected overpressure”, and much research has investigated this reflected overpressure. When a blast wave front is passing over the leeward side as shown in Figure 2.2 (c), the blast wave is diffracted or expanded, and the leeward-side peak overpressure is reduced from the side-on peak overpressure.

In most blast loading problems, only side-on and reflected overpressure have been considered. The term “leeward-side or diffracted overpressure” is chosen as new terminology to be used in the present work, in which the leeward-side blast loading is very important.

2.2 Airblast Parameters

The overpressure profile is usually defined by a few parameters such as a peak overpressure P_{s0}, t_0, and t_a, shown in Figure 2.1 or Figure 2.6 and these parameters are obtained experimentally or analytically. They are functions of the explosive powers, the distances from the origin of the detonation to a measuring point, and the angles of incidence. In the present work, airblast parameters were obtained through Kingery and Bulmash’s[26] experimental data sets. There are, however, different data sets of airblast parameters as explained in detail in Ref. [10]. In this section, explosive powers, scaling laws with varying explosive powers and distance, airblast parameters, overpressures, and incident angles will be explained in turn.

2.2.1 Explosives: TNT or Equivalent TNT

In the usual process classified as an explosion, energy is released in a fairly quick time and in a small volume, and some properties of a blast loading (see Section 2.1) are strongly affected by both sources and manner of explosives. The general properties of an explosion source are described by its total energy, E, its energy density, E/V (V is a volume), and the rate of energy release, *i.e.*, power[18], as listed in Table 2-1. But, the type of explosion in the present research can be specified as an ideal explosion of point source or condensed phase explosives[18] as shown in Figure 2.3, since those explosions of point source or condensed phase explosions produce ideal blast waves. Then, it has been found that the blast wave produced by these "ideal' explosions can be correlated entirely by a single parameter, the total source energy, irrespective of the energy density or the power of the source.[18] Therefore, the energy per unit mass or weight is a useful indicator of the explosives, usually reported along with the density of the explosive.[18]

Table 2-1 Properties of various condensed phase explosives and conversion factor of equivalent TNT magnitude[18, 25].

Explosive	Mass Specific Energy (kJ/kg)	TNT Equivalent	Density (Mg/m^3)	Detonation Velocity (km/s)	Detonation Pressure (GPa)
Pentolite (50/50)	5110	1.129	1.66	7.47	28.0
TNT	4520	1.000	1.60	6.73	21.0
RDX	5360	1.185	1.65	8.70	34.0
Comp. B	5190	1.148	1.69	7.99	29.5
HMX	5680	1.256	1.90	9.11	38.7

However, the range of energy densities for most condensed explosives is surprisingly small, as can be seen by comparing their energy density to that of TNT as shown in the second column of Table 2-1, and most condensed explosives also have the property of exploding essentially at a constant rate for a given initial density and explosive type, called the detonation velocity D.[18] Typically, detonation velocities range from about 1.5 km/s for some blasting explosives to 8 km/s for military explosives.[18] Accordingly, though there are a number of high explosives used for military and commercial purposes, TNT is usually used as a reference explosive, and in the present work an explosive power is also described in terms of TNT weight. In case of non-TNT explosives, an equivalent TNT magnitude shown in Table 2-1, made by altering the energy released or the weight of the actual explosive component is used. The information shown in Table 2-1 was taken from from Refs. [18] and [25].

2.2.2 Scaling Laws

In blast wave analysis, scaling of the properties of blast waves from explosive sources is a common practice, and there are many different scaling methods to predict the properties of the blast wave of an arbitrary explosive as scaled from the tests conducted on a larger or smaller explosive. By these scaling laws, the experimental test results are generalized and can be utilized in the general blast wave analysis and blast loading of varying explosive powers and distances. But, because of the assumptions of a perfect gas and negligible gravity and viscosity, these scaling laws may no longer apply for some strong shock waves or for distances that are particularly close to the explosive source. In this section, Hopkinson and Sachs[19] blast scaling methods are described as the most commonly used methods.

The most common form of blast scaling is Hopkinson-Cranz or “cube root” scaling[19] as given in Equation (2.2). This law was first formulated by Hopkinson in 1915 and then independently by Cranz in 1926, based on the similarity characteristics in blast waves which are produced at identical scaled distance when two different explosive charges of similar geometry and of the same compositions are detonated in similar atmospheric conditions. From this idea, a dimensional parameter, Z, has been used as a scaled distance as shown in Equation (2.2):

$$Z = \frac{R}{E^{\frac{1}{3}}} \tag{2.2}$$

where *R* is the distance from the origin of a detonation to a measuring point, and *E* is the total energy of the explosive charge[18].

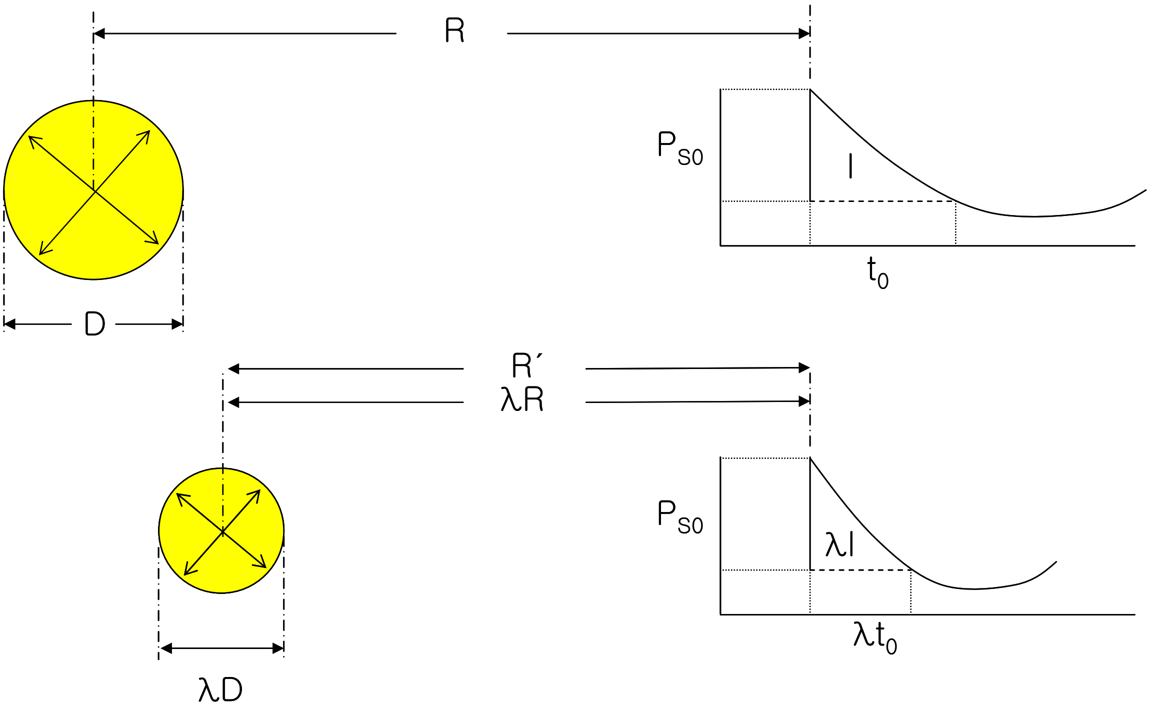

Figure 2.3 Hopkinson-Cranz blast wave scaling

Figure 2.3 shows schematically the implications of Hopkinson-Cranz blast wave scaling. An observer located at a distance R from the center of an explosive source of characteristic dimension D will be subjected to a blast wave with amplitude P_{s0}, duration t_0, and a characteristic time history. The integral of the pressure-time history is the impulse, designated as I. As shown in the lower case in Figure 2.3, most of the parameters are multiplied with the length scale factor, λ. The length scale factor ratio, λ, is defined as the ratio of R′ to R (*i.e.* λ= R′/R). The Hopkinson-Cranz scaling law states that an observer stationed at a distance λR from the center of a similar explosive source of characteristic dimension λD detonated in the same atmosphere will feel a blast wave of 'similar' form with amplitude P_{s0}, duration λt_0 and impulse λI. In Hopkinson-Cranz scaling, pressure, temperature, densities and velocities are unchanged at corresponding times.[19]

In Ref. [18], Kennedy in his 1946 work found that this scaling can be applied for varying distances if the geometry of the explosives being scaled is roughly similar. However, he noted that while the method is capable of being applied for varying distances, in some respects the trends of reported scaled values have the same form but can vary as much as a factor of two. Kingery found in his 1952 work that close agreement could be found between small-charge blasts (one to eight pounds) and larger 100-pound counterparts. Thus, Kingery and Bulmash's airblast parameters in the following section are based on the Hopkinson-Cranz scaling law.

Sachs' scaling law, proposed in 1944, is almost universally used to predict characteristics of blast waves from explosions at high altitude.[19] Sachs' law states that the blast parameters such as dimensionless overpressure, Equation (2.3), and dimensionless impulse, Equation (2.4), can be expressed as unique functions of a dimensionless scaled distance, Equation (2.5):[19]

$$\overline{P} = \frac{P}{p_0} \tag{2.3}$$

$$\bar{i} = \frac{ia_0}{E^{1/3} P_o^{2/3}} \tag{2.4}$$

$$\overline{R} = \frac{RP_0^{1/3}}{E^{1/3}} \tag{2.5}$$

where a_0 is the speed of sound in the ambient atmosphere.

According to Ref. [18], Dewey and Sperazza studied the detonation of bare pentolite spheres in an altitude simulation chamber so as to vary temperature and pressure. The Hopkinson-Cranz scaling law was shown by Deway and Sperazza to be consistent for distance changes, but not for altitude changes, *i.e.*, ambient pressure changes, while Sachs' scaling law produced excellent scaled results that were consistent for changes in both distance and altitude.

Thus, it could be shown that the Hopkinson-Cranz scaling law is a special case of Sachs' scaling law; *i.e.*, Sachs' scaling law reduces to the Hopkinson-Cranz scaling law when there is no atmospheric pressure change between the explosive test data and the actual condition of the desired explosive for which one is predicting the airblast parameters.[18]

2.2.3 Kingery and Bulmash

A computational program, BLAST.f, developed by Chock and Kapania[10] to determine external airblast loads on a rigid structure such as one made of steel and concrete, has three subroutines and each of them is based on its own data set and Friedlander's equation for overpressure profiles (refer to Section 2.3 in detail.). All the estimated airblast parameters used in the present work were generated by this program and most of the generated airblast parameters are mainly based on Kingery and

Bulmash's data set. There are, however, different data sets of airblast parameters as explained in detail in Ref. [10].

Kingery and Bulmash[26] gathered their data by detonating various charges from one kilogram to 400,000 kilograms. Measurement of shock arrival was recorded by various methods including photographic analysis, electric switches which close at the arrival of the blast wave front so that there can be an electric time stamp, and overpressure transducers. Measured peak overpressure values were taken by direct transducer measurement of the shock wave and were also inferred from the velocity of the shock front. The impulses were measured as an area under the curve formed by the pressure profile and were shown as a function of the overpressure, duration, and decay rate of the blast.

These data were then scaled to standard atmospheric sea-level conditions, mostly based on the idea of Hopkinson-Cranz and Sachs' scaling laws. Measured distances were scaled using the reciprocal of a distance scaling factor:

$$S_d = \left(\frac{Q_2}{Q_1}\right)^{1/3} \left(\frac{P_{st}}{P_0}\right)^{1/3} \tag{2.6}$$

where S_d is the scaling factor, Q_2 is the other explosive mass (in kilograms) being scaled to the reference weight of one kilogram Q_1, P_{st} is the standard atmospheric sea-level pressure, and P_0 is the ambient atmospheric pressure. Measured times were also scaled using the reciprocal of a time scaling factor:

$$S_t = \left(\frac{Q_2}{Q_1}\right)^{1/3} \left(\frac{P_0}{P_{st}}\right)^{1/3} \left(\frac{T_{st}}{T_0}\right)^{1/2} \tag{2.7}$$

where T_{st} is the standard atmospheric temperature (288 K), and T_0 is the ambient temperature in degrees K. Peak overpressures were scaled to standard atmospheric pressures by using the reciprocal of a pressure scaling factor:

$$S_P = \frac{P_0}{P_{st}} \tag{2.8}$$

Impulses were scaled to one kilogram of charge mass by using scaling factors from Equation (2.6) or (2.7) (see Figure 2.3):

$$S_i = \left(\frac{Q_2}{Q_1}\right)^{1/3}\left(\frac{P_{st}}{P_0}\right)^{1/3}\left(\frac{T_{st}}{T_0}\right)^{1/2} \tag{2.9}$$

Positive durations from various sources were scaled by Kingery and Bulmash to one kilogram of charge mass by using the reciprocals of the distance scaling factor, in Equation (2.6), and the time scaling factor in Equation (2.7) (refer to Figure 2.3).

For reflected overpressure, Kingery and Bulmash gathered data from other sources, noting that the reflected pressure data are not usually measured directly and that their data were only from cases where blasts impinged upon a surface from the normal direction. They noted that the following relationship was used for calculating the reflected peak overpressure:

$$P_{r0} = \left(P_{s0} + P_0\right)\frac{\left(2 + \frac{\gamma+1}{\gamma-1}\right)\left(\frac{P_{s0}+P_0}{P_0}\right) - 1}{\frac{\gamma+1}{\gamma-1} + \frac{P_{s0}+P_0}{P_0}} - P_0 \tag{2.10}$$

where P_{s0} is the side-on peak overpressure, P_0 is the ambient pressure, and γ is the variable ratio of specific heats. Kingery and Bulmash stated that γ is a function of peak overpressure and that this relationship can be found in graphical format in Kingery and Pannill's report at the Ballistic Research Laboratories in 1964. Peak overpressures with different incident angles will be covered in detail in the following section.

Kingery and Bulmash's data set was then converted to a computer code by using a representation in the Log-Log scale as shown below[10]:

$$Y = C_0 + C_1 U^1 + C_2 U^2 + \cdots + C_N U^N \tag{2.11}$$

where

$$U = K_0 + K_1 T \tag{2.12}$$

Y is the natural logarithm of the parameter under evaluation, T is the natural logarithm of the scaled distance, and N is the order of the polynomial fit through the data. Parameters C_j and K_j were calculated and documented completely in the tabulated data set[10].

Using this data set, the natural logarithm of a desired parameter can be determined, and using the scaling law, those dimensionless parameters can be converted into dimensional airblast parameters for use. For English units, pressures would be converted by taking an inverse common logarithm of the parameter to get pounds per square inch, and for times and impulses, the inverse common logarithm must be multiplied by the cube root of the charge weight to get units of psi-ms and ms, respectively[10].

2.2.4 Peak Overpressure and Angle of Incidence

An approximation for the area of normal reflection can be made by assuming that the limit of normal reflection will be within an area of a structure that lies within an unobstructed 45° angle of attack cone to the explosion. While this can be considered a simple rule of thumb that is easy to implement for use in commercial Finite Element Method (FEM) codes, the Army's Engineering Design Handbook[25] describes a different method for calculating reflected peak overpressures after a blast wave strikes a flat surface at an arbitrary incident angle from 0 to 90 degrees. For the calculation of this reflected peak overpressure, the side-on peak overpressure value is interpolated in Figure 2.4, then a coefficient is determined for a target incident angle. This coefficient is then multiplied by that side-on peak overpressure for the reflected peak overpressure value on the surface. This figure is given, in a tabular format, to the program BLAST2.f which has the option of adjusting the side-on peak overpressures for a given incident angle.

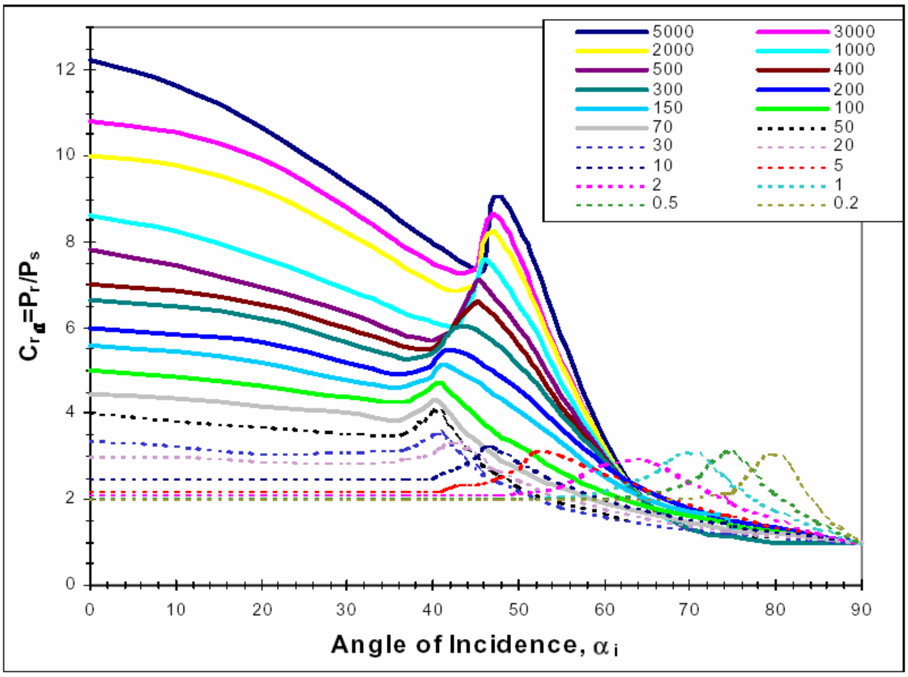

Figure 2.4 Reflected pressure coefficient vs. angle of incidence of blast waves that reflect from inclined flat surfaces. The number in the legend corresponding to each curve indicates side-on peak overpressures P_{s0} in psi, by courtesy of the author of Ref. [10]

For leeward sides, peak overpressures are also calculated from side-on peak overpressures measured at the same location. But, instead of using similar tabulated experimental data for windward-side or reflected peak overpressures, a simple correction[17], Equation (2.13), is used in the present work:

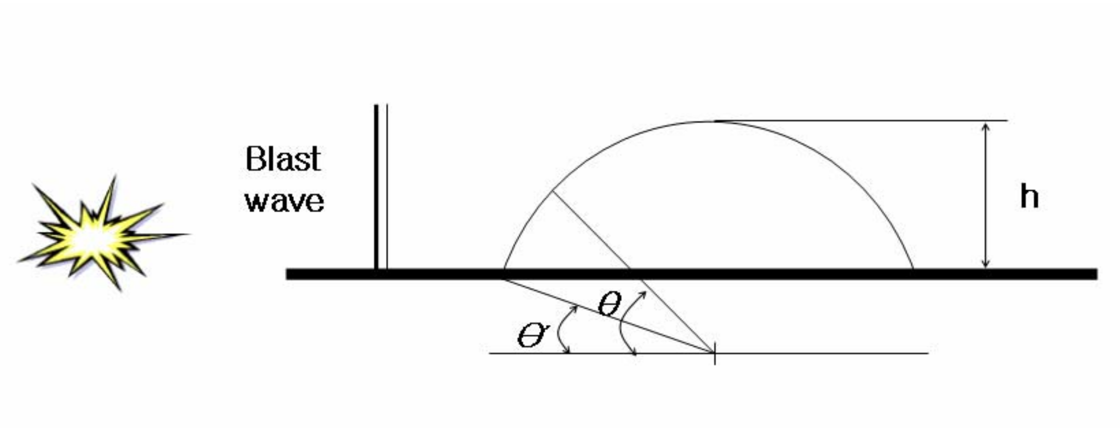

Figure 2.5 Definition sketch for cylindrical-arch notation

$$P_{l0} = P_{s0}(1.5 - \frac{\theta}{180}) \tag{2.13}$$

where P_{l0} means a leeward-side peak overpressure and θ is a clockwise angle from the horizon to an arbitrary location as defined in Figure 2.5. For leeward sides, the range of θ is from 90 to 180 degrees. This simple correction needs to be improved for a more accurate estimation.

2.3 Overpressure Profiles

Once the airblast parameters, such as a peak overpressure P_{s0}, a duration time of the positive overpressure t_0, and an arrival time of the blast wave front t_a, have been determined as discussed in Section 2.2, they can be used to generate an overpressure profile as shown in Figure 2.1 using approximate model equations such as the Flynn's linearly decreasing model, the Ethridges's exponentially decreasing model, and the Friedlander's Equation (2.1), *etc.*[18,19]. However, since the BLAST.f program employed the modified Friedlander's equation to generate the overpressure profile and it is still used to generate side-on or incident overpressure profiles, it is introduced first. Then the diffracted overpressures porfiles on the leeward side and the reflected overpressures profiles over flexible structure are newly proposed.

2.3.1 Side-On or Incident Overpressure Profiles

For side-on or incident peak overpressures, the overpressure profiles are generated using the modified Friedlander's equation as shown below (The modified Friedlander's equation is explained in detail in Ref. [10]):

$$P = P_{s0}\left(1 - \frac{t - t_a}{t_0}\right)e^{-\frac{t - t_a}{\Theta}} \tag{2.14}$$

where P_{s0} is a side-on peak overpressure for any overpressure profile. In this modification, a modified decay coefficient, Θ, is added, defined as follows:

$$\Theta = \frac{t_0}{b - \cfrac{b^2 - \frac{P_{s0}}{I}\left(b + e^{-b} - 1\right)}{2b - \frac{P_{s0}}{I}\left(1 - e^{-b}\right)}} \tag{2.15}$$

$$I = \frac{P_{s0} t_0}{b}\left[1 - \frac{\left(1 - e^{-b}\right)}{b}\right] \tag{2.16}$$

where b is the decay coefficient which is determined numerically by the fixed point iteration method of the above Equation (2.16), P_{s0} is the side-on peak overpressure, t_0 is a duration time of the positive phase, and I is the specific impulse which is obtained from airblast parameters by Kingery and Bulmash.

2.3.2 Leeward-Side or Diffracted Overpressure Profiles

For leeward-side or diffracted peak overpressures, the overpressure profiles are generated using Equation (2.17) as shown below (The leeward-side flow field is explained in detail in Ref. [17]):

$$P_s = P_{s0}(1.5 - \frac{\theta}{180})\left(1 - \frac{t - t_a}{t_0}\right)e^{-\frac{t-t_a}{\Theta}} \tag{2.17}$$

where P_{s0} is a side-on peak overpressure, Θ is defined in Equation (2.15), and θ is explained in Figure 2.5. Compared to the side-on overpressure profiles, the difference is only the peak overpressure, which was explained earlier. For leeward sides, the range of θ is from 90 to 180 degrees.

2.3.3 Windward-Side or Reflected Overpressure Profiles

For windward-side or reflected peak overpressures, the overpressure profiles are a little complicated due to the reflection effect. Figure 2.6 and Figure 2.7 are two examples[17,140] of reflected overpressure profiles which have two separate regions, of which the earlier part represents the reflected overpressure dominant region and the other represents the side-on overpressure dominant region.

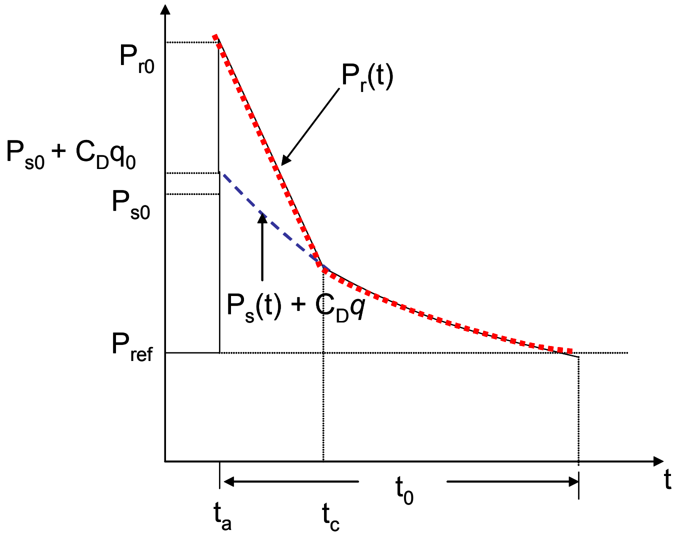

$$t_c = \frac{4h}{a_{refl}} \text{ or } \frac{3h'}{a_{refl}}$$

$$q = 14.7\left[\frac{5/14(P_s/14.7)^2}{1+1/7(P_s/14.7)}\right]$$

$$a_{refl} = 422\sqrt{\frac{1.088P_{s0}^2 + 70P_{s0} + 720}{102.9 + 6P_{s0}}}$$

Figure 2.6 Reflected overpressure profile divided into two region using a time for clearing reflection effect, t_c

In Figure 2.6, P_{r0} is a peak reflected overpressure, C_D is local drag coefficient, q is dynamic pressure, t_c is a time for clearing reflection effect, h or h' is clearing height, and a_{refl} is the velocity of sound in the reflected region.

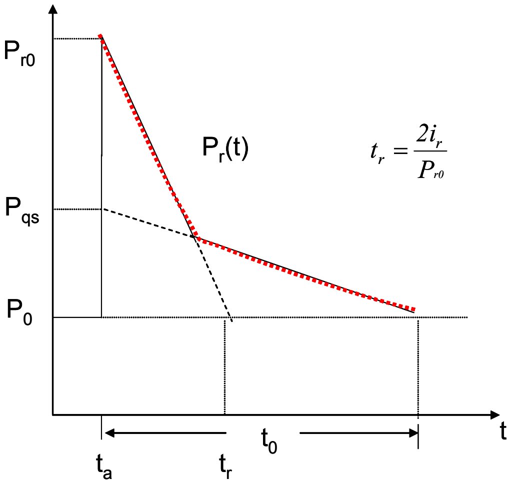

Figure 2.7 Reflected overpressure profile divided into two region using a duration time for reflected overpressure, t_r

In Figure 2.7, P_{r0} is a peak reflected overpressure, P_{qs} is a peak quasi-static overpressure, t_r is a duration time for reflected overpressure, and i_r is the magnitude of impulses in the reflected region.

Based on those reflected overpressure profiles and the test data supplied by the U.S. Air Force Research Laboratory, a reflected overpressure profile model equation is proposed as follows:

$$P_r = P_{r0}\left(1-\left(\frac{t-t_a}{t_0}\right)^R\right)e^{-S\left(\frac{t-t_a}{t_0}\right)} \qquad (2.18)$$

where two parameters, *R* and *S*, are introduced into the original Friedlander's modeling equation to generate more detailed reflected overpressure profiles for structures with a flexible skin. R is named after the reflected overpressure and S is named after the side-on overpressure, since the parameter *R* controls the reflected overpressure dominant region and the parameter *S* controls mainly the side-on overpressure dominant region. Figure 2.8 shows the simplified overpressure profile example generated by Equation (2.18).

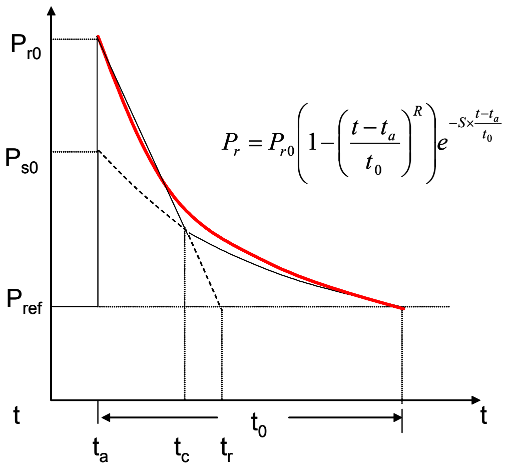

Figure 2.8 Reflected overpressure profile used in BLAST2.f

2.4 Reduction Factor Method

Structural movement of a TEMPER tent due to the external airblast loading causes air inside the tent to move and generates transmitted blast wave loading inside the structure. This is an example of fluid-structure interaction[13]. As shown in Figure 2.9, due to the dynamic response of the flexible structure to the external blast loading over side 1, an external blast wave is transmitted inside the closed flexible structure. The pressure loads generated by this transmitted blast wave on side 4 may be one of the important causes for the material failure of the XM28 liner inside the TEMPER tent.

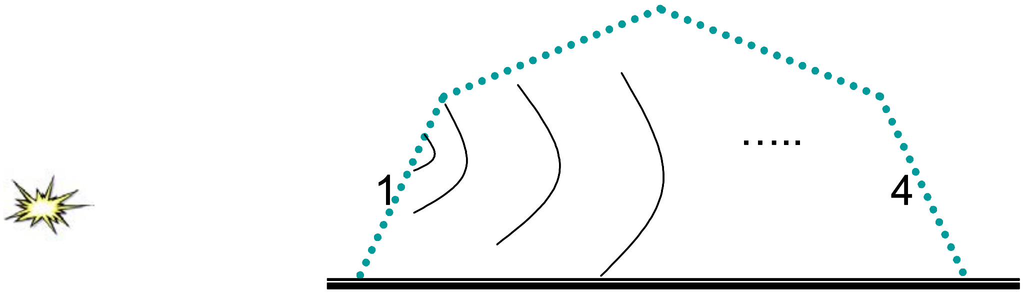

Figure 2.9 Transmission of external blast wave inside a flexible tent structure

In the present reduction factor method, the limited experimental data were examined to estimate the transmitted blast wave loading as shown in Figure 2.9. From this examination, it was found that the peak overpressures measured behind the flexible wall were less than the peak overpressures measured almost at the same distance without any interference. Therefore the reduction factor is introduced to model quantitatively the reduced peak overpressures in both side-on and reflected peak overpressures. Since the reflected overpressures are the blast loading against the interior side of the wall on side 4 in Figure 2.9, reduction factors were calculated only for the reflected peak overpressures using an error function in two ways as shown in Equations (2.19) and (2.20):

$$RF_{measured}(\%) = \frac{(P_{measured\ with\ a\ wall} - P_{measured\ without\ a\ wall})}{P_{measured\ without\ a\ wall}} \times 100 \tag{2.19}$$

$$RF_{estimated}(\%) = \frac{(P_{measured\ with\ a\ wall} - P_{estimated\ without\ a\ wall})}{P_{estimated\ without\ a\ wall}} \times 100 \tag{2.20}$$

In Equation (2.19), reference peak overpressures are also measured peak overpressures, but in Equation (2.20), reference peak overpressures are estimated using the BLAST2.f program. Neglecting the reduction factor of -25% which was calculated with Equation (2.19) and in which case the reference peak overpressure shows measurement uncertainty due to a large difference between the measured values from the same experimental conditions, the average reduction factor for both measured and estimated results is 45%. Considering various different experimental conditions and limited data, this reduction factor method should be studied more in detail, but in the present work it is compared to both the measured and numerically obtained data, as explained in Section 5.2.

Table 2-2 Experimental data for reduction factor in analyzing the transmitted blast wave loading inside a flexible structure

TNT(lb)	Distance (ft)	Test		BLAST2.f(CONWEP)		Reduction Factor	Wall
		Pr(psi)	Ps(psi)	Pr(psi)	Ps(psi)		
6600[142]	268	11.3		11.1	5.1		No
	277	5.8		10.5	4.8	-49%, -45%	Yes
	263	6.1		11.5	5.2		No
	276	4.6		10.6	4.8	-25%, -57%	Yes
6.57[3]	11	93	48	97.4	29.1		No
	11	56	23	97.4	29.1	-40%, -43%	Yes
	14	58	32.5	49.5	17.2		No
	14	32	13	49.5	17.2	-45%, -35%	Yes

2.5 BLAST2.f Program

BLAST2.f is a program written in FORTRAN 77 to determine the airblast parameters and overpressure profiles based on Kingery and Bulmash's data set and Friedlander's equation. This program, which is capable of calculating the airblast pressure loading over a flexible structure including the leeward side, was modified from the original program BLAST.f written by Chock and Kapania in modular form to examine the two different methods for determining explosive airblast parameters and blast pressure profiles. It is a user input file driven program in which all pertinent run parameters are put into the input file titled BLAST.INP. BLAST.INP requires the input of type of method used (CONWEP), the normal distance in inches, the charge weight in TNT equivalent, type of output desired (airblast or hemispherical surface burst/mine blast), time step controls, the reflected overpressure profile parameters, the incident angle for leeward-side overpressure, and the radial values (x and y coordinate pairs are converted to radial values) of the loading areas from the point normal to the blast center.

After the reading of the user input file, the program goes to the subroutine duplicating Kingery and Bulmash's data set. This subroutine first determines the correct airblast parameters, then the blast profiles, and these are stored in a subroutine passable array structure. These profiles, one for each loading area, are then output to the file BLAST.OUT, in English units. The program has the option for making an adjustment of reflected pressure waves with varying angles of incidence, but does not determine if the areas given to the program lie within the area for which normal reflection of blast waves occurs.

BLAST2.f makes use of the information in Figure 2.4 such that the determined blast pressures have a correction in the reflected peak overpressure for varying incident angles of incidence on the windward side of the structure. Then depending on the input parameters to control the decay of the overpressure profile, new decay coefficients are calculated accordingly to correspond to this new reflected peak overpressure, or the modified Friedlander's equation, Equation (2.18), is used to generate the reflected overpressure profile.

The subroutine, CONWEP, makes use of Kingery and Bulmash's Log-Log curve-fitting routines for TNT scaled explosive charges. This routine makes use of a large number of arrays, all containing the appropriate curve-fitting values used in doing Kingery's Log-Log fitting. The arrays are initialized for hemispherical surface burst parameters and if the logical flag *mine* (short for mine blast) informs the routine that a spherical airblast is desired, the routine then resets the values as appropriate for the determination of the spherical airblast.

First, the Hopkinson scaled distance is determined and stored for each radial value. Then, each appropriate parameter for the determination of the complete blast profile is calculated through the use of the predetermined Log-Log curves and stored in an appropriate array. The blast decay coefficient is first determined by the use of the fixed-point iteration function DECAY, using the 'epsilon' value from the user input file, but the decay value is then converted to the modified form by way of Equation (2.15). The individual arrays storing blast parameters for each loading area are then used by the modified Friedlander's equation in Equation (2.14) or (2.18) to generate the full blast profiles over the desired time lengths using the time step controls from the input file BLAST.INP. The stored profiles are then passed to the output routine OUTFIL and stored in the outfile BLAST.OUT.

For the reduction factor method, this BLAST2.f program is used as it is. Then, the profile generated for a surface without any interfering surface in front of the surface is proportionally scaled down to reflect the reduction factor of 55%.

2.6 Applications of BLAST2.f

2.6.1 Peak Overpressures

First, the BLAST2.f program was applied to estimate side-on and reflected peak overpressures in several cases where comparisons with test data were possible. Table 2-3 shows the comparison of peak overpressures from estimations and tests. Except for the marked results which have errors more than 40%, most of the errors are within 20%. Large differences in reflected pressure in a single test may be due to measuring error in the test data. The comparison shows that the BLAST2.f program can estimate the airblast parameters such as peak overpressure in a simple way with reasonable accuracy.

Table 2-3 Comparison of peak overpressures from BLAST2.f and field tests

TNT(lb)	Distance (ft)	Test		BLAST2.f(CONWEP)		Error	
		Pr(psi)	Ps(psi)	Pr(psi)	Ps(psi)	Pr(%)	Ps(%)
55.1[141]	65	4.5	4.4	8.4	3.8	87	-14
	65	8.8	4.4	8.4	3.8	-5	-14
	65	11.1	4.4	8.4	3.8	-24	-14
	80	6.7	3.6	6	2.8	-10	-22
	100	2.4	2	4.3	2	79	0
6600[142]	267		5.2	11.6	5.1		-2
	370		3	6.5	3.1		3
	493		2	4.3	2		0
	845		0.7	2.1	1		43
	268	11.3		11.5	5.1	2	
	263	6.1		11.9	5.2	95	
6.57[3]	11	93	48	97.4	29.1	5	-39
	14	58	32.5	49.5	17.2	-15	-47
220[141]	160	4.3	2	4.3	2	0	0

2.6.2 Overpressure Profiles

In this section, BLAST2.f is applied to estimate the airblast loading over a TEMPER tent with a CPS, which is a protective system from attacks by chemical and biological warfare agents (Figure 1.1). As shown in Figure 2.10, the TEMPER tent is subjected to an external explosion of 25 kg (≒55.1 lb) TNT at a distance of 65 ft. Using BLAST2.f, the airblast loading on each wall was represented with overpressure profiles estimated at the center of each wall. In this estimation of airblast loading, side 1 and 2 are treated as windward sides, and side 3 and 4 as leeward sides.

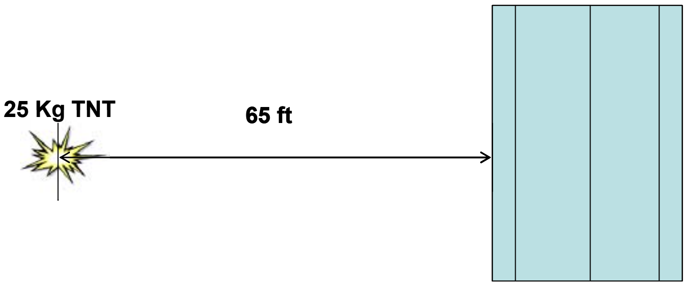

(a) Top view

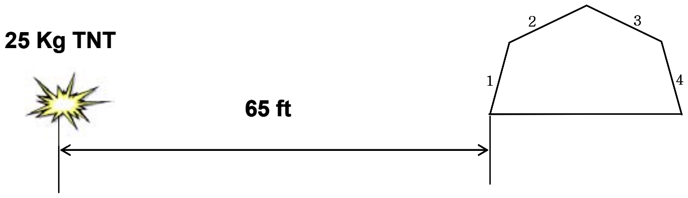

(b) 2-D axisymmetric view

Figure 2.10 Explosion test field view

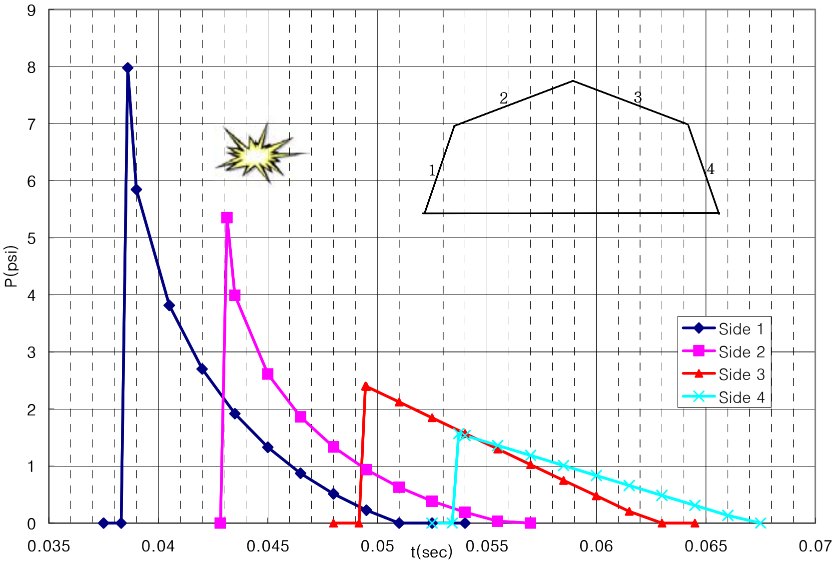

Figure 2.11 Estimated airblast loading over a TEMPER tent

Figure 2.11 shows the overpressure profiles on all the external sides of the tent. In this calculation, *R* is 0.2 and *S* is 0.65 for reflected overpressure profiles. Comparison of overpressure profiles in Figure 2.12 shows how R and S influence the overpressure profiles on the windward sides. The values of R and S used in this calculation were chosen by comparing the overpressure profiles of BLAST2.f with test data which measured the overpressure profiles on the flxible wall of the tent structure. Therefore the effect of wall flexibility was considered through the two parameters *R* and *S* in Equation (2.18).

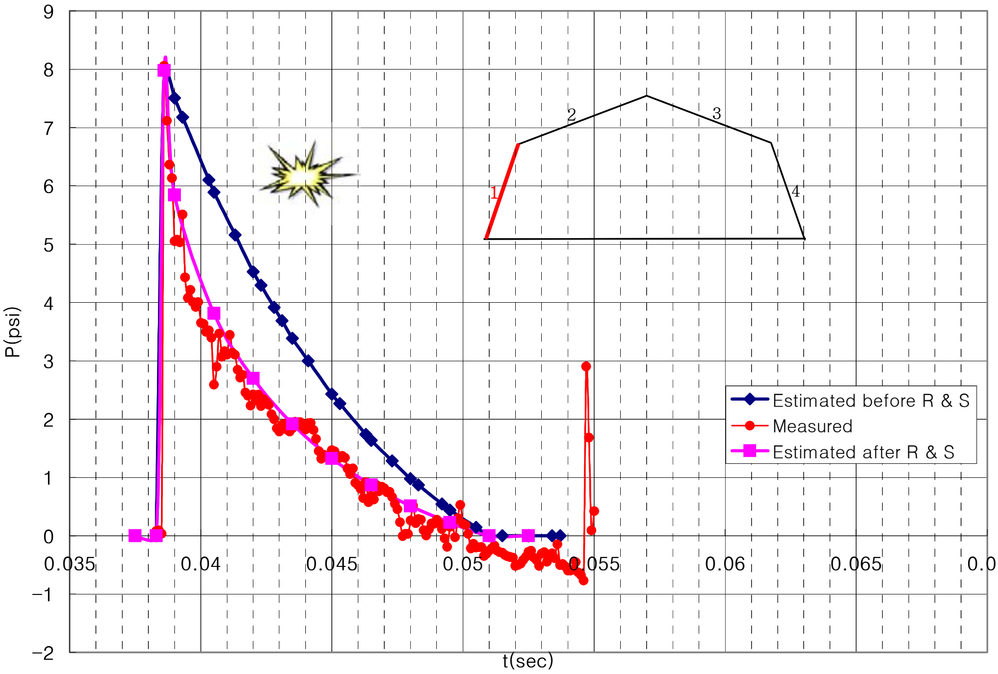
9
8
7
6
5
4
3
2
1
0
−1
−2
P(psi)
0.035
0.04
0.045
0.05
0.055
0.06
0.065
0.07
t(sec)
1
2
3
4
Estimated before R & S
Measured
Estimated after R & S

(a) side 1

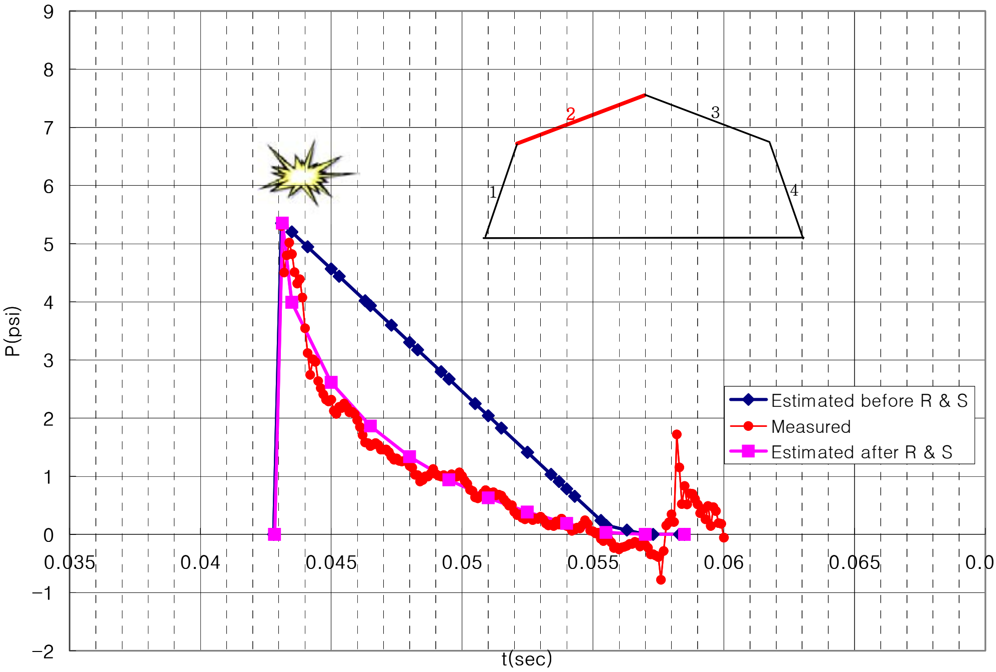
9
8
7
6
5
4
3
2
1
0
−1
−2
P(psi)
0.035
0.04
0.045
0.05
0.055
0.06
0.065
0.07
t(sec)
1
2
3
4
Estimated before R & S
Measured
Estimated after R & S

(b) side 2

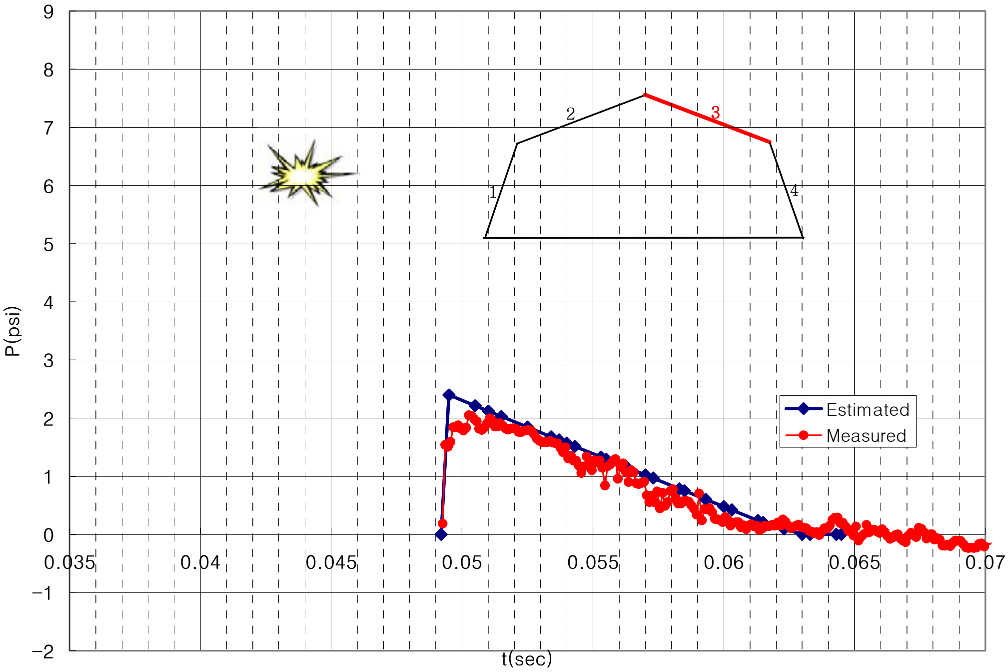
9
8
7
6
5
4
3
2
1
0
−1
−2
P(psi)
0.035
0.04
0.045
0.05
0.055
0.06
0.065
0.07
t(sec)
1
2
3
4
Estimated
Measured

(c) side 3

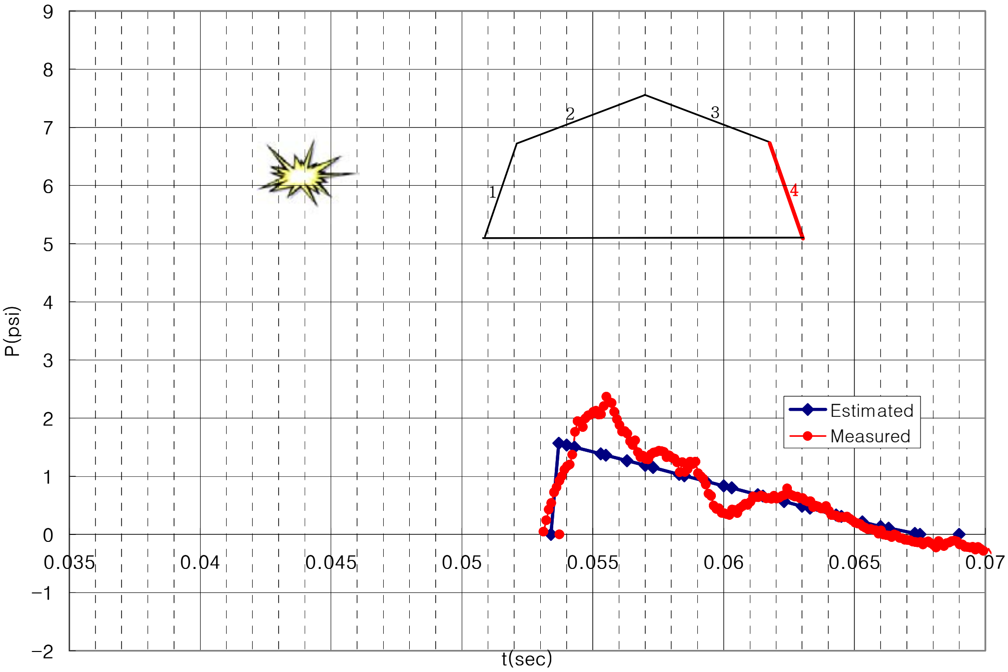

(d) side 4

Figure 2.12 Comparison of overpressure profiles; Estimated before R & S is a result obtained using the BLAST2.f program for a rigid structure, Measured is a result obtained from the field test, Estimated after R & S is a result obtained using the BLAST2.f program for a flexible structure

2.6.3 Reduction Factor Method

Using the reduction factor of 55% and the BLAST2.f program, a transmitted blast wave loading on side 4 inside the tent was calculated, and the results are shown in Figure 2.13, in which the exterior blast loading is included for the purpose of comparison. Since the experimental data for the positive duration period and the arrival time for the transmitted blast wave loading are not found, the plot is drawn using the positive duration period and the arrival time calculated for the airblast parameters without an interfering wall. The arrival times shown in Figure 2.13 are shifted arbitrarily a little behind the arrival time obtained from the calculation of the BLAST2.f program, considering the lag which may occur during the transmission. From this reduction factor method result, it is inferred that the transmitted blast wave loading inside the tent is larger than the external blast loading, even with the roughly determined reduction factor. Therefore, this shows that the transmitted blast wave may be one of the important causes of the liner failure.

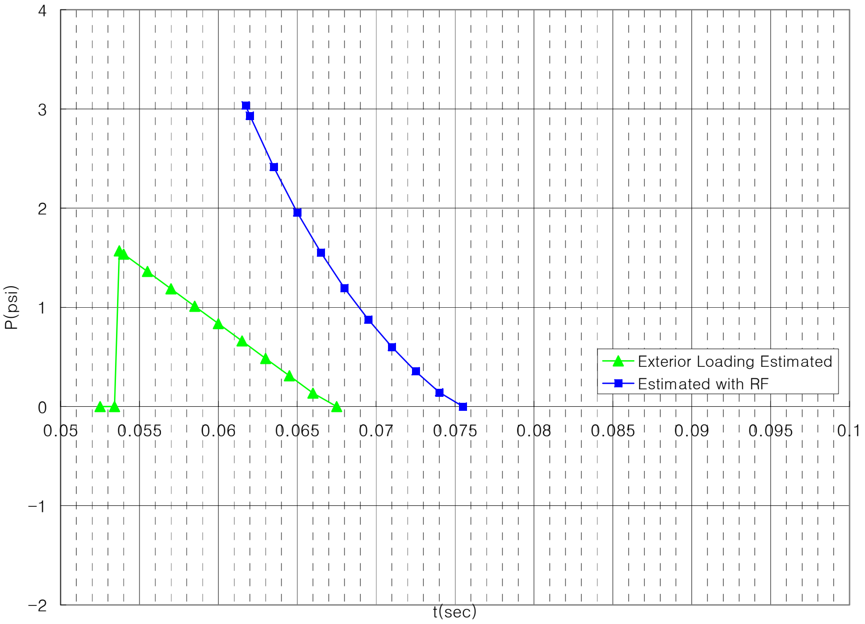

Figure 2.13 Estimation of a transmitted blast wave loading inside a tent using the reduction factor method

Chapter 3

Numerical Simulation of Blast Wave Propagation

This chapter will cover the numerical simulation of blast wave propagation in air using a commercial Computational Fluid Dynamics (CFD) code, Fluent, and the blast loading of overpressure profiles on a rigid structure. For the blast wave propagation, recent examples using various numerical methods and boundary conditions will be reviewed and they will be compared with the numerical simulation done in the present work. Finally the overpressure profiles obtained from the numerical simulation will be compared with empirical/analytical results.

3.1 Introduction

In this section, numerical methods which can numerically solve the unsteady flow field outside a structure due to the external explosion, *i.e.* simulate the blast wave propagation over the structure, are discussed.

In Section 1.2.2, the general literature about the numerical methods used to predict blast phenomena and the corresponding loading conditions on a given structure were summarized in a roughly chronological order. The computational programs originally used to carry out these numerical studies were wave propagation codes capable of analyzing the highly nonlinear and time-dependent nature of explosions,[16] *i.e.*, simulating the blast (or shock) wave propagation. Numerical methods for compressible flows, which are the groundwork for wave propagation codes, started in the 1940s-50s and can be classified into three universal methods[28]: (i) the method of finite-differences[29-31], (ii) the method of integral relations[28,32,33], and (iii) the method of characteristics[34-35]. The finite-difference method with artificial dissipative mechanisms[36-39] and the numerical method of characteristics[41-45] were commonly used methods in explosion wave calculations in the U.S. in the 1960s.[43] Due to the computational capability in those days, the finite-difference method, almost the same concept as used in the current Finite Difference Method (FDM) to solve the flow field from the Euler/Navier-Stokes equations, used artificial dissipative mechanisms to improve the numerical results with coarse grid cells. Alternatively the numerical method of characteristics applied the approximated flow characteristics and solved the simplified differential equations numerically. Aside from the basic concept in numerical methods to solve fluid flows, Hicks[49] developed the One-Dimensional Lagrangian Hydrodynamics (IDLH) solution scheme originated from the ingenious scheme of Godunov[31,50]. The hydrocode, as written in Ref. [49], could be extended to any continuum-mechanics flow problems[49,51] theoretically, and this point of view makes a difference with the numerical methods mentioned above. Hicks *et al.*[52-53] developed several Lagrangian wavecodes and hydrocodes in their internal reports in the 1970s. Therefore, as a matter of convenience, numerical methods for the blast wave propagation are roughly classified into two groups in this study: (i) CFD codes and (ii) hydrocodes.

With the rapid development of computers having high-speed and large-memory, recent movement in applying numerical methods in fluid dynamics is to solve the governing equations directly. CFD codes and hydrocodes have been actively studied and developed to show that those methods are applicable to the numerical simulation of the blast wave propagation and the ensuing blast loading over the structure to the explosion. In Section 3.2, those methods are reviewed using recently published examples.

In this numerical simulation of blast wave propagation, a commercial CFD code, Fluent, was used. First, the external flow field outside the structure was defined with a sufficiently large area where a far field pressure condition can be applied, and this region was discretized using unstructured conformal grids[11]. Second, the Euler/Navier-Stokes equations were solved for the coupled, implicit/explicit, unsteady motion of the ambient air and the pressure distribution in the discretized flow field domain. In the computation, a second-order upwind scheme was chosen for the Euler/Navier-Stokes solver, and the Courant number was set to 0.1. Finally, the blast loading over a structure under a blast wave was calculated from the pressure solved on the boundary which is defined by the structure. The CFD code, Fluent, was particularly well suited for this work due to the dynamic mesh model[11] implemented recently. The dynamic mesh model was updated at each time step by the motion of chosen moving boundaries which were predefined as functions of time and location before the computation. The moving boundary was used to define the approximate propagation of a detonation front formed by the boundary between the direct explosion-driven chemical reaction region and the induced flow field region surrounding the explosion. The arbitrary definition of the pre-defined rate of motion of the moving boundary was obtained by repeated trials of numerical simulation and comparison of the blast loading over the structure between the numerical simulation and the estimation using BLAST2.f.

3.1.1 Summary of CFD Codes

Fluid mechanics is an extensive subject encompassing widely diverse fluid flow problems[144]. The mathematical descriptions to solve these problems have been well established, even though the mathematical modeling is still an important research area. The equations governing the fluid flow problem are the continuity equation, the Euler/Navier-Stokes equations, the energy equation, and the equation of state[144]. The continuity equation is derived from conservation of mass[144]; the Euler/Navier-Stokes equations are derived from Newton’s second law[144]; the energy equation is derived from the law of conservation of energy[144]; and the equation of state is a functional relation between thermodynamic state variables[144]. These equations form a system of coupled non-linear PDEs to be solved with the boundary conditions obtained for the specific problems.

These equations, however, are classified or simplified into different sets of equations prior to attempting their solution, in general with respect to speed and viscosity. Incompressible, low-speed, inviscid flows are governed by the Laplace equation (derived from the continuity equation) for the velocity potential which is a partial differential equation of elliptic type. The problems in this range are closed with Dirichlet or Neumann boundary conditions (or both). The equations for subsonic compressible inviscid flows are still elliptic as long as the entire flow field is subsonic. They switch to hyperbolic in the supersonic pockets defined by the shock waves. The equations for inviscid, supersonic flows are of the hyperbolic type, therefore they require initial data in a time marching solution. Viscous flows are of a wide variety of their own. The classical boundary layer equations (Prandtl) are of the parabolic type and require initial conditions at one end of the integration domain. The additional viscous terms to the Euler equations can be approximated by an appropriate numerical differentiation technique. The Navier-Stokes equations that are usually solved for turbulent flows are in fact Reynolds-averaged equations, due to the large disparity of length scales between turbulence and integration domains. This additional viscous term in the Navier-Stokes equations is usually represented by various turbulence models and considerable effort has been devoted to the construction of approximate turbulence model as an important research area in computational models of fluid flow.

Because of the non-linear terms in these Partial Differential Equations (PDEs), however, few problems are solved analytically. In general, analytical solutions are possible only if these PDEs can be approximated to be linear in cases of fluid flow problems where non-linear terms naturally drop out (*e.g.*, fully developed laminar flows in ducts and plates), or where non-linear terms are very small compared to other linear terms so that they can be neglected (*e.g.*, creeping flows, small-amplitude sloshing of liquid, *etc.*). If the non-linearities in the governing PDEs cannot be neglected, which is the situation for most engineering fluid flow problems, then numerical methods are considered as alternatives to obtain solutions. All of the numerical methods are the process of replacing the PDEs governing the fluid flow fields with a set of algebraic equations (the process is called discretization), but the field is so broad as to include convergence acceleration methods (multi-grid, relaxation, artificial viscosity, etc.), stability control, and pre-conditioning. These numerical method, in which nonlinear algebraic equations can be solved with the aid of a digital computer to get an approximate solution in the fluid flow problems, are regarded as CFD from a wide point of view.

Depending upon the discretization method and concerned sets of governing PDEs, CFD is broadly classified into a few groups: (i) Finite Difference Method (FDM), (ii) Finite Volume Method (FVM), (iii) Boundary Element Method (BEM), and (iv) Finite Element Method (FEM). FDM is one of the most commonly used methods in CFD applications in transonic potential flows and the compressible-viscous flows governed by the Euler/Navier-Stokes equations. In FDM, the flow field domain including the boundary of the physical problem are usually covered by a grid or mesh. At each of the interior grid points, the original PDEs are replaced by equivalent finite difference approximations. In making this replacement, a numerical error which is related to the size of the grid is introduced. Specially, the treatment of the additional viscous terms in the Navier-Stokes equations is presently one of the great difficulties in CFD. FVM can be regarded as an alternative to FDM in the similar flow problems solved by FDM. However, FVM is based on the integral formulation of the conservation laws applied to each control volume which usually discretize the flow field domain with triangles or quadrilaterals in 2D and tetrahedra or hexahedra in 3D. Then, integral formulations of the conservation laws are approximated in terms of chosen degrees of freedom in the control volume. BEMs methods (panel methods) or FEMs are usually used for incompressible, low-speed, inviscid flows governed by the Laplace equation (derived from the continuity equation) for the velocity potential. On the other hand, numerical methods for compressible flows started in the 1940s-50s and could be classified into three universal methods[28]: (i) the method of finite-differences (developed to FDM)[29-31], (ii) the method of integral relations (developed to FVM)[28,32,33], and (iii) the method of characteristics[34-35]. The finite-difference method with artificial dissipative mechanisms[36-39] and the numerical method of characteristics[41-45] were commonly used methods in explosion wave calculations in the U.S. in the 1960s.[43]

This brief summary is hardly sufficient to cover the continually expanding world of CFD. Besides countless articles in archival journals, there are many excellent books classified into various categories devoted only to numerical schemes for a wide range of equations. Therefore, it is not the purpose of this simple review to be comprehensive. Those who are really interested in learning CFD are referred to the books, including Refs [143, 145-147] used for this very brief review.

3.1.2 Summary of Hydrocodes

It was mentioned previously that ever since Hicks[49] developed the IDLH solution scheme to simulate the shock wave propagation, hydrocodes could be extended to any continuous flow problems[49,51]. In fact, hydrocodes theoretically make fewer approximations than the more special-purpose CFD codes, and they numerically solve more fundamental time-dependent equations of continuum mechanics. This point of view makes hydrocodes different from CFD codes. Therefore, hydrocodes are defined as analysis programs for the simulation of multi-material, compressible, transient continuum mechanics, and can be called Computational Continuum Mechanics (CCM) codes[58]. However, the continuing development of CFD and hydrocode capabilities tends to make the distinction between CFD and hydrocodes unclear. Some hydrocodes have even implemented the capability of modeling structural dynamics to expand the applicability to determine structural response and fluid-structure interaction problems so that those codes can simulate the response of both solid and fluid material under highly dynamic conditions in which blast wave propagation is a dominant feature. In this section, Lagrangian, Eulerian, Coupled Eulerian-Lagrangian (CEL), and Arbitrary Lagrangian-Eulerian (ALE) hydrocode methods are briefly explained before the description of the recent application of an explicit finite element code, LS-DYNA, for an airblast simulation.

- Lagrangian hydrocodes

A Lagrangian description for an individual fluid element in the flow fields means[144] that in Lagrangian hydrocodes the finite element meshes used to discretize continuum fields are fixed to the material, *i.e.*, deforming or moving together with the material. Therefore, the computation is relatively straightforward and fast, since the mass within each element mesh is constant and the computation of mass flux across mesh boundaries is unnecessary. Material deformations correspond to distortions of mesh elements. But, these distorted mesh elements cause numerical errors and stability problems, and the time step to avoid these problems may be reduced to unacceptably low values, increasing the computation time rapidly and in effect making the calculation impractical.

To solve this unfavorable mesh evolution problem in the process faced when using quadrilateral elements (six-sided “hexahedral” elements in 3D), triangular elements (four-sided “tetrahedral” elements in 3D) were used to allow as large distortions as possible. Alternatively, mesh re-zoning[58] was adopted. But, these attempts introduce additional computational complexities and inaccuracies, and the numerical problems would still exist in Lagrangian hydrocodes. The calculation method is also, strictly speaking, no longer Lagrangian conceptually if the meshes are re-zoned. This general problem of most Lagrangian hydrocodes limits their applicability to relatively low-deformation problems such as shock–structure interaction analysis[58]. Considering these limitations, the traditional (implicit) CSD FEM codes like ANSYS[134] can be good alternatives. In that case, however, the dynamic loading conditions acting on the structure should be adjusted to some degree in advance for including the Fluid-Structure Interaction (FSI) effects. This is one of the main research topics in this dissertation and will be illustrated in Chapter 5.

- Eulerian hydrocodes

An Eulerian description for the space filled by the flowing fluid with fluid properties as a function of time means[144] that in Eulerian hydrocodes the finite element meshes used to discretize continuum fields are fixed to the space instead of mesh elements fixed to the material, as is done in a Lagrangian solution. With the fixed shape of mesh elements, Eulerian hydrocodes avoid the problem of mesh distortions in Lagrangian hydrocodes such as numerical errors, stability problems, and the unreasonably small time step in advancing in time for computational solutions. These computational methods are similar to general CFD codes except that Eulerian hydrocodes do not limit the flow field media to fluids; Eulerian hydrocodes can include media of structural properties and even multi-material capability in the flow field modeling.

Moreover, since hydrocodes are developed for transient dynamics solvers from the beginning, while CFD codes are mostly designed to solve steady flow problems first, the computational methods for the solution in each time step are basically different. In Eulerian hydrocodes, there are two separate phases for the usual solution process for each time step: (i) solving the equations of motion based on the Lagrangian description for all the mesh elements, and (ii) restoring the deformed and moved meshes to their original shape[58], *i.e.*, advecting the material over the fixed meshes based on the results of phase (i). Phase (ii) requires sophisticated algorithms that can strongly influence the solution and require additional computational cost. The convergence of flow field properties such as pressure within a multimaterial cell can also result in considerable computational cost, particularly if the higher order accuracy of the Lagrangian phase is to be retained. On the other hand in usual CFD codes, the media flow through the boundaries of the fixed mesh elements in each time step by solving the Euler or Navier-Stokes equations of motion in their Eulerian form. As mentioned above, cells (or elements) containing more than one material are common in Eulerian hydrocode computations; the presence of multiple fluid and/or solid materials within a cell is the main reason that Eulerian hydrocodes are computationally expensive, and distinguish Eulerian hydrocodes from CFD codes. This situation necessitated additional numerical algorithms that prevent artificial material diffusion (the mixing of materials across a material interface) within these mixed cells and finally led to CEL hydrocodes.

- CEL hydrocodes

Lagrangian hydrocodes have been successfully coupled and linked to Eulerian hydrocodes such that large-distortion fluid dynamics calculations can be made within an Eulerian hydrocode, and detailed structural calculations can be made within a Lagrangian hydrocode. When both Eulerian and Lagrangian methods are employed in their most advantageous computation modes in separate (or overlapping) regions of the domain, the result can be called CEL hydrocodes.

One recommended coupling scheme concerning the application of the CEL hydrocodes is to connect solid-type materials in a Lagrangian hydrocode and fluid-type materials in an Eulerian hydrocode separately. As the numerical solution advances in time, the motions of solid-type mesh elements calculated by Lagrangian methods interact continuously with the motions of fluid-type mesh elements calculated by Eulerian methods, allowing true fluid-structure interaction. Therefore, a typical CEL hydrocode actually comprises three modules: Eulerian hydrocode, Lagrangian hydrocode, and

Coupling. The Coupling module handles the interacting information between the Eulerian and Lagrangian hydrocode modules and it has been developed in several ways.

- Arbitrary Lagrangian-Eulerian (ALE) hydrocodes

Arbitrary Lagrangian–Eulerian (ALE) hydrocodes use aspects of both Lagrangian and Eulerian hydrocodes: (i) solving the equations of motion based on the Lagrangian description for all the mesh elements, and (ii) remapping the spatial mesh elements by maintaining the Lagrangian motions, by advecting the material over the fixed original meshes in Eulerian methods, or by evolving new meshes to avoid numerically unfavorable mesh shapes. The mesh remapping schemes in ALE hydrocodes are based primarily on maintaining more uniform meshes. The ALE method provides a way of coupling fluid dynamics to structural dynamics without interfacing separate sets of material elements as is done in the Coupled Eulerian–Lagrangian method. The efficiency to be gained by straightforward coupling is probably significant. In cases where structural elements can be incorporated directly within the ALE framework, the coupling is trivial. In cases where the ALE numerical method cannot incorporate structural elements, the coupling can be effected through a continuous transfer of boundary conditions. Structure–medium coupling is generally more efficient in ALE hydrocodes than in CEL hydrocodes.[58]

3.2 Recent applications

As mentioned above, with the advanced computer technology, recent movement in applying numerical methods in fluid dynamics is to solve the governing equations directly. In this section, some examples, which have been recently published in the field of blast wave propagation using numerical methods, are reviewed in a greater detail and the results from these example will be compared with the result from the present research in which a CFD code, Fluent, is used in simulating explosion problems and its blast loading on a given structure derived from the simulation. These examples are divided into two groups, according to the types of numerical methods used: (i) CFD codes and (ii) hydrocodes.

3.2.1 Blast Wave Propagation using CFD Codes

From a broad point of view, CFD includes all the numerical methods which are related to solving the fluid flow problems and loading conditions acting on the structure resulting from the motion of fluid flow. In this section, CFD implies a numerical solution of the Euler/Navier-Stokes equations for the discretized flow field of structured or unstructured meshes or grids[11].

Ofengeim and Drikakis[70] solved the Euler/Navier-Stokes equations using an adaptive grid method and a second-order Godunov scheme to simulate planar blast-wave propagation over a cylinder. They used an initial pressure difference in the fixed flow field domain to induce the wave propagation. The flow field was discretized by a hybrid structured-unstructured grid approach and an adaptive mesh method. Fig. 2 in Ref. [70] shows the flow field geometry, initial conditions, and boundary conditions.

Fig. 4 in Ref. [70] shows overpressure profiles obtained at the locations of a leading edge, center, and a trailing edge of a cylinder in the computation without the cylinder. Therefore, these overpressure profiles are side-on overpressure profiles which are compared with the corresponding reflected or diffracted overpressure profiles. In the present work, only a short positive phase case is studied since the overpressure profiles are similar to the ones in our study as explained in Chapter 2. It should be noted that the overpressure profiles have a second shock for a short positive phase case. Fig. 7a-b in Ref [70] shows the flow field after the blast wave passed the cylinder. From the figure, at an early time instant, the blast wave does not lose its momentum, since it is a transient flow contrary to the fully-developed steady flow which shows momentum loss due to the separation at the leeward side. From Fig. 9a-b in Ref. [70], at an later time instant, it is possible to see that a second shock develops.

From Fig. 7a-b in Ref. [70], it is confirmed that the selection of a viscous solver (Navier-Stokes) or an inviscid solver (Euler) does not make a significant difference to the results. Fig. 11 in Ref. [70] shows the pressure profiles at different positions of the cylinder surface. In the case of a short duration of positive phase, there is almost no difference between viscous and inviscid results. In the case of ψ=90°, *i.e.* at the top of the cylinder, the peak overpressure is almost the same as the peak overpressure in Fig. 4 in Ref. [70]. Therefore, with an incident angle of 0°, the peak overpressure on the surface can be considered as a side-on overpressure. The case of ψ=0° is considered as a normal incident angle and the numerical results show that the peak reflected overpressure is around 8.0 and the peak side-on overpressure is 3.3. This difference is consistent with the previous estimation using BLAST2.f with the peak reflected overpressure of 8.4 psi and the peak side-on overpressure of 3.8 psi, and the test data with the peak reflected overpressure of 8.8 psi and the peak side-on overpressure of 4.4 psi, in which the explosive condition is 55 lb of TNT and 65-ft distance. In the case of ψ=150°, the numerical results show two peaks in the positive phase, which is found in the test data.

Liang *et al.*[72] numerically investigated the problem of an unsteady cylindrical blast-wave interaction with a flat plate. They solved the two-dimensional Euler/Navier-Stokes equations using finite volume method with a fifth-order Weighted Essentially NonOcillatory (WENO) scheme for spatial discretization and a fourth-order Runge-Kutta method for time integration. They also used the initial conditions in the fixed flow field domain of a 400×200 grid to induce the wave propagation. The initial conditions correspond to relatively complicated state (pressure, density, and velocity) distributions inside the assumed explosion and are based on analytical solutions. The use of the fifth-order WENO scheme tends to avoid the need of using a very fine grid or adaptive grid in the flow field for resolving flow discontinuities or large gradients. Fig. 1 in Ref. [72] shows the flow field geometry, initial conditions, and boundary conditions.

Fig. 2 in Ref. [72] shows the two kinds of initial conditions, where the first kind is based on the similarity characteristics and Rankine-Hugoniot conditions, and the second kind is a nonsimilarity solution for a strong blast wave using the instantaneous energy release. The two kinds of initial conditions were tested in the free field. Since the second shock wave was developed only in the second one, *i.e.*, nonsimilar initial conditions, the second kind of initial conditions was used for the following results.

Fig. 7 in Ref. [72] shows the pressure variation with respect to time at the point (3.02, 3.0). At t =0.8 the first shock wave results in an abrupt pressure rise of about 4.55. Following the first shock front are the expansion waves, causing a rapid pressure reduction. The pressure reduction consists of two phases. The first one is a positive phase with a pressure greater than the undisturbed pressure P_0. The second is a negative phase with a pressure less than P_0. At approximately t =4.05, the secondary shock wave propagates to this location, resulting in a pressure jump. Later, the pressure decays to the undisturbed value P_0.

Finally, Liang *et al.*[72] studied the blast-wave interaction with a smooth flat plate and the interaction of the reflection of the first shock wave with the secondary shock wave. Fig. 8 in Ref. [72] shows the density ratio contours at different instants, where M_S is the initially incident shock Mach number and HOB is the height of burst.

Cler *et al.*[75] applied CFD, Fluent, and Discontinuous Galerkin (DG) codes to simulate unsteady gun muzzle blast wave propagation. They used the pressure inlet conditions in the fixed flow field domain to induce the wave propagation. The flow field was discretized by tri- or quad-grids and an unsteady non-conformal adaptive grid method (Figure 2 and Figure 3 in Ref. [75]). In their computations, Fluent required higher adaption levels and finer grids than DG to obtain accurate results.

Figure 4 in Ref. [75] shows the experimental data used for the pressure inlet boundary condition based on the measured static muzzle pressure of the North Atlantic Treaty Organization (NATO) rifle. A constant pressure, velocity, and density far-field boundary condition with values identical to the initial conditions was used.

In the comparison figures shown in Figure 7 in Ref. [75], a logarithmic density grayscale contour plot of the CFD results was used to compare to experimental shadowgraph images. Shadowgraph shows curvature of density throughout the flow field. By using a logarithmic scale for the CFD density contours, weak shock patterns such as the primary blast wave are more visible and easier to compare to experimental shadowgraph images.

Figure 18 in Ref. [75] shows variation of pressure vs. distance along the 135-degree radial line emanating from the muzzle at an instant for both Fluent and DG results. The peak overpressure and distance from the muzzle are similar for both the Fluent and DG results, indicating similar accuracy and ability to maintain shock strength for these flows.

3.2.2 Airblast Simulation using Hydrocodes

Mahmadi *et al.*[59] conducted an airblast simulation using an explicit finite element code, LS-DYNA, a hydrocode using Eulerian Multi-material and ALE formulations for the Navier-Stokes equations with the JWL equation of state for gaseous products of detonation.

The case treated in this example was a high explosive charge of 0.5 lb of composition C-4 with a radius of charge of 3.23 cm. A reflecting plane was placed at 4 ft

(121.9 cm) from the static charge. The explosive was modeled with 8-node elements. This charge model was surrounded with the air mesh such that there was a one-to-one match at the boundary between the explosive models and the air models. After the detonation, a high-velocity shock front departed from the explosive source into the surrounding air. A shock is a narrow discontinuity in the pressure wave, and therefore requires fine mesh resolution. Figure 8 in Ref. [59] shows the mesh modeling for this case with a plane wall. Figure 10 and 11 in Ref. [59] show the propagation and the reflection of the airblast wave against the wall. This shock wave is followed by the expansion of gas produced by the explosive.

Figure 5 in Ref. [59] shows the comparison of overpressure profiles from experimental data and numerical data. Peak overpressures and the arrival time are very close to each other. While the positive phase overpressure profiles are similar, the negative phases and the second shocks after the first peak overpressures need to be investigated more.

As a whole, the numerical results from four examples show that numerical methods can be used to predict the airblast wave loading quite well. These earlier studies encouraged the author to use the numerical methods with a new boundary condition to simulate the airblast wave propagation under consideration.

3.3 Blast Wave Propagation Over a Rigid Structure

In this section, the dynamic flow field outside a rigid structure, simulating the expansion of the explosive wave over the structure, is solved numerically using CFD code titled Fluent. Fluent is a commercial CFD code that can solve various kinds of fluid dynamic problems. This CFD code is particularly suited for this work due to the dynamic mesh model[11] implemented in the most recent version. The dynamic mesh model is updated at each time step by the motion of chosen moving boundaries which are defined as functions of time and location before the computation. The arbitrary definition of the pre-defined rate of motion of the moving boundary was obtained by repeated trials of numerical simulation and comparison of the blast loading over the structure between the numerical simulation and the estimation using BLAST2.f.

The case treated in this example is the same as that solved in the calculation of blast loading using BLAST2.f in Section 2.6; the TEMPER tent (Figure 1.1) is subjected to an external explosion of 25 kg (55.1 lb) TNT, 65 ft away from the explosion origin as shown in Figure 2.10. The difference is the rigidity of the structural shape in this calculation. The flexibility will be considered in Chapter 5 where the fluid-structure interaction is applied.

In this numerical simulation, the high explosive charge model is defined by the boundary condition of a moving wall in a circular shape as shown in the lower-left corner of Figure 3.1. The boundary condition of a moving wall was used to define the approximate propagation of the detonation front, formed by the boundary between the gaseous products of the detonation and the air surrounding the explosion, as shown in Mahmadi's numerical simulation of airblast wave propagation[59] using an explicit finite element hydrocode, LS-DYNA. In Mahmadi's work, the movement of the detonation front was defined implicitly by the JWL equation of state and the state of the surrounding air, but here it is defined explicitly as a function of time and location before the computation.

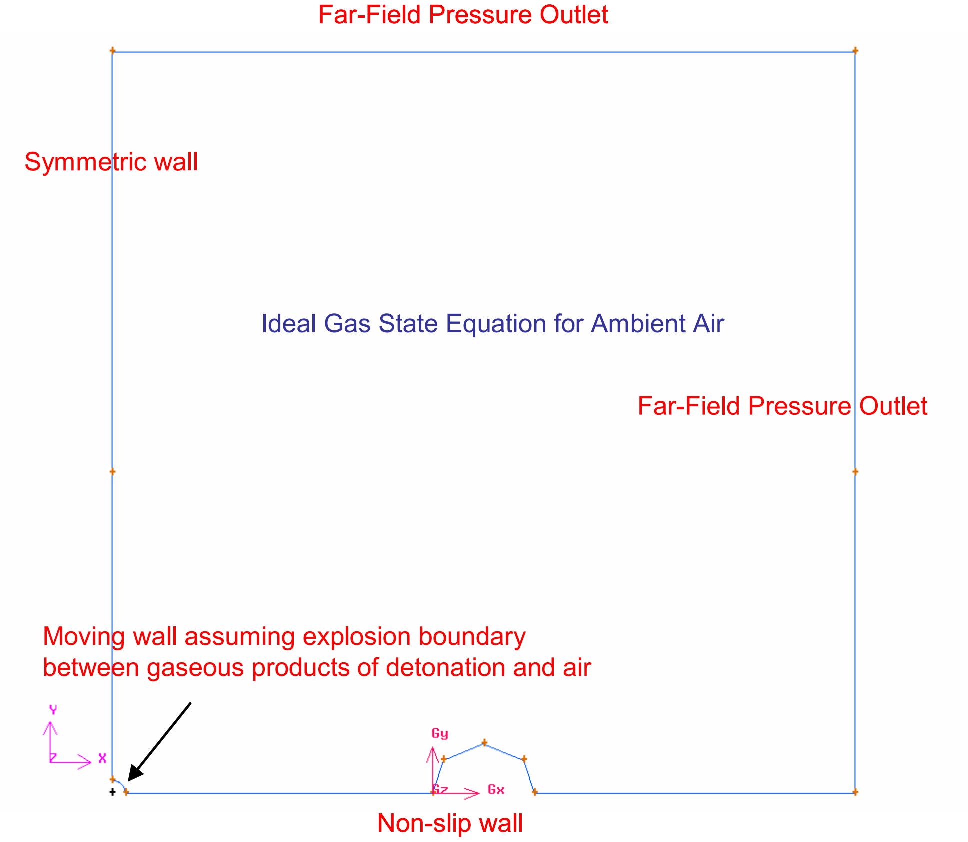

Figure 3.1 Problem geometry and initial/boundary conditions

Then, the high explosive charge and the rigid structure are surrounded with unstructured conformal dynamic meshes[11] descretizing the flow field as shown in Figure 3.2. To save computational time, refinement of the mesh is focused near the structure which experiences the blast loading, as shown in Figure 3.2. As time goes on, the moving wall varies the shape in a pre-defined way and the dynamic mesh also changes shape according to the varying shape of the moving wall.

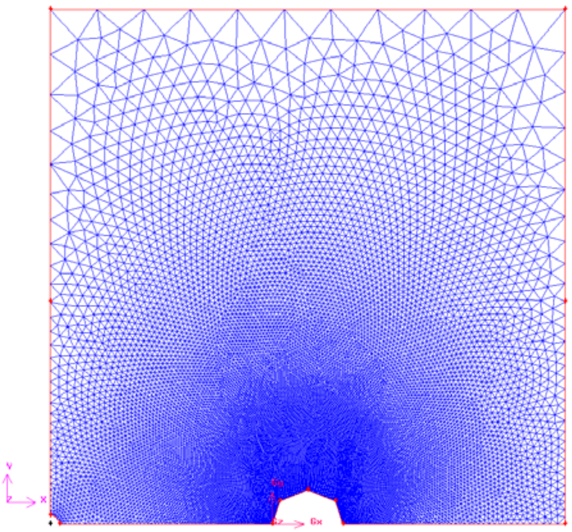

Figure 3.2 Initial flow field domain discretized in unstructured tri-grids

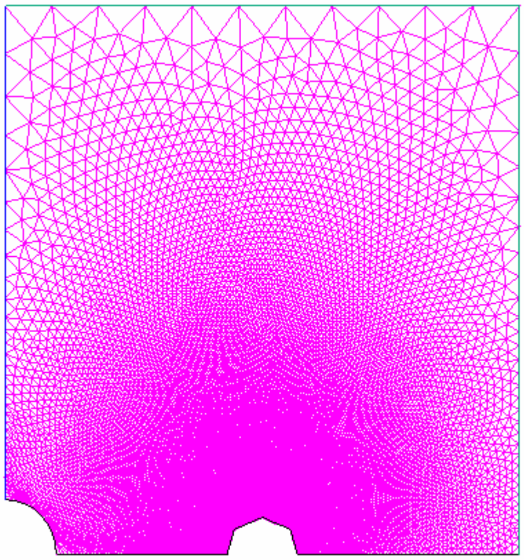

Figure 3.3 The descretized flow fiels at t = 0.06602 sec showing the changed shape of the moving wall and the dynamic meshes

As the computation is performed, the circular moving wall expands rapidly as shown in Figure 3.3 which is a discretized flow field at an instant in time, which clearly shows the changed shape of the moving wall and the dynamic meshes. The movement of the high explosive charge is defined in detail in Figure 3.4, where (a) shows a pre-defined rate of change of the radius of a circular moving wall with the maximum Mach number of 1.225, and (b) shows the radius of a circular moving wall varying over time, obtained through the numerical integration of the pre-defined rate of change of the radius of a circular moving wall. With this movement, a high-velocity shock front departs from the moving wall into the surrounding air.

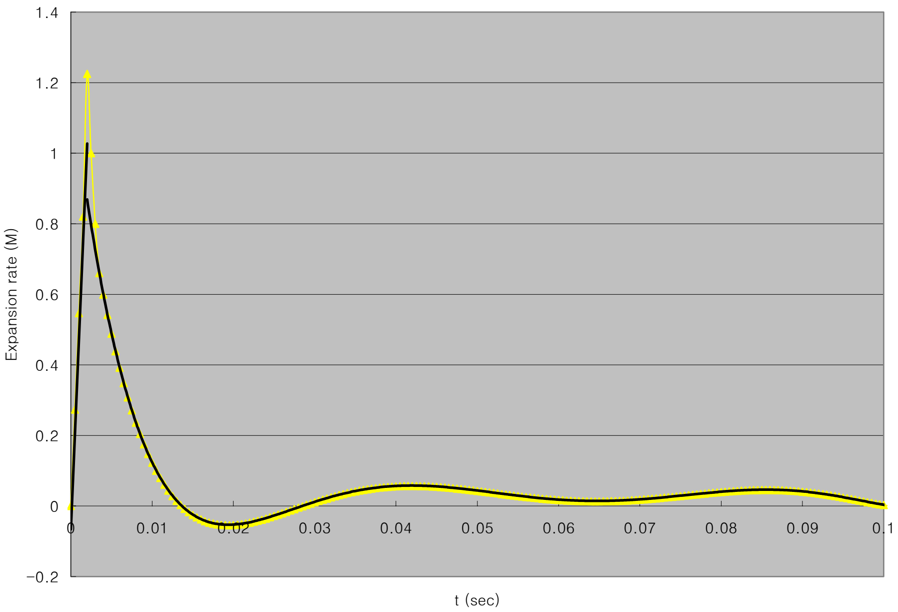

(a) A pre-defined rate of change of the radius of a circular moving wall

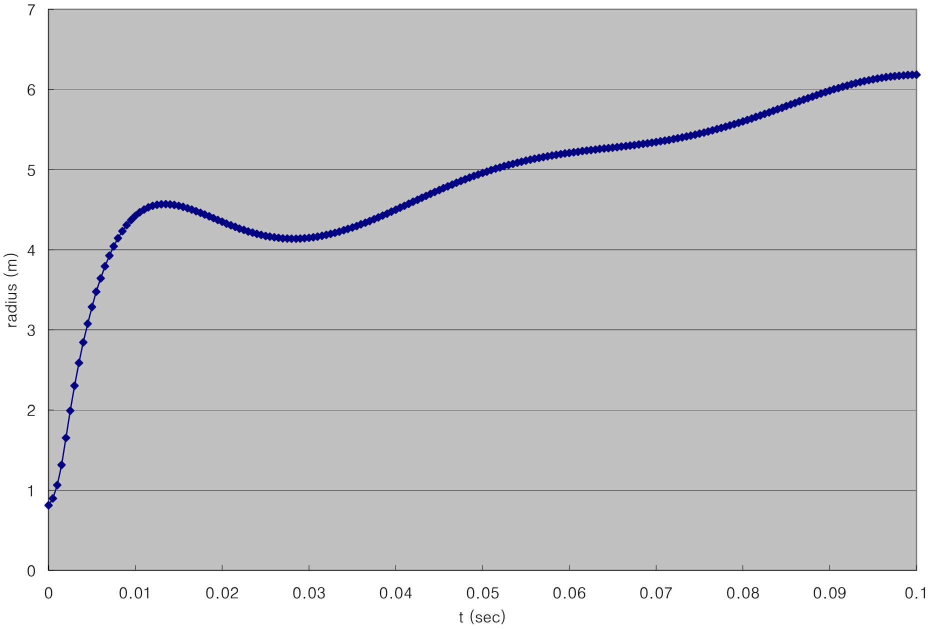

(b) The variation of the radius of a circular moving wall

Figure 3.4 A description of the circular moving wall

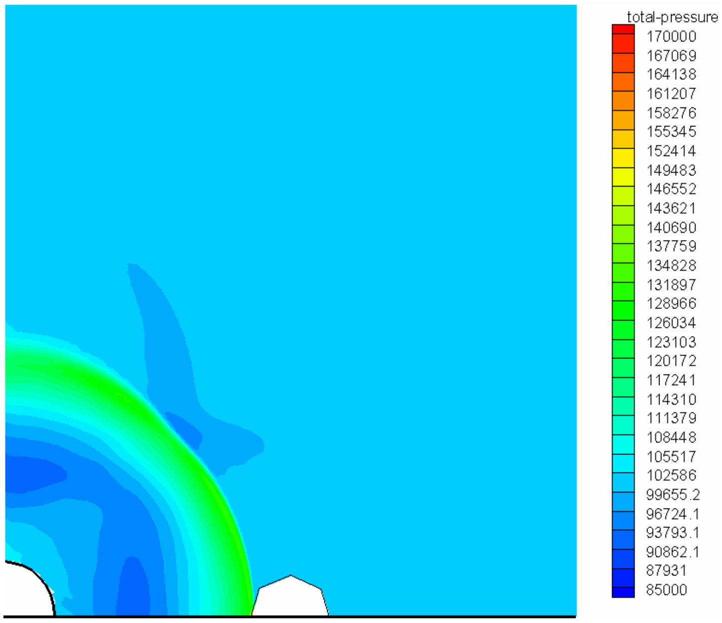

(a) 0.0428 sec

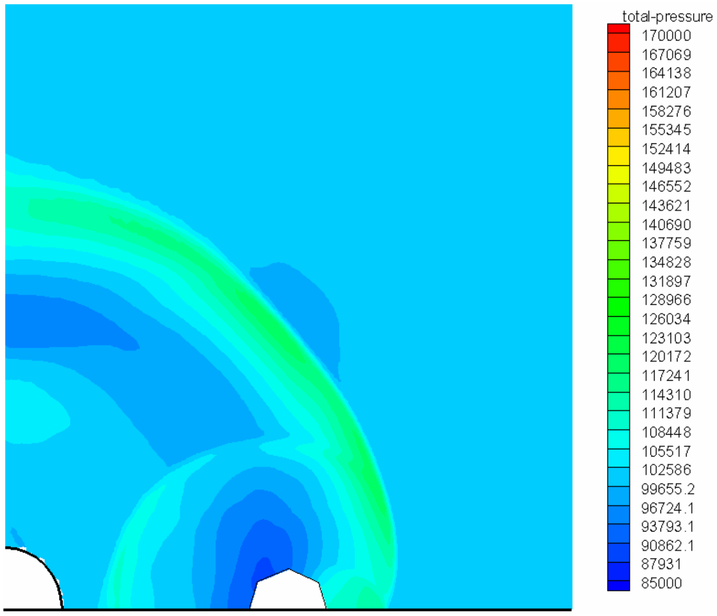

(b) 0.0661 sec

Figure 3.5 Total pressure (in psi) contours induced by a blast-wave interaction with a tent-shaped rigid structure at different instants

Then, Euler/Navier-Stokes equations were solved for the coupled, explicit, unsteady motion of the ambient air in the discretized flow field domain until the airblast shock front passed over the far-field pressure outlet walls defined in Figure 3.1. A second-order upwind scheme was chosen in the flow discretization, and the Courant number was set to 0.1. The propagation and the reflection of the airblast wave against the wall are shown in the results from this numerical solution: Figure 3.5(a) shows the flow field before the blast wave is reflected against the front wall, and Figure 3.5(b) shows the flow field after the blast wave passed over the structure. Specially, Figure 3.5(b) can be compared with Ofengeim and Drikakis's figure at an early time instant in Fig. 7a-b in Ref [70]. Both figures show the airblast wave front and the reflected wave front in the flow field, and the wave geometries are very similar to each other, considering the difference of a circular airblast wave front and a plane airblast wave front. As confirmed in Fig. 7a-b in Ref [70], it is also verified in this solution that the selection of a viscous solver (Navier-Stokes) or an inviscid solver (Euler) does not make a significant difference to the results.

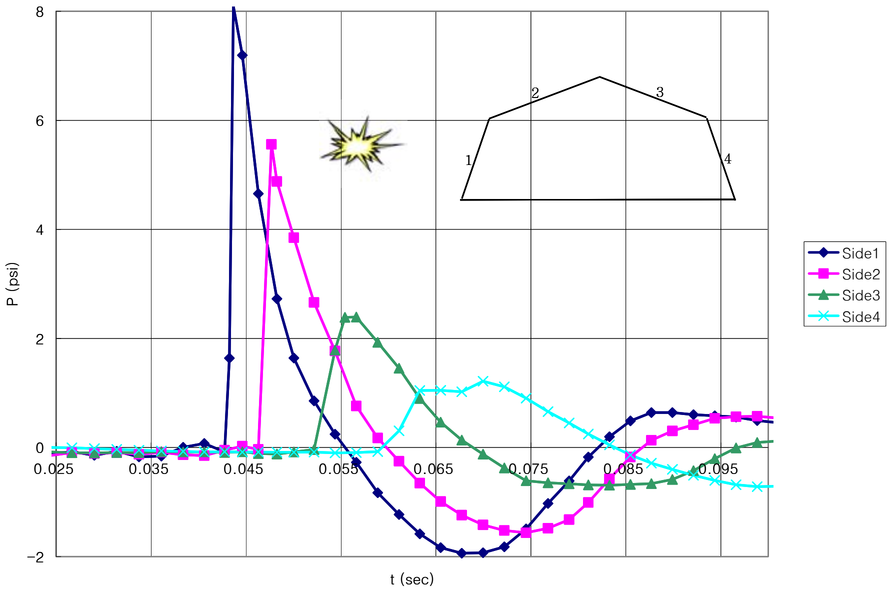

Figure 3.6 Overpressure profiles obtained from the numerical simulation using Fluent

Finally from this numerical solution, the blast loading over the whole structure can be obtained. Figure 3.6 shows the overpressure profiles calculated at the center of each wall to be compared with the estimation. As shown in other numerical solutions, the development of the second shock can be found in this numerical solution. Figure 3.7 shows the comparison of the overpressure profiles from the numerical solution and the estimation. Since the numerical solution was performed with a rigid structure, the estimated overpressure profiles are also obtained with R=S=1.0, which means that no flexibility is considered. Except at side 4, where vortex flow due to the blast wave diffraction is dominant, the results are very close to each other. In addition, the numerical solution can predict the blast loading due to the second shock.

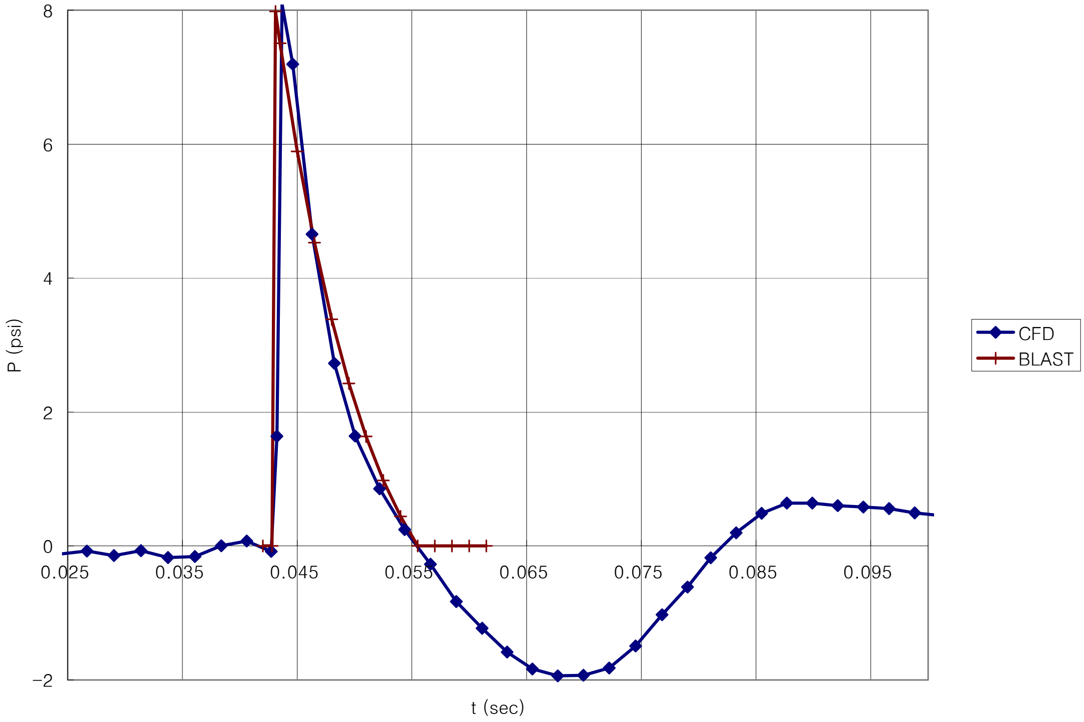
8
6
4
2
0
−2
P (psi)
0.025
0.035
0.045
0.055
0.065
0.075
0.085
0.095
t (sec)
CFD
BLAST

(a) side 1

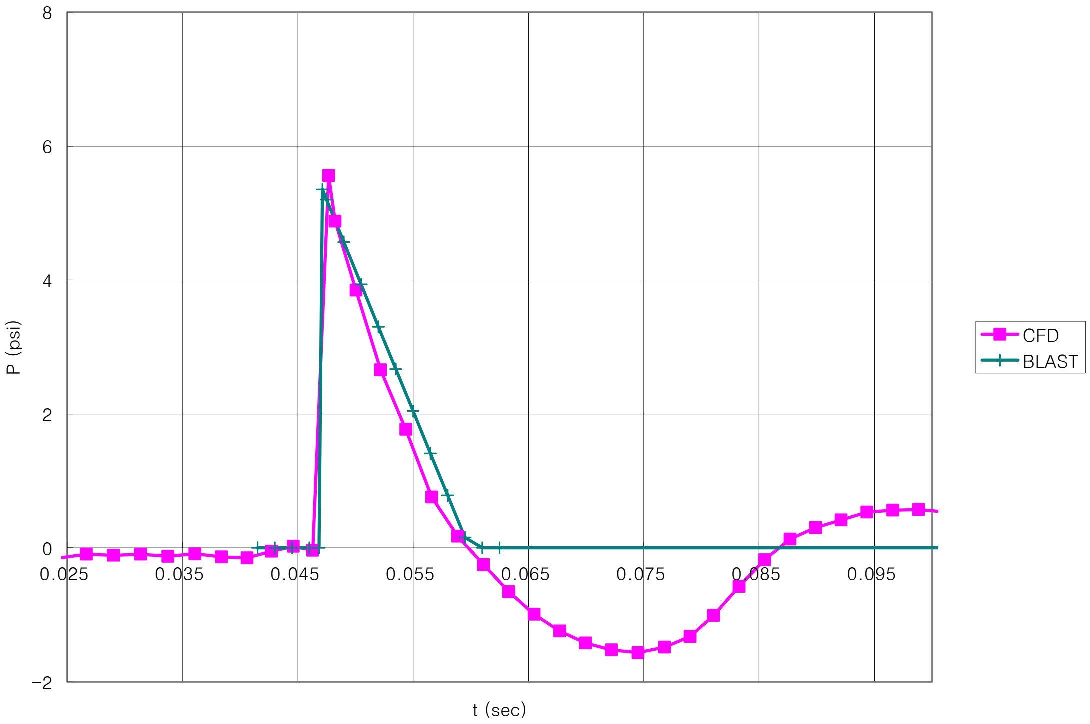
8
6
4
2
0
-2
P (psi)
0.025
0.035
0.045
0.055
0.065
0.075
0.085
0.095
t (sec)
CFD
BLAST

(b) side 2

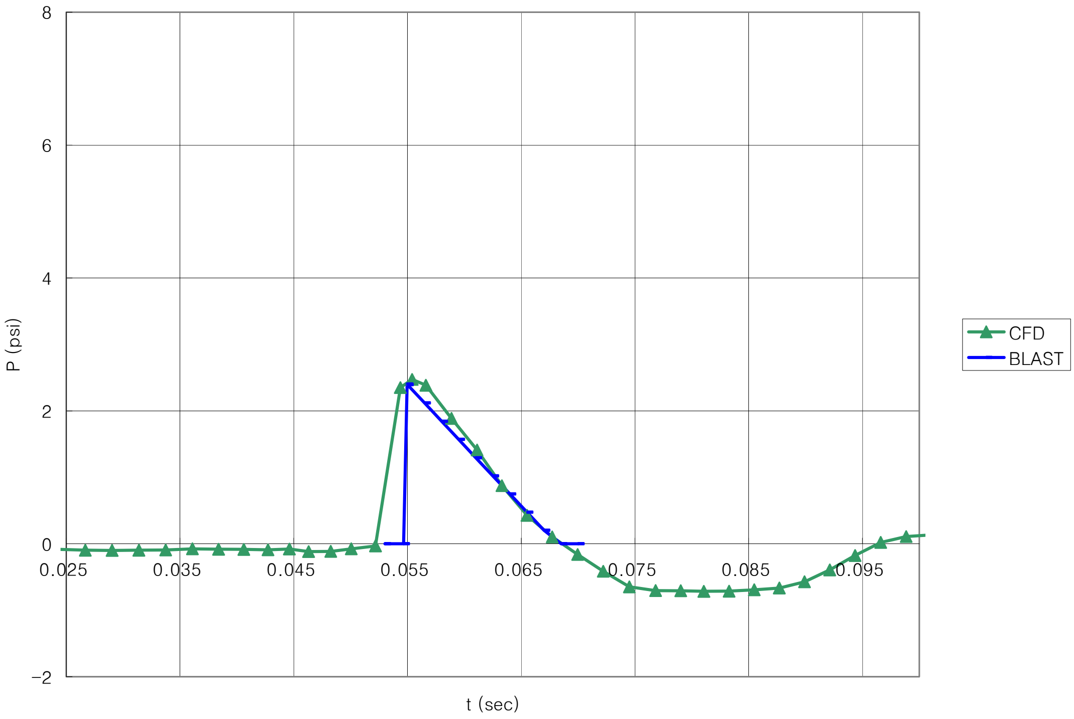
8
6
4
2
0
−2
P (psi)
0.025
0.035
0.045
0.055
0.065
0.075
0.085
0.095
t (sec)
CFD
BLAST

(c) side 3

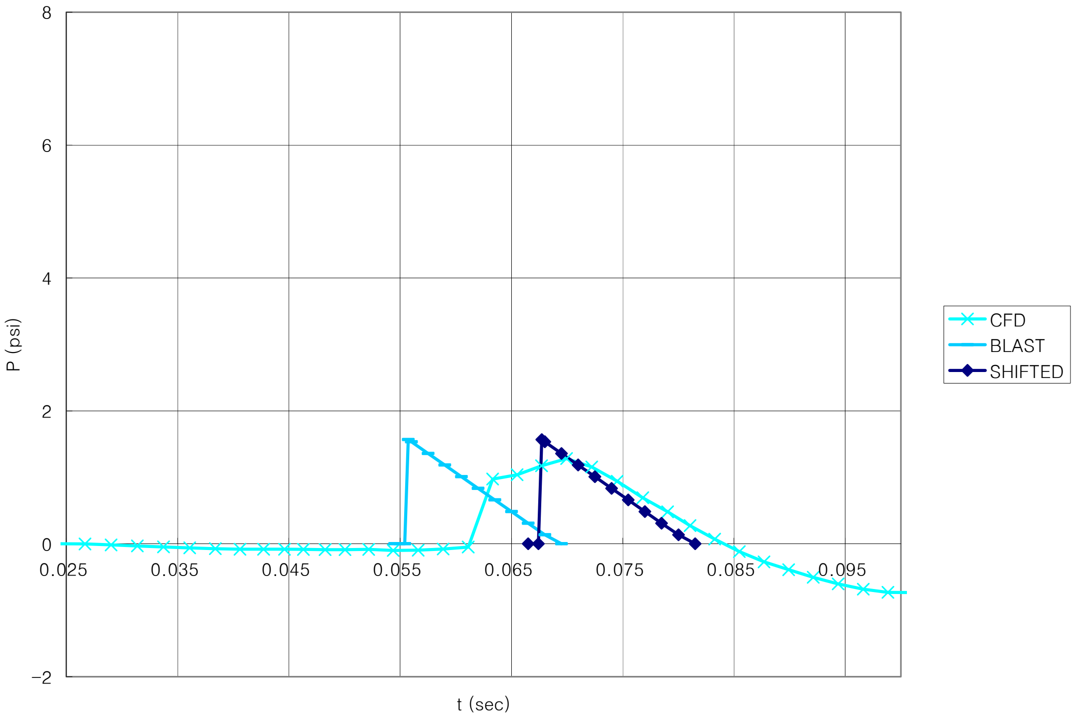

(d) side 4

Figure 3.7 Comparison of overpressure profiles; BLAST is a result estimated using the BLAST2.f program and CFD is a result obtained from the numerical simulation using Fluent

Chapter 4

Numerical Analysis of Flexible Structure

This chapter will describe the Finite Element Method (FEM) methods for flexible membrane structures and its dynamic response to blast loadings. For this purpose, the finite element models in ANSYS will be reviewed and a numerical test will be performed for the finite element model which can be used in the transient analysis. Then, an application of transient analysis to the tent structure under blast loading will be performed.

4.1 Introduction

When a rigid or flexible structure is placed under a dynamic loading condition such as an airblast, the response depends on the duration of the loading, the peak load, and the shape of the pressure pulse. The blast parameters and the blast loading over the rigid or flexible structure were already studied and explained in Chapter 2. In Chapter 3, numerical simulation of blast wave propagation over a rigid structure and the blast loading on a rigid structure were studied using the Computational Fluid Dynamics (CFD) code, Fluent. In this chapter, the finite element method is studied to obtain the large motion of a flexible structure under dynamic loading conditions. The Computtional Structural Dynamics (CSD) code, combined with the CFD code, is required to solve problems such as the transmitted blast wave, the blast wave propagation over a flexible structure, and the blast loading on a flexible structure, and this will be considered in Chapter 5 on the fluid-structure interaction. In this chapter, finite element models in

ANSYS are studied for their properties and the assumptions made in deriving the governing equation of motion for numerical analysis. Then these element models are used to calculate the deflections of a flexible tent structure under static loading conditions. Finally, a shell-type element, SHELL63 in ANSYS, is used to obtain the dynamic response of the flexible structure to the blast loading. In this FEM analysis, geometrci nonlinearities are considered using the geometrically nonlinear options within the ANSYS since the large deflection is expected for flexible membrane structures due to pressure loads normal to the surface.

4.2 Finite Element Method for Flexible Structure

4.2.1 Shell-Type Finite Element Models

Since the flexible structure is a very thin structure, it is usually modeled by shell-type elements in the FEM code. While the derivation of governing equations for a curved shell-type element poses many difficulties, the flat shell-type element replacing the curved shell-type element, by reducing the size and increasing the number of finite elements, can lead to a relatively simple derivation of alternative formulations with physical approximations due to limiting the shape of the finite elements to a flat plate.

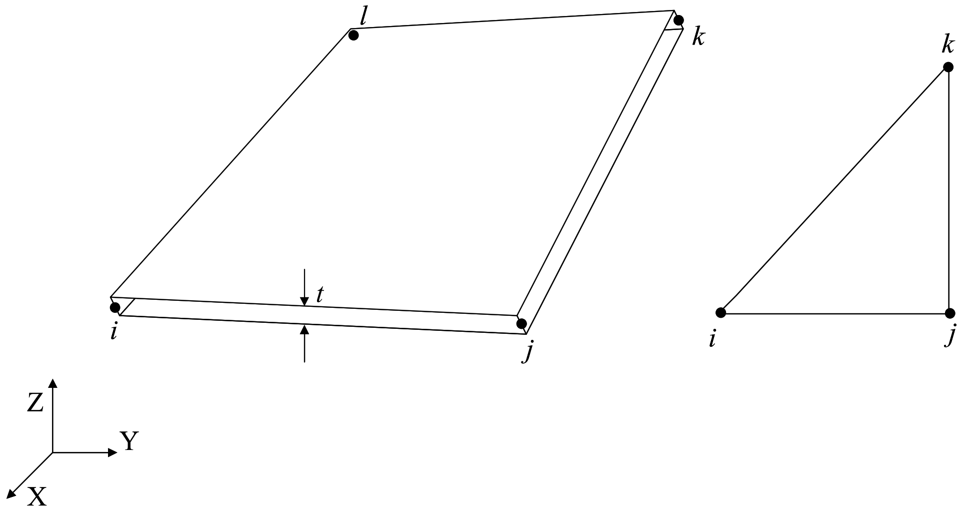

Figure 4.1 Geometric definition of a shell-type element

Therefore, a shell-type element model is basically a structure that can be derived from a flat plate by initially forming the middle surface as shown in Figure 4.1. However, the way a shell sustains external loads is very different from that of a general flat plate. The stress resultants acting at a node point of the shell have both tangential and normal components, each of which may carry a major part of the load. In Figure 4.2, in-plane deformations, u and v, are tangential to the shell middle surface and cause the elastic force resisting the deformation, and out-of-place deflection, w, is normal to the shell middle surface and causes the bending force resisting the bending deflection. Therefore, the analysis of the general deformation and deflection of shell-type elements is mathematically very complicated.

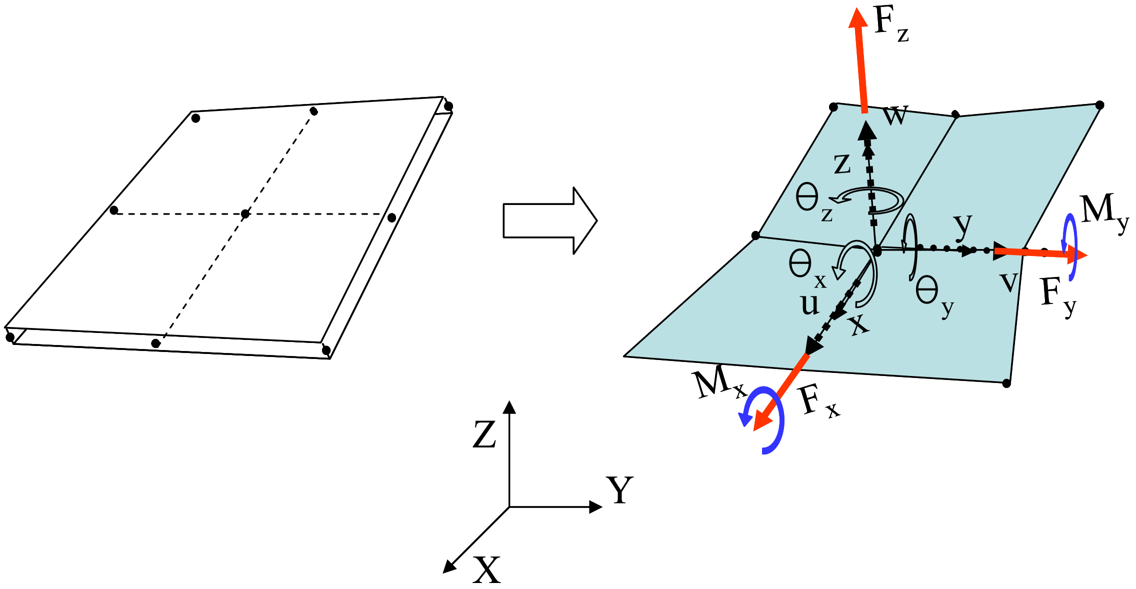

Figure 4.2 Deformation and acting forces at a node point in a flat shell element

Since the flat shell-type elements are used in the derivation of this complicated mathematical equation of large deflection of flexible structures, it is assumed that the behavior of a continuously curved surface could be adequately represented by the behavior of a surface made from the flat elements. With theoretical developments and the evidence from many numerical examples, this assumption is considered as acceptable, *i.e.,* flat plate elements with independent membrane and bending actions could properly represent the true behavior of curved shells, especially in situations where these actions are coupled together in the structural response. Not only is the formulation based on this assumption easy to code, but flat shell-type elements are more suitable for non-linear analysis since in that case the stiffness matrix has to be evaluated many times.

4.2.2 Flat Shell Element Configuration

A typical polygonal flat shell element involves in-plane and bending actions in its local coordinate system. For the in-plane action (plane stress), the strain can be described in terms of the displacements u and v at each node as shown in Figure 4.2. Through the application of the principle of virtual work to the equations of motion of the flat shell element[127], the stiffness matrix $[K]^P$ is derived and the nodal forces $\{F\}^P$ are related to the displacement parameters $\{u\}^P$ by as shown below:

$$\{F\}^P = [K]^P \{u\}^P \tag{4.1}$$

where

$$\{u\}^P = \begin{Bmatrix} u_i \\ v_i \end{Bmatrix}, \{F\}^P = \begin{Bmatrix} F_{xi} \\ F_{yi} \end{Bmatrix} \tag{4.2}$$

Similarly, for the bending action, the strain can be defined in terms of nodal displacement w (z-direction) and the relative deflection to the neighboring nodes which are shown in two rotational components θ_x and θ_y shown in Figure 4.2. Then, the stiffness matrix is defined as follows:

$$\{F\}^B = [K]^B \{u\}^B \tag{4.3}$$

where (see Figure 4.2)

$$\{u\}^B = \begin{Bmatrix} w_i \\ \theta_{xi} \\ \theta_{yi} \end{Bmatrix}, \ \{F\}^B = \begin{Bmatrix} F_{zi} \\ M_{xi} \\ M_{yi} \end{Bmatrix} \tag{4.4}$$

These derived equations (4.1) and (4.3) are based on two important assumptions. First, the deformations from both in-plance and bending actions are uncoupled with respect to each other. Second, the rotational component θ_z does not occur as a nodal deformation parameter. While assembling equations (4.1) and (4.3), however, this rotation is taken into account as a fictitious couple θ_z.

Combining the nodal displacements, one obtains

$$\{u\} = \begin{Bmatrix} u_i \\ v_i \\ w_i \\ \theta_{xi} \\ \theta_{yi} \\ \theta_{zi} \end{Bmatrix} \tag{4.5}$$

and

$$\{F\} = \begin{Bmatrix} F_{xi} \\ F_{yi} \\ F_{zi} \\ M_{xi} \\ M_{yi} \end{Bmatrix} \tag{4.6}$$

The complete form can be written as

$$\{F\} = [K]\{u\} \tag{4.7}$$

The above formulation is valid for any shape of the polygonal element, such as for rectangular and triangular elements as shown in Figure 4.1. The assembled stiffness matrices [K] are obtained with reference to a local coordinate system. The rotational component θ_z is accounted for in the assembled stiffness matrices by adding an appropriate number of zeros. This stiffness matrices [K], which shows the material linearity, becomes a function of the displacement {u} when the geometric nonlinearities are considered, since the stiffness changes because the shape changes and/or the rotation.

These are transformed into the global system in order to be assembled into the appropriate global equilibrium equations. The transformation matrix is composed of cosines of angles between the particular axes in the local coordinate system and the global co-ordinate system. Once the stiffness matrices of all the elements are determined in the global coordinate system, the assembly of the elements and forces follows the same pattern. The displacements obtained are referred to the global system, but before the stresses are computed, it is necessary to change these to the local coordinate system for each element.

In this formulation, a problem arises if all the elements meeting at a node are co-planar[127]. This situation occurs for folded plate segments and at the straight boundaries of developable surfaces (*e.g.*, cylinders or cones), due to the zero stiffness in the θ_z direction and from the fact that the classical shell equations do not produce equations associated with the rotational parameters. Inclusion of rotation in the z-direction and the associated force M_z has its benefit in that the rotations and displacements at nodes can be treated in a simple manner using the transformations[127].

One way to eliminate this problem is by adding an arbitrary stiffness coefficient $K_{\theta z}$ (z–direction) for the rotational part. *i.e.*, an arbitrary in-plane rotational stiffness. Thus the equation in the local coordinate system becomes[127]

$$K_{\theta z} \times \theta_{zi} = 0 \tag{4.8}$$

This would lead to a perfectly well-behaved set of equations from which all the displacements can be obtained. Since it does not affect the stresses and is uncoupled from all the equilibrium equations, the stiffness for the rotational part is added externally without affecting the results. But this approach causes programming complexities, and therefore modifications are required so that the rotational parameters arise more naturally and have real physical meaning. The θ_z introduced in this way is called a drilling degree of freedom[127]. For triangular elements with corner nodes only, the membrane form utilizes the linear displacement field that yields only constant-strain terms, while most of the bending elements have bending strains with higher-order terms.

4.2.3 Study of Shell-Type Finite Element Models in ANSYS

There are several shell-type finite element models in ANSYS for use in simulating the motion of flexible structures: SHELL28, SHELL41, SHELL43, SHELL63, SHELL93, SHELL143, SHELL150, and SHELL181. The characteristics of these elements were reviewed through the ANSYS manual[134] and three of them, which can model the large non-linear deflections of membrane structure, were selected: SHELL41, SHELL63, and SHELL181.

SHELL41 is a 3-D element having membrane (in-plane) stiffness but no bending (out-of-plane) stiffness. It is intended for shell structures where bending of the elements is of secondary importance. The element has three degrees of freedom at each node: translations in the nodal x, y, and z directions. The element has variable thickness, stress stiffening, large deflections, and a cloth option. When out-of-plane loads are applied to this shell element as in the case of blast loading, any out-of-planeness within the element or roundoff error in nodal locations may cause instability in the displacement solution. To counteract this, the element has the option of adding a slight normal stiffness with an elastic foundation stiffness (EFS) which is defined as the pressure required to produce a unit normal deflection of the foundation.

The formulation of the SHELL63 (flat shell) consists of a membrane element, the plane-stress element of the constant stress-strain triangular element (CST), and a plate bending element without shear deformation based on the Discrete-Kirchhoff Theory (DKT). Therefore, it has both bending and membrane capabilities in addition to membrane only capability, allowing both in-plane and normal loads, and has six degrees of freedom at each node: translations in the nodal x, y, and z directions, and rotations about the nodal x, y, and z axes. (If the membrane option is used, the element has translational degrees of freedom only.) A consistent tangent stiffness matrix option is available for use in large deflection (finite rotation) analyses and it has the option for choosing the type of in-plane rotational stiffness. The use of a consistent tangent stiffness in a non-linear analysis often speeds up the rate of convergence rapidly. It normally results in a quadratic rate of convergence. This consistent tangent stiffness matrix is derived from the discretized finite element equilibrium equations without the introduction of various approximations. A consistent tangent stiffness accounting for finite rotations derived by Nour-Omid and Rankin[133] for beam/shell elements is used. The terminology of finite rotation in the context of geometrical non-linearity implies that rotations can be arbitrarily large and can be updated accurately. Using the Allman rotational stiffness for the in-plane rotational stiffness enhances the convergence behavior in large deflection (finite rotation) analyses of planar shell structures (flat shells or flat regions of shells) as explained in Section 4.2.2.

SHELL181 is suitable for analyzing thin to moderately-thick shell structures. It is a 4-node element with six degrees of freedom at each node: translations in the x, y, and z directions, and rotations about the x, y, and z-axes. (If the membrane option is used, the element has translational degrees of freedom only, like SHELL63.) The degenerate triangular option should only be used for filler elements in mesh generation. SHELL181 is also well-suited for linear, large rotation, and/or large strain non-linear applications. Change in shell thickness is accounted for in non-linear analyses. In the element domain, both full and reduced integration schemes are supported. SHELL181 accounts for follower (load stiffness) effects of distributed pressures.

Since the nodes of a shell-type element defined on a surface with three nodes or four nodes and straight edges do not give volume information, the thickness is given as an input. With these elements, material and geometric non-linearities can be modeled with stress stiffening and large deflection capabilities. Details regarding the shell-type elements used in the present work are explained in Ref. [134].

These three shell-type elements were applied to solve the deflection of a flexible structure under a static pressure load as shown in Figure 4.3. The static pressure load is 150 Pa which is the initially maintained pressure inside the TEMPER tent to prevent flow of contaminated air into the liner for the CPS operation as explained in Section 1.1.

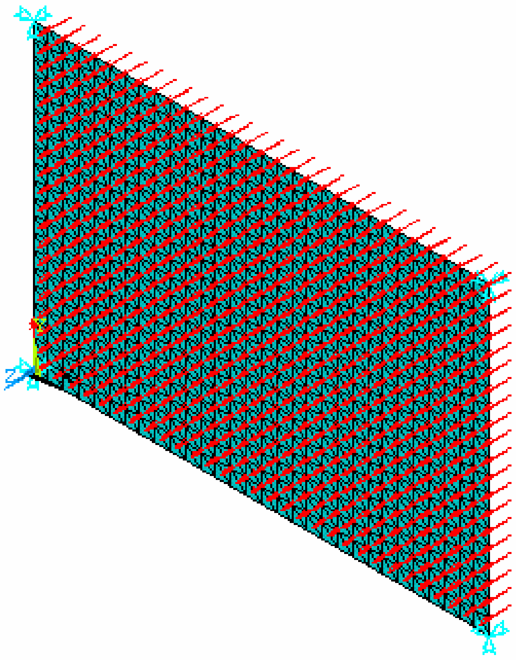

Figure 4.3 Geometric and loading boundary conditions for a membrane structure represented by SHELL41, SHELL63, and SHELL181 in ANSYS

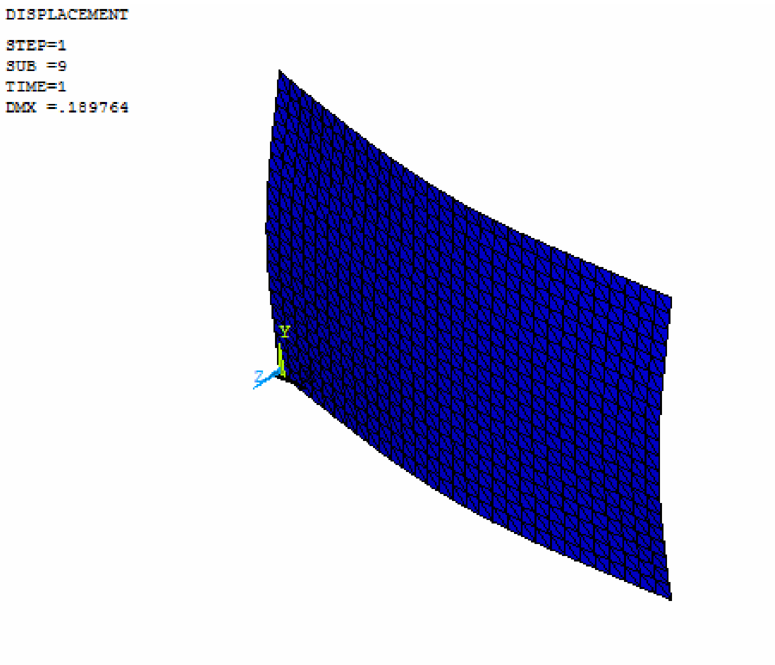

Figure 4.4 Deformed shape of flexible structure modeled with SHELL41 in ANSYS

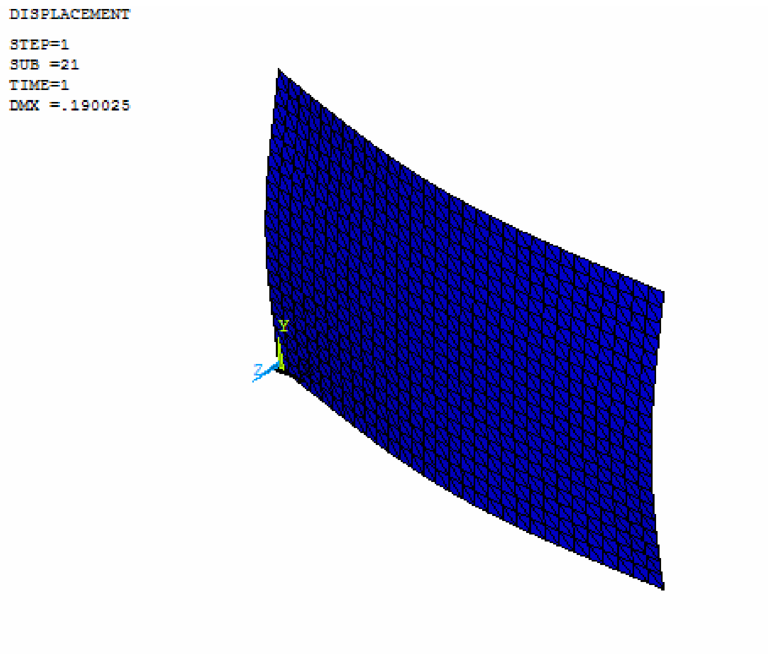

Figure 4.5 Deformed shape of flexible structure modeled with SHELL63 in ANSYS

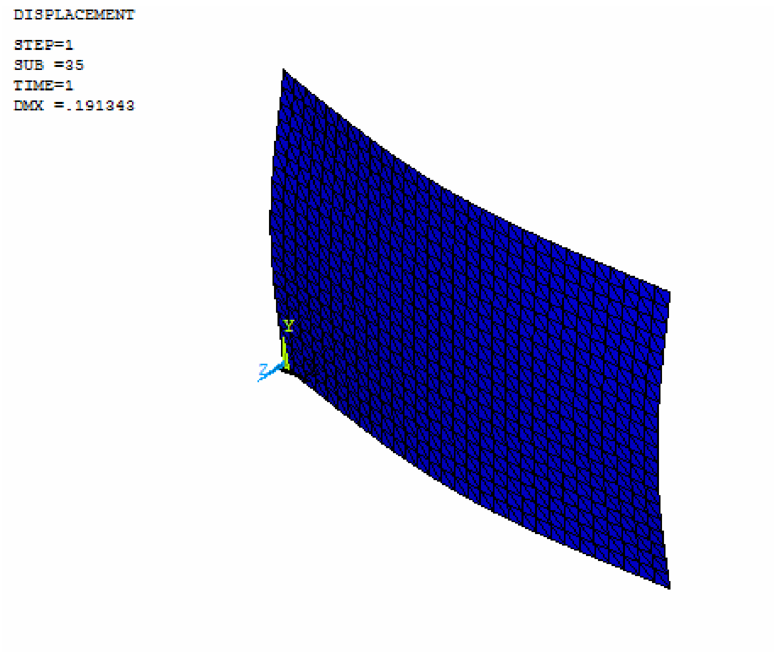

Figure 4.6 Deformed shape of flexible structure modeled with SHELL181 in ANSYS

The material properties for the flexible structure are: 0.076 mm for thickness, 1400 kg/m^3 for density, 3.89 GPa for Young's modulus, and 0.38 for Poisson's ratio. These values are primarily based on the experimental results explained in Ref. [136].

Table 4-1 Magnitude of maximum deflection vs. shell-type finite element models

	SHELL41	SHELL63	SHELL181
Maximum deflection (m)	0.1897	0.1900	0.1913

From Figure 4.4 to Figure 4.6, it is shown that the deflection shape and the magnitude of maximum deflection (see Table 4-1) are almost same, even though different element types were used to model the flexible structure under the static loading. Based on these results from static analyses, any of the three element types can be used to solve for the dynamic response of the flexible structure under the blast loading. Therefore, based on this result and the fact that SHELL63 has both bending and membrane capabilities in addition to membrane only capability, shell-type finite element models were studied focusing on SHELL63 for the transient dynamic analysis.

4.3 Dynamic Response of Flexible Structure

Transient analysis of dynamic responses of flexible structures is challenging due partly to the interaction between membrane and bending deformations. For non-linear problems, analytical results of the governing equations cannot be obtained, so the solutions are determined using numerical methods. The physical behavior of a shell is basically governed by the constitutive law, geometry, boundary conditions, and loading, and can usually be categorized as membrane dominated, bending dominated, or mixed[126]. When large deformations are included, a state of pure bending is seldom encountered, as membrane stresses are generated due to the large transverse displacements. Due to these large deformations, the characteristic of the problem changes from bending dominated to membrane dominated. An important aspect of the structural analysis of membrane structures, regardless of the thickness, is that significant bending develops near restraints or in the vicinity of point loads. The presence of bending moments results in numerical problems if appropriate care is not taken in numerical simulation.

4.3.1 Implicit Structural Transient Analysis

Structural transient analysis determines the dynamic response of a structure corresponding to the action of any general time-dependent loads. This type of analysis can be used to obtain the time-varying displacements, strains, stresses, and reaction forces in a structure as it responds to any combination of static, transient, and harmonic loads.

The time scale of the loading is such that the inertia or damping effects are considered to be essential in solving for the dynamic response. Initial conditions are assumed to be known. If the inertia and damping effects are negligible in analyzing the characteristics of the response, it may be possible to use a static analysis instead.

The basic equation of motion for the transient dynamic analysis[134] is

$$[M]\{\ddot{u}\}+[C]\{\dot{u}\}+[K]\{u\}=\{F(t)\} \tag{4.9}$$

where [*M*] is a mass matrix, [*C*] is a damping matrix, [*K*] is a stiffness matrix, $\{u\}$ is a nodal displacement vector, and {F(*t*)} is an applied load vector. The dot above the nodal displacement *u* means a derivative with respect to time, indicating that $\dot{u}$ means the nodal velocity and $\ddot{u}$ means the nodal acceleration. At any given time, *t*, these equations can be thought of as a set of "static" equilibrium equations that also take into account inertia forces ($[M]\{\ddot{u}\}$) and damping forces ($[C]\{\dot{u}\}$). Then, when the geometric nonlinearities are considered, Equation (4.9) is changed into a nonlinear equation of motion for the transient dynamic analysis as shown below.

$$[M]\{\ddot{u}\}+[C]\{\dot{u}\}+\left\{f_{NL}^{S}(\{u\})\right\}=\{F(t)\} \tag{4.10}$$

There are various methods to solve Equation (4.9) and (4.10), and those methods are usually classified into two groups: (i) explicit and (ii) implicit. The forward difference method[127] is a well-known example of explicit transient analysis, and the Newmark method and the HHT method[127,135] are examples of the implicit transient analysis. In the present work, the Newmark method in ANSYS is used to perform implicit transient analysis for the deflection of flexible structures. The details of these transient dynamic analyses for structures are found in Refs. [127] and [134]. The time increment between successive time steps is called the integration time step.

For the non-linear structural resistance vector, $\{f_{NL}^{S}(\{u\})\}$, the Newton-Raphson method is employed along with the Newmark method. If follower force effects are taken into account or the load vector is influenced by the dynamic response, the load vector becomes a function of *u* and the interaction between the structural motion and the loading should be taken into account to solve Equation (4.9).

4.3.2 Solution Methods

ANSYS provides three methods for performing implicit transient dynamic analysis for structures: the full method, the mode superposition method, and the reduced method.

The full method uses the full system matrices to calculate the transient response. It is the most general of all the methods: (i) it allows all types of non-linearities (large deflections, large strains, and so on), (ii) no mass matrix approximation is involved allowing effective use of solid-model loads, and (iii) it accepts all type of loads including nodal forces, imposed displacements, and element loads (pressure). Therefore it is easy to use, because mode shapes and selection of master degrees of freedom, which are critical in the mode superposition method and the reduced method separately, do not need to be pre-determined for solving the equation of motion. However, these advantages cause more expensive computation than the other two methods.

The mode superposition method uses factored mode shapes (eigenvectors) from a modal analysis to calculate the structure's response. It is faster and less expensive than the reduced or the full method for many problems and it accepts modal damping. But limited non-linear solutions are allowed and imposed displacements are not accepted for the loading condition.

The reduced method condenses the problem size by using master degrees of freedom (DOF) and reduced matrices. After the displacements at the master DOFs have been calculated, ANSYS expands the solution to the original full DOF set. This method is faster and less expensive than the full method. But this method also has limited non-linear solutions and limited imposed loading conditions.

Therefore, considering the non-linearity in the expected large deflection in the dynamic response of the felxible structure to blast loading (time-varying pressure distribution), the full method is used for the transient dynamic analysis of the flexible structures.

4.3.3 Application

The case treated in this transient dynamic analysis is the same as that solved in the calculation of blast loading using BLAST2.f in Section 2.6; the TEMPER tent (Figure 1.1) is subjected to an external explosion of 25 kg (55.1 lb) TNT, 65 ft away from the explosion origin as shown in Figure 2.10. The pressure loads (the overpressure profiles, see Figure 4.7) applied to each membrane-type structure are obtained using BLAST2.f which takes into account the FSI effect on the side of a moving wall which faces the incoming blast wave (refer to Sections 2.3 and 2.6). In addition, the fluid-structure interaction effects on the opposite side of the wall are included by reducing the pressure loads obtained on the moving wall using BLAST2.f. Reduction of the pressure loads refers to the subtraction of the pressure loads on the opposite side of the wall (the resisting pressure loads) from the pressure loads on the side facing the blast wave (the blast pressure loads). Since the external blast loads over the closed flexible shelter cause dynamic movement of the flexible walls internal resisting pressure loads are developed inside the tent. This FSI effect will be treated separately in Chapter 5 in detail. It is assumed that the pressure loads on each membrane-type section of the structure are uniform in the present transient dynamic analysis. Since the pressure load on side 1 is the strongest, the transient dynamic analysis was performed with the side 1 pressure load in Figure 4.7.

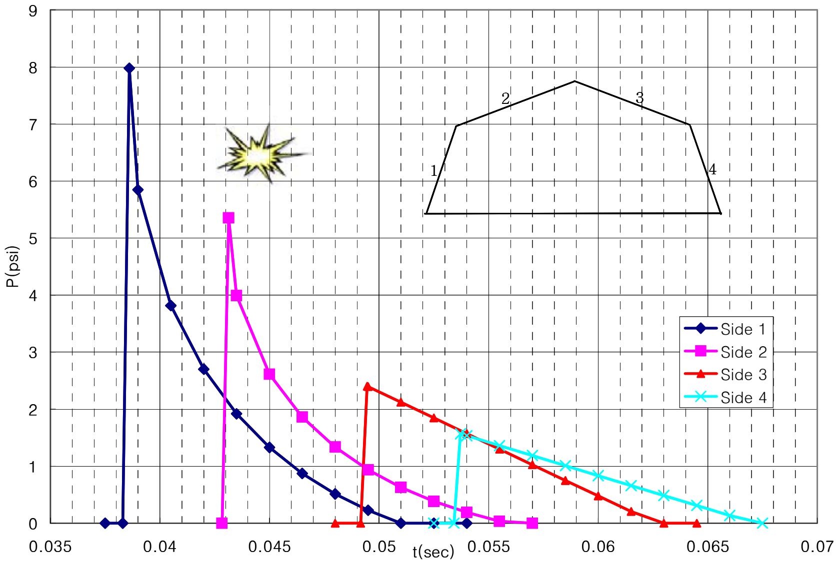

Figure 4.7 Estimated airblast loading over a TEMPER tent

Figure 4.8 shows the displacement restrictions along the edges and pressure loads imposed on all the elements of the surface in the transient dynamic analysis for the flexible membrane-type structure. The full solution method with the Newton-Raphson method and the Newmark method is employed for the non-linear transient analysis at each time step with the corresponding loading conditions. The material properties for the membrane structure are: 3 mm for thickness, 3000 kg/m^3 for density, 250 MPa for Young's modulus, and 0.33 for Poisson's ratio. These values are primarily based on the experimental results explained in Ref. [139]. However, some values are changed with a consideration of the mixed structural properties of both canvas and liner material acting together, and numerical stability required for the transient dynamic analysis. Figure 4.9 and Figure 4.10 show the results of the transient dynamic analysis using the SHELL63 finite element for modeling the tent structure under the blast loading. These results are required to be compared with the results of other analyses, which are performed separately in the group research and will be cited.

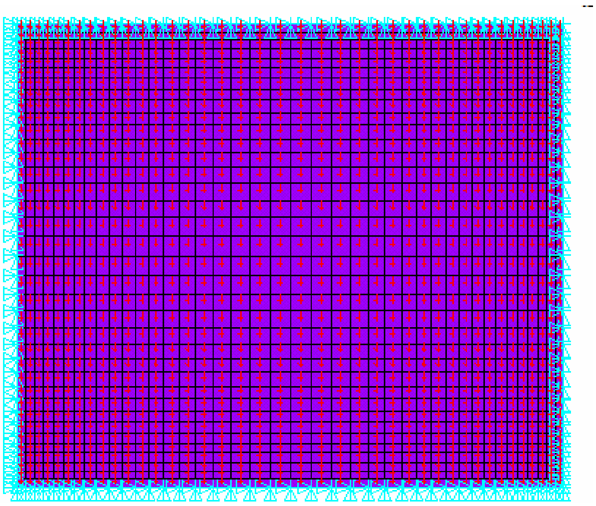

Figure 4.8 Geometric and loading boundary conditions for each membrane

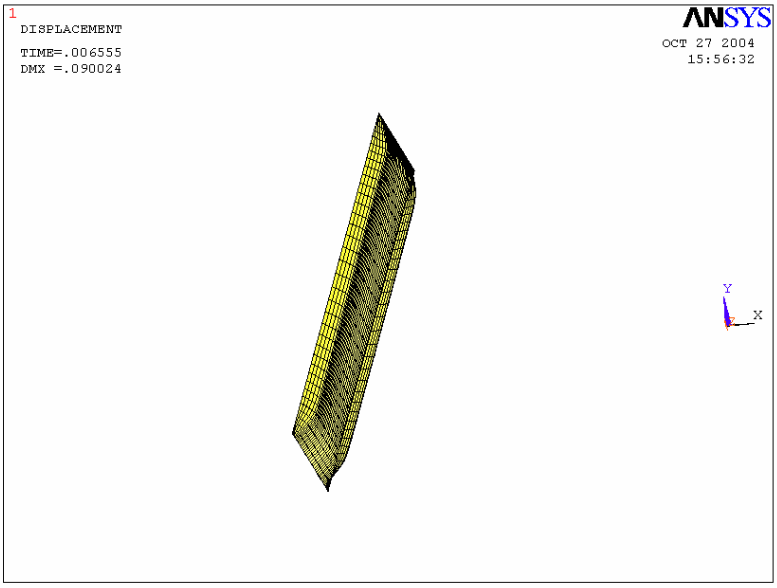

(a) t = 0.0065 sec

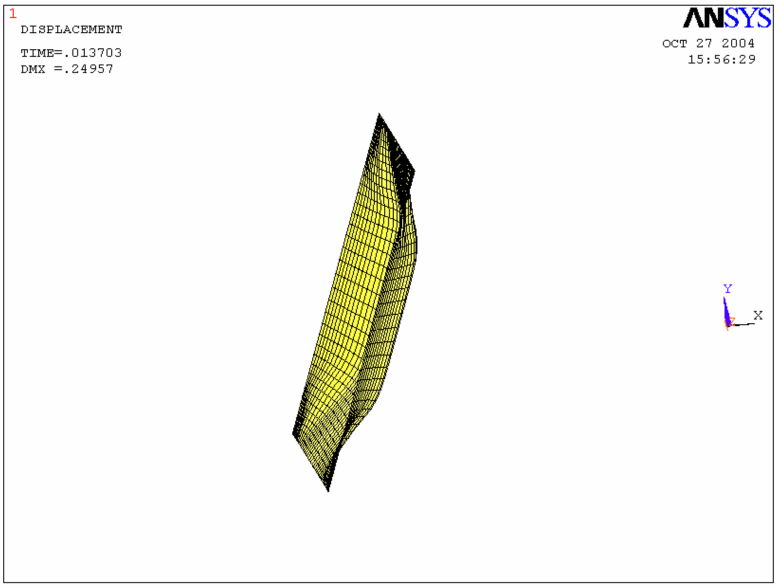

(b) t = 0.0137 sec

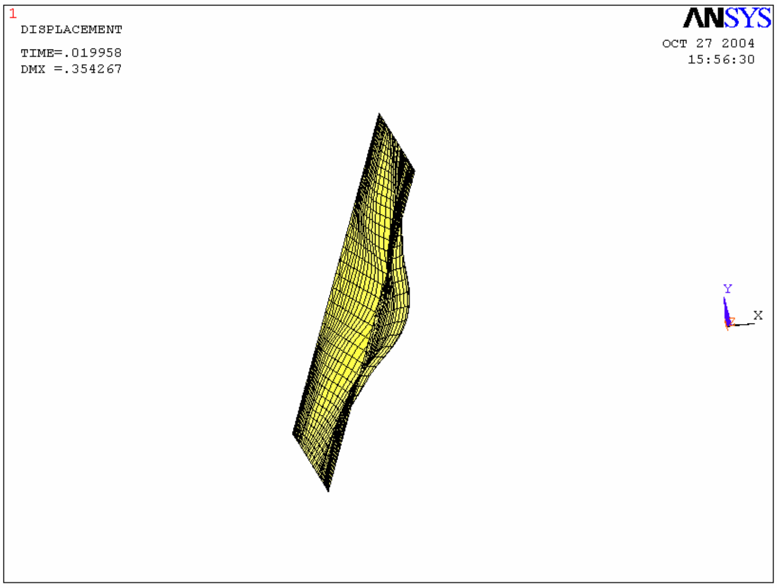

(c) t = 0.01996 sec

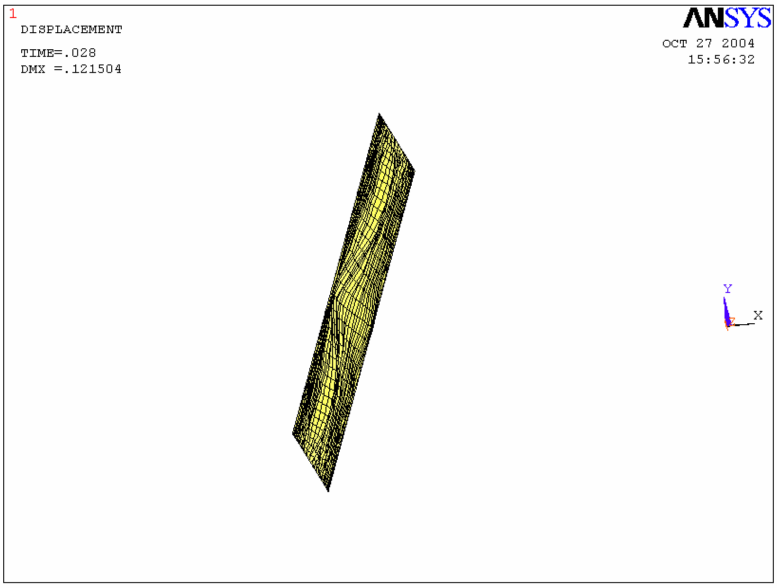

(d) t = 0.0280 sec

Figure 4.9 Deformed shapes at certain times

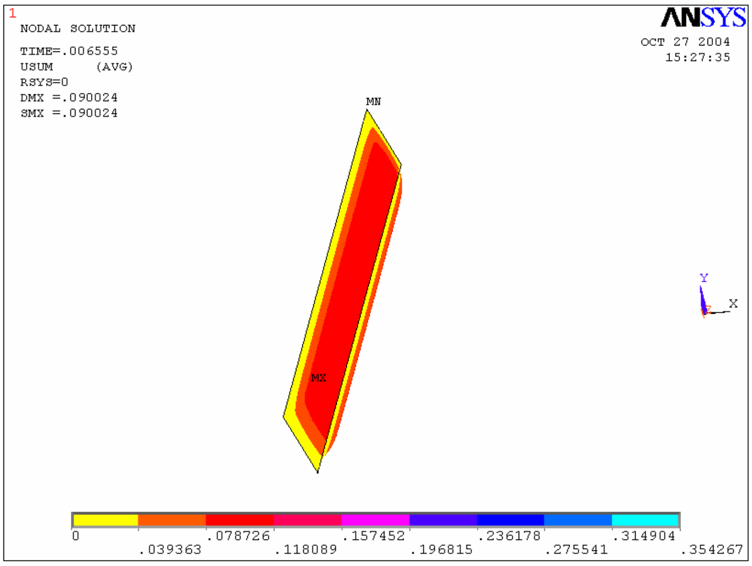

(a) t = 0.0065 sec

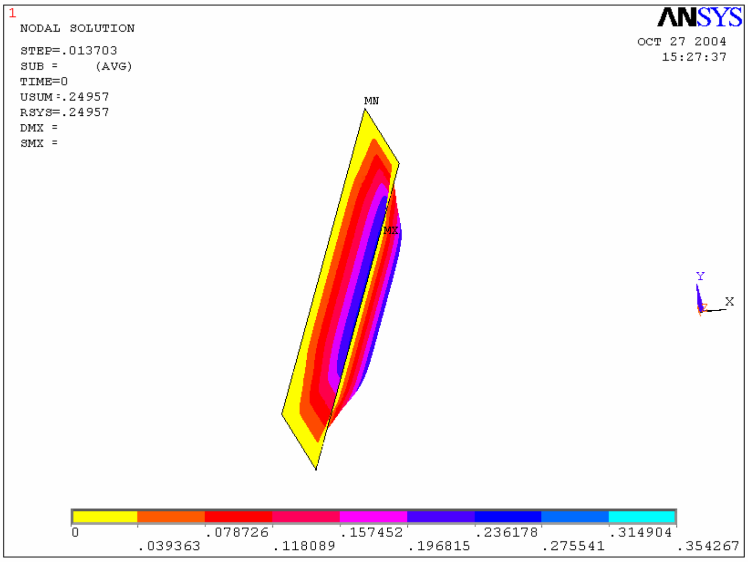

(b) t = 0.00137 sec

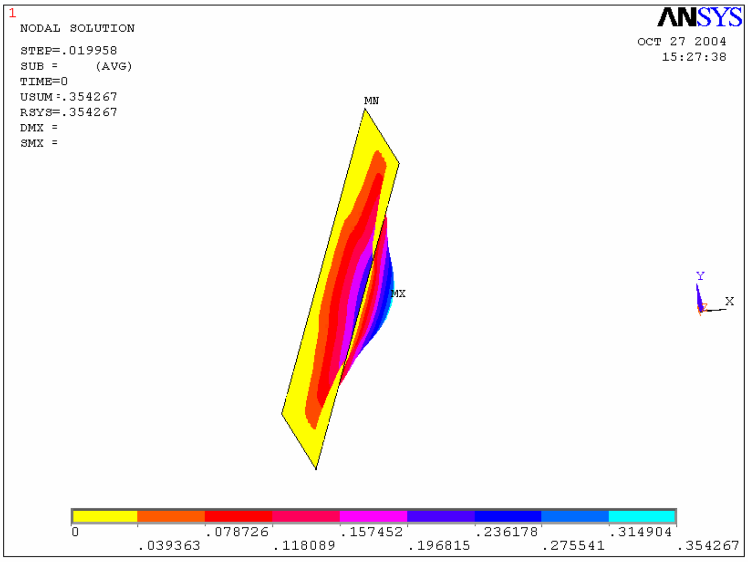

(c) t = 0.01996 sec

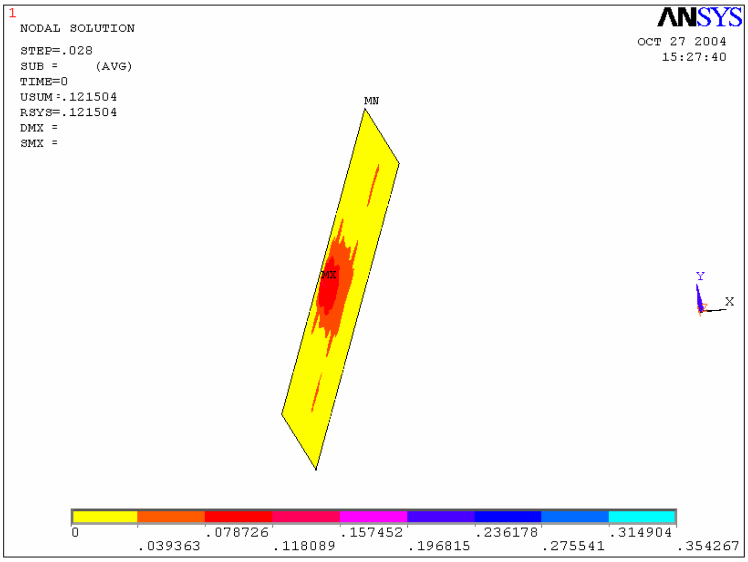

(d) t = 0.0280 sec

Figure 4.10 Contours of the average magnitude of the deflection at certain times

Chapter 5

Fluid Structure Interaction

This chapter will explain the iterative Fluid Structure Interaction (FSI) algorithm and the algorithm will be applied to the FSI analysis for the transmitted blast wave and the blast loading inside the flexible tent as shown in Figure **1.4**. Then the results from the FSI analysis will be compared with both experimental and estimated data. Finally, the numerical simulation of blast wave propagation covered in Chapter 3 will be extended to the flexible structure by involving the results of the FSI analysis as shown in Figure **1.5**, and the blast loading of overpressure profiles on a flexible structure obtained from the numerical simulation will be compared with both empirical/analytical results and experimental data.

5.1 Introduction

The blast parameters and the blast loading over the rigid or flexible structure were already studied and explained in Chapter 2. In Chapter 3, numerical simulation of blast wave propagation over a rigid structure and the blast loading on a rigid structure were studied using a Computational Fluid Dynamics (CFD) code. In Chapter 4, the Finite Element Method (FEM) was used to obtain the large motions of a flexible structure under a dynamic loading condition. In this chapter, the Computational Structural Dynamics (CSD) code, combined with the CFD code, will solve the problems such as the transmitted blast wave, blast wave propagation over a flexible structure, and blast loading on a flexible structure.

Structural movement of a TEMPER tent due to the external airblast loading causes air inside the tent to move and generates transmitted blast wave loading inside the structure. This is an example of fluid-structure interaction[13]. As shown in Figure 5.1, due to the dynamic response of the flexible structure to the external blast loading over side 1, an external blast wave is transmitted inside the closed flexible structure. The pressure loads generated by this transmitted blast wave on side 4 may be one of the important causes for the material failure of the XM28 liner inside the TEMPER tent.

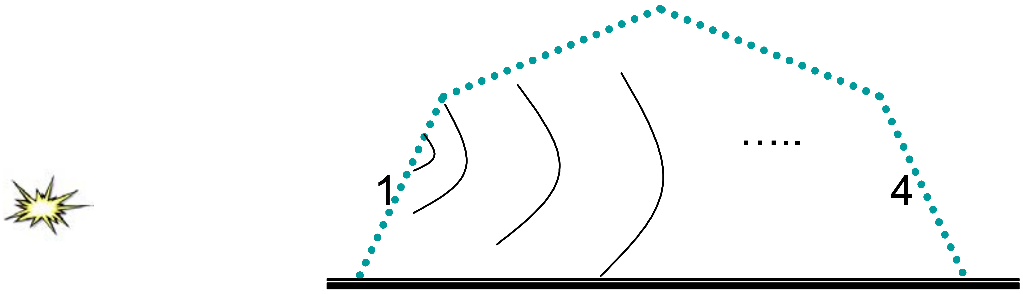

Figure 5.1 Transmission of external blast wave inside a flexible tent structure

Structural movement of a TEMPER tent due to the external airblast loading combined with the air resistance inside the tent also influences the pressure loads which were calculated through the numerical simulation of blast wave propagation over a rigid structure using a CFD code in Chapter 3. This is also an example of fluid-structure interaction. In this chapter, numerical simulation of blast wave propagation is extended to a flexible structure through the FSI analyses mentioned above, and then the pressure loads on a flexible structure will be calculated and compared to the experimental data.

5.1.1 Transmitted Blast Wave Loading

The transmitted blast wave loading inside a tent structure due to the dynamic response of the flexible structure to external blast loading is estimated using two different methods in the present study: (i) analytical/empirical models with a reduction factor, and (ii) the FSI analysis[12-13].

For the analytical/empirical model method, the reduction factor, which models the reduced strength of the blast wave transmitted through the wall, was determined through examination of the collected field test data. Then, BLAST2.f was used directly to compute the transmitted wave pressure loading, reducing the predicted peak overpressure with the reduction factor.

For the present FSI analysis, the algorithm which was previously applied to an aeroelastic problem by Bendiksen[14] was implemented. In this method, a type of fully explicit partitioned[13] or staggered[15] algorithm, CFD, and CSD based on FEM were performed iteratively at each intermediate time step to generate the transient boundary conditions during the interaction between the structure and the flow field. Boundary conditions, the pressure loading for CSD, and the movement of the boundary defining the flow field for CFD are the direct means by which the domains of fluid and structure influence each other. After the exterior blast loading over the structure was estimated using BLAST2.f, CSD was performed for the transient dynamic analysis of the response of the structure to the external pressure loading to determine the deformation at the initial time step. This deformation was used as the boundary condition for solving the internal flow field inside the structure using CFD to calculate the interior pressure loading due to the movement of the internal flow field. Finally, the resultant pressure loading was calculated from the external pressure loading determined in advance and the internal pressure loading. This resultant pressure loading was then used as the boundary condition in CSD for the next time step. This staggered iteration was repeated until the transmitted wave pressure loading was obtained on the chosen wall.

For the CFD solution, the same numerical methods used for the external flow field in Chapter 3 were implemented for the internal flow field solution. For the transient dynamic analysis of a 2-D tent structure in the CSD calculation, the tent structure was modeled with quadratic shell-type elements for the fabric and fixed geometric conditions for the frame in 3-D. The simplified structure of the flexible membrane structure was divided into four parts, because the CSD analysis was performed with the assumption of fixed frames, and each part surrounded by these frames is not influenced by the motion of the other parts. Then, the transient motion of the structure at the center section of the 3-D structure in the Z-direction was taken as the moving boundary in the CFD analysis in the iterative FSI routine. The rest of the numerical methods used for the motion of the tent structures are the same as explained for dynamic response of flexible membrane structures to blast loading in Chapter 4.

The estimations of the transmitted wave pressure loading from the two methods were compared with the field test data. This comparison showed that the two methods are capable of estimating the transmitted wave pressure loading, and that the FSI analysis using a staggered algorithm can be a useful tool to understand the unsteady motion inside a flexible structure reacting to an external explosive blast.

5.1.2 Blast Wave Propagation over a Flexible Structure

To solve the blast wave propagation over a flexible structure and its blast loading on a flexible structure, the CFD application done in Chapter 3 should be combined with the non-linear transient dynamic analysis and the transmitted blast wave loading analysis using the FSI analysis as mentioned in Section 5.1.1. The whole methodology for this FSI problem will be explained with Scherbatiuk's simplified numerical method[137] in Section 5.2.1. However, in the present research, instead of solving the FSI problems in two different flow fields separated by the flexible structure at the same time, the CFD application done in Chapter 3 will be combined with the deflection of the flexible structure obtained in the transmitted blast loading analysis in which the imposed pressure loads were calculated using BLAST2.f, which takes into account the FSI effect on the side of a moving wall which faces the incoming blast wave (refer to Sections 2.3 and 2.6). The synchronization problem involving two analyses based on different time domains was solved by matching the start of the deflection of the flexible structure obtained in the transmitted blast loading analysis with the time when the peak overpressure in the numerical simulation of the blast wave propagation over a rigid body arrives at the center of the surface.

The estimated pressure loads through the FSI analysis explained above were compared with the field test data. This comparison showed that the proposed FSI analysis can include the flexibility effect on the pressure loads calculated by the CFD code as explained in Chapter 3.

5.2 Transmitted Blast Wave Loading

5.2.1 Methodology

A general methodology for the fluid-structure interaction was introduced through a literature review in Section 1.2.4. Here, a methodology related to the transmitted blast wave is explained with Scherbatiuk's simplified numerical method[137] and the staggered algorithm using both FEM and CFD codes.

As shown in Figure 5.2 (a), the flexible membrane barrier is hit by a blast wave and deformed in a very short time, transmitting the blast wave through it. Therefore, it is possible that the strength of the transmitted blast wave depends on the motion of the barrier, *i.e.,* the same phenomenon which must be considered in the fluid-structure interaction studied in the present research. Scherbatiuk[137] studied the effects of different elastic material properties and geometries on transmission of blast waves through flexible barriers in a two-dimensional domain using a simple computational method. He solved numerically the equations of the motion of the flexible structure and combined the Meyer's method[138] for the FSI effect to calculate the resistance to movement provided by the increase of pressures on the opposing side of the flexible membrane, which is induced from the deforming velocity of the barrier. The resistance finally leads to the strength of the transmitted blast wave through a rigid movable wall and a model of a flexural membrane barrier.

As shown in Figure 5.2 (b) and Figure 5.3, the flexible membrane barrier is modeled with discrete lumped masses connected together by springs housed in massless, rigid, non-resisting extensible tubes simulating membrane resistance. In addition, rotational springs are located at the center of masses to resist bending. This discrete modeling leads to system of equations of motion in a matrix form, involving the blast forces as functions of time and the motion of the barrier.

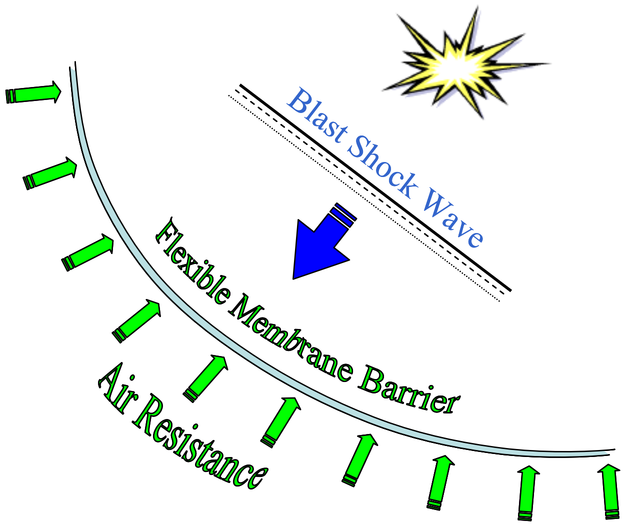

(a) Real Structure under Blast Loading

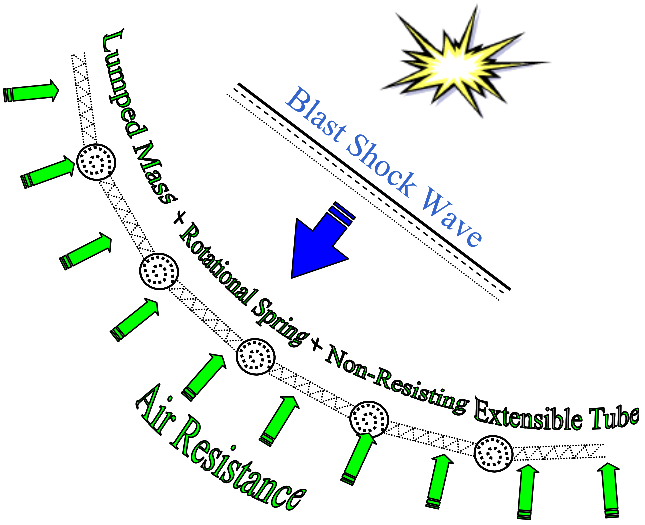

(b) Modeled Structure under Blast Loading

Figure 5.2 A flexible membrane and the blast wave transmission

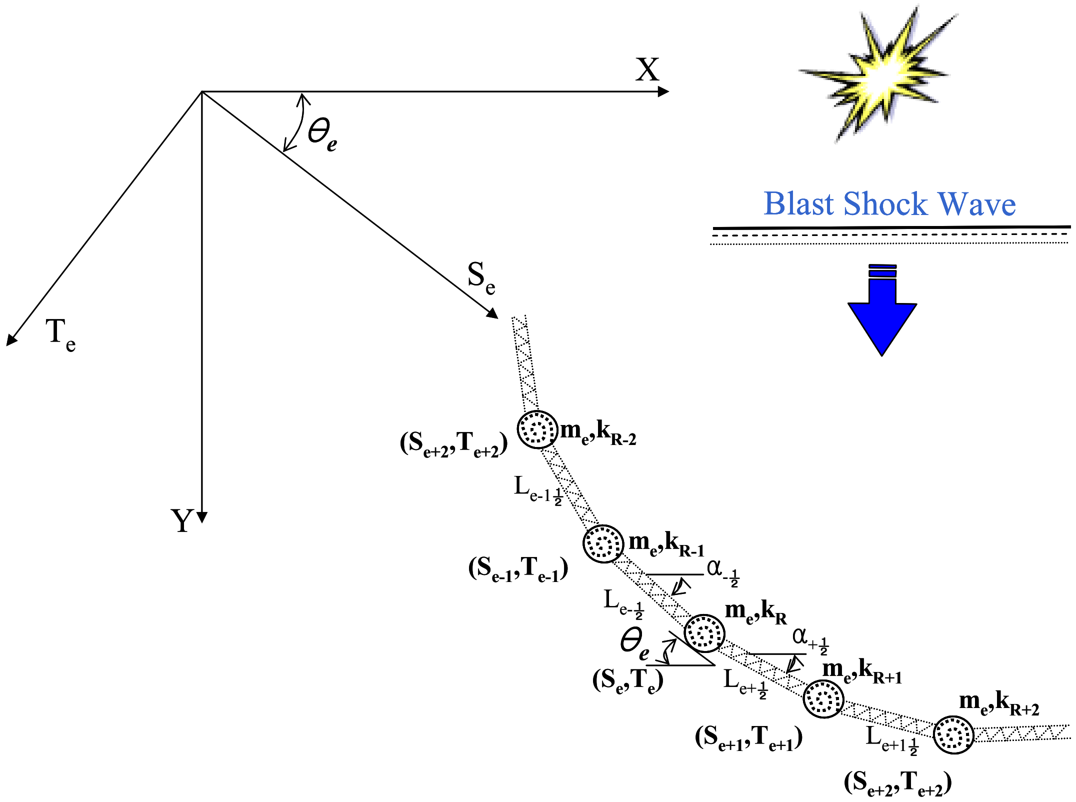

Figure 5.3 Representation of a membrane structure using discretely modeled elements; lumped masses, non-resisting extensible tubes, and rotationary springs

Due to large deformations and the uncoupling of the equations of motion, Scherbatiuk[137] used both a global axis system (X,Y) and a local axis system (S_e,T_e) and θ_e at each node e to derive equations of motion and the resulting pressures as shown in Figure 5.3.

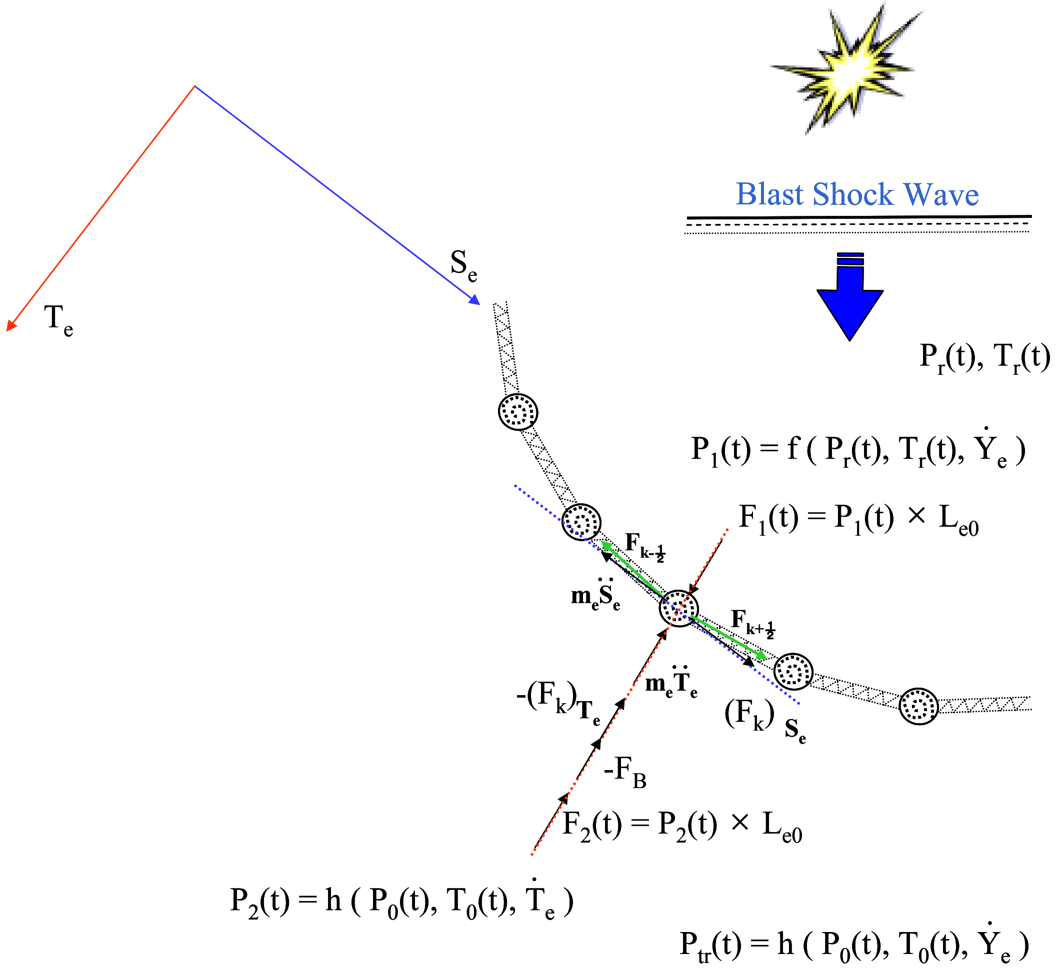

Figure 5.4 Forces applied to a lumped mass element

Figure 5.4 shows the forces applied to a lumped mass element. Based on this free body diagram, the resulting equations of motion in the S_e and T_e directions for node e are as follows:

$$\sum F_{S_e} = 0 = (F_k)_{S_e} - m_e \ddot{S}_e \tag{5.1}$$

$$\sum F_{T_e} = 0 = F_1(t) + (F_k)_{T_e} + F_B - m_e \ddot{T}_e - F_2(t) \tag{5.2}$$

The forces $(F_k)_{Se}$ and $(F_k)_{Te}$ are the sums of the spring forces from the non-resisting extensible tubes attached to the lumped mass in the positive S_e and T_e directions, respectively. The mass of each node is given as m_e, and is the product of the density, initial thickness, and initial element length. The forces $F_1(t)$ and $F_2(t)$ are the applied forces parallel to the T_e direction due to the reflecting shock wave and shock pressure created on the opposing side of the flexural membrane. The bending force F_B is the force applied at the node due to bending resistance, and is dependent on the position of element *e* relative to the adjacent two nodes on either side. The equations for the spring forces and the bending force, explanations, and assumptions made are found in detail in Ref. [137].

The calculation of blast forces which are applied to the discrete models comprises the fluid-structure interaction procedure in Scherbatiuk's work. With the reflected overpressure profiles assumed in $P_r(t)$, he calculated the applied blast forces using Meyer's 1-D method which computes the pressure on both sides of a rigid movable wall from a weak shock wave based on the 1-D velocity of the rigid wall:

$$F_1(t) = P_r(t) \left[\frac{\frac{2a_r(t)}{\gamma - 1} - \dot{Y}_e}{\frac{2a_r(t)}{\gamma - 1}} \right]^{\frac{2\gamma}{\gamma - 1}} \times L_{eo} \tag{5.3}$$

where γ, the ratio of specific heats for gas, was assumed to be 1.4, a_r is the speed of a reflected shock, L_{eo} is the initial element length, and $\dot{Y}_e$ is the node velocity which is given as

$$\dot{Y}_e = \sqrt{\dot{S}_e^{\,2} + \dot{T}_e^{\,2} - (\dot{S}_e \cos\theta_e - \dot{T}_e \sin\theta_e)^2} \tag{5.4}$$

where S_e, T_e, and θ_e are explained in Figure 5.3.

The force resisting the movement of the barrier from the air on the opposing side was based on the velocity normal to the slope of the barrier and is given by

$$F_2(t) = P_0 \left[\frac{\frac{2a_0}{\gamma-1} + \dot{T}_e}{\frac{2a_0}{\gamma-1}} \right]^{\frac{2\gamma}{\gamma-1}} \times L_{eo} \tag{5.5}$$

where a_0 is the speed of sound in the ambient atmosphere.

Then the transmitted overpressure profile is calculated using the following equation:

$$P_T(t) = P_0 \left[\frac{\frac{2a_0}{\gamma-1} - \dot{Y}_e}{\frac{2a_0}{\gamma-1}} \right]^{\frac{2\gamma}{\gamma-1}} - P_0 \tag{5.6}$$

Scherbatiuk's methodology explained above can be considered as a simplified fluid-structure interaction using a staggered algorithm. Based on Scherbatiuk's methodology, a fluid-structure interaction method with a staggered algorithm using more complicated FEM and CFD codes is devised and applied in this chapter to calculate the transmitted blast wave loading inside a simplified 2-D tent structure. The methodology used in this FSI problem is summarized in the flowchart below.

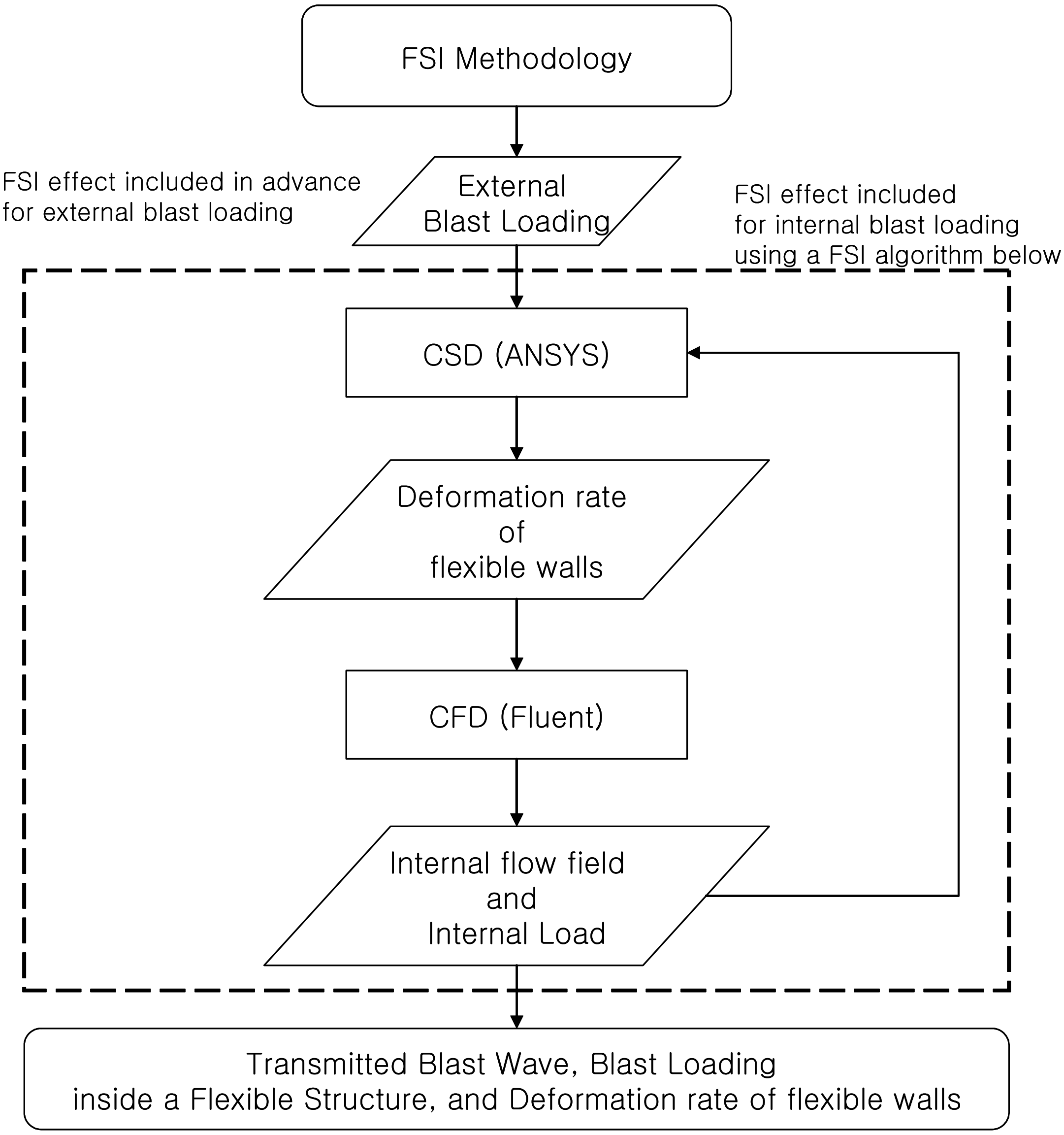

Figure 5.5 A fluid-structure interaction method with a staggered algorithm using both FEM (ANSYS) and CFD (Fluent) codes

In this method involving a fully explicit partitioned or staggered algorithm, which was previously applied in an aeroelastic problem by Bendiksen, CFD and CSD based on FEM were performed iteratively at every intermediate time step, as shown in Figure 5.5, to generate transient boundary conditions during the interaction between the structure and the flow field. Those boundary conditions, the pressure loading for CSD, and the movement of the boundary defining the flow field for CFD are the direct means by which the domains of fluid and structure influence each other. In this study, Fluent and ANSYS are used independently for the CFD analysis and the CSD analysis, as used in each numerical analysis in Chapter 3 and Chapter 4.

For the stage shown in the first box in Figure 5.5, the exterior blast loading over a rigid structure of a 2-D tent shape is estimated using BLAST2.f as in Chapter 2, separate from the fluid-structure interaction, designated by the box of “Result and Loading” in Figure 5.5. With this exterior blast loading as a loading condition, CSD is performed to determine the transient motion of the structure (“Wall Movement” in Figure 5.5) for the first time step in the FSI analysis procedure. This structural motion, used as the moving wall boundary condition for CFD, causes the movement of the air inside the structure. This air movement resists the structural motion through the internal pressure loading (“Internal Loading” in Figure 5.5). Finally, the resultant pressure loading (“Result and Loading” in Figure 5.5) is calculated from the external pressure loading determined in advance and the internal pressure loading for the boundary condition in CSD for the next time step. These sequential processes form an initial and complete routine in the staggered algorithm for the FSI analysis. Then this iterative FSI computation is repeated for a given time duration. While the calculation is performed, the movement of the internal air develops into the increase of pressure on the interior side of the tent, and this movement can be considered as transmitted blast waves through walls which are impacted by the external blast waves.

5.2.2 FEM Modeling for Structural Dynamics

For the transient dynamic analysis of a 2-D tent structure in the CSD calculation, the tent structure is simplified as flexible shell-type membrane structures supported on fixed frames in 3-D as shown in Figure 5.6. The simplified tent made of flexible membrane-type structures and rigid frames is divided into four parts and each part is modeled with quadratic shell-type elements as shown in Figure 5.7, since the transient dynamic analysis is performed with the assumption of no displacement in the rigid frames, and each part surrounded by these frames is not influenced by the motion of the other parts. This division also saves computation time by performing the transient dynamic analysis separately for each part of the four-sided tent structures. Then the transient motion of the structure at the center section of the 3-D structure in the Z-direction is taken as the moving boundary in the 2-D CFD analysis in the iterative FSI routine.

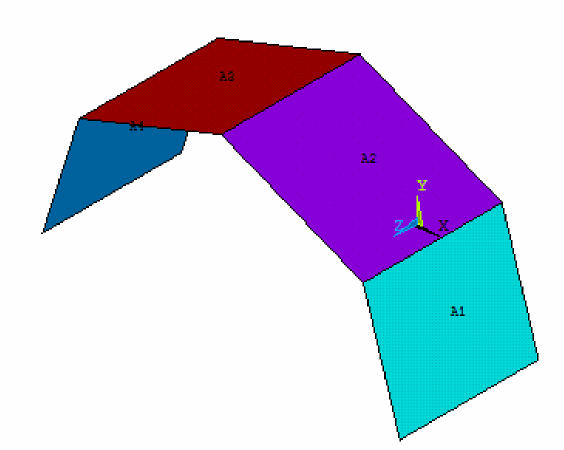

Figure 5.6 Simplified structural model of a tent structure for the FSI analysis

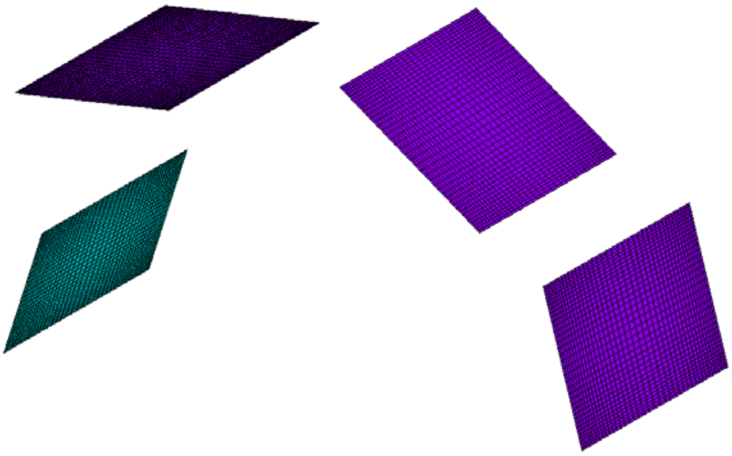

Figure 5.7 FEM modeling of a simplified tent structure with quadratic shell-type elements

The loading conditions applied to each part of membrane-type structure, and its resulting motion, are integrated in the common time history. The shell–type element, SHELL63[134] , which was tested and chosen for the modeling of the flexible structure under dynamic loading in Chapter 4, is used in this FSI analysis study for the structural analysis part using FEM as shown in Figure 5.8. With this element, material and geometric non-linearities due to large deflection of the flexible structure can be modeled with stress stiffening and large deflection capabilities. Details regarding the shell-type elements used in the present work are explained in Chapter 4.

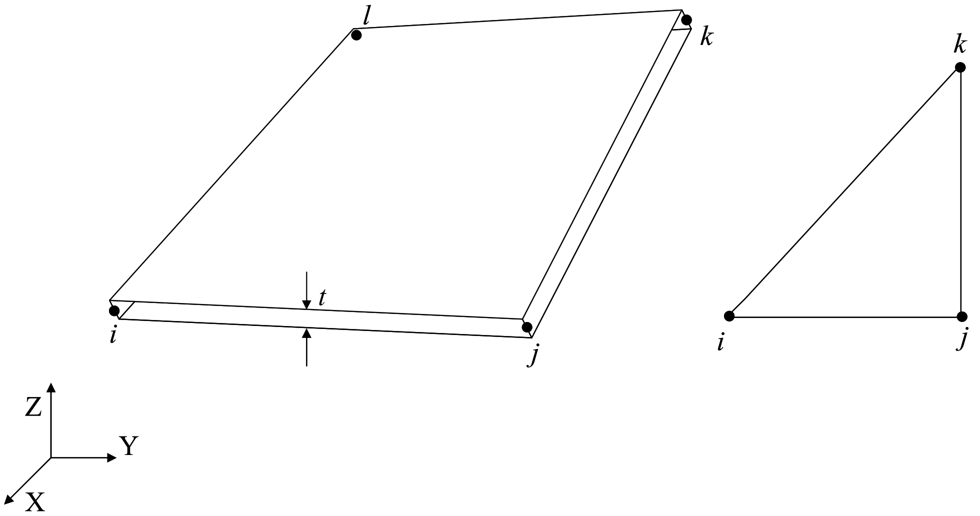

Figure 5.8 Geometric definition of a shell-type element

The pressure loads (the overpressure profiles, see Figure 5.9) applied to each membrane-type structure are obtained using BLAST2.f which takes into account the FSI effect (refer to Sections 2.3 and 2.6). The same blast loading condition is applied in this FSI analysis as shown in Figure 2.10; the TEMPER tent (Figure 1.1) is subjected to an external explosion of 25 kg (55.1 lb) TNT, 65 ft away from the explosion origin as shown in Figure 2.10. It is assumed that the pressure loads on each membrane-type structure is uniform at each time step in the present FSI analysis.

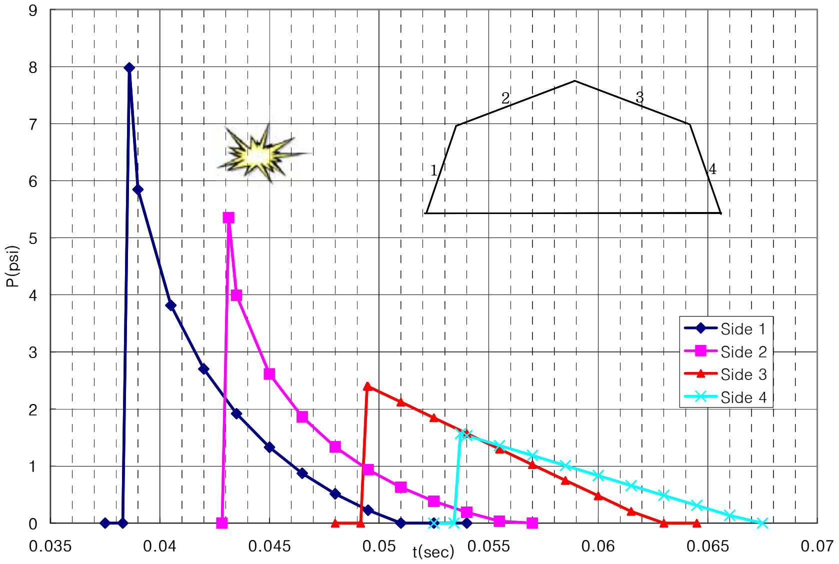

Figure 5.9 Estimated airblast loading over a TEMPER tent

Figure 5.10 shows the imposed displacement and element loads of pressure in the transient dynamic analysis for each flexible membrane-type structure. The full solution method with the Newton-Raphson method and the Newmark method is employed for the non-linear transient analysis at each FSI time step with the corresponding loading conditions. The material properties for the membrane structure are: 3 mm for thickness, 3000 kg/m^3 for density, 250 MPa for Young's modulus, and 0.33 for Poisson's ratio. These values are primarily based on the experimental results explained in Ref. [139]. However, some values are changed with a consideration of the mixed structural properties of both canvas and liner material acting together, and numerical stability required for the structural transient dynamic analysis.

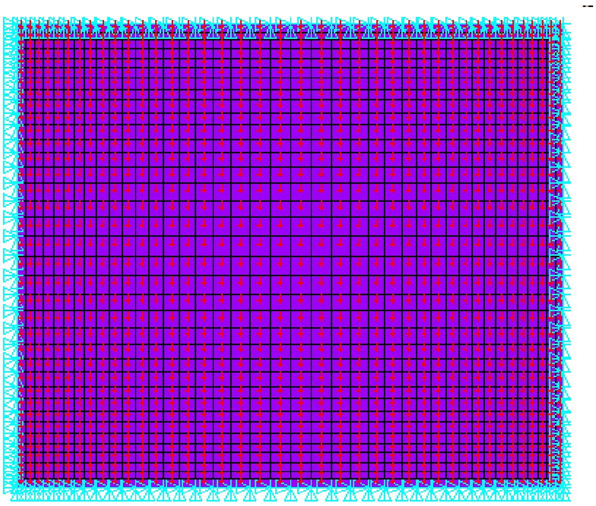

Figure 5.10 Geometric and loading boundary conditions for each membrane

5.2.3 CFD Modeling for Aerodynamics

For the CFD solution, the same numerical methods used for the external flow field in Chapter 3 are implemented in the dynamic flow field solution inside a 2-D tent structure for the FSI analysis. The flow field inside the structure is discretized using unstructured conformal grids (Figure 5.11), and the Euler/Navier-Stokes equations are solved for the coupled, implicit, unsteady motion of the ambient air in the discretized flow field domain. A second-order upwind scheme was chosen for the Euler/Navier-Stokes solver. The dynamic mesh model is updated at each FSI time step by the motions of surrounding moving boundaries (Figure 5.12) which are obtained from the CSD analysis as functions of time and location before the CFD solution is determined.

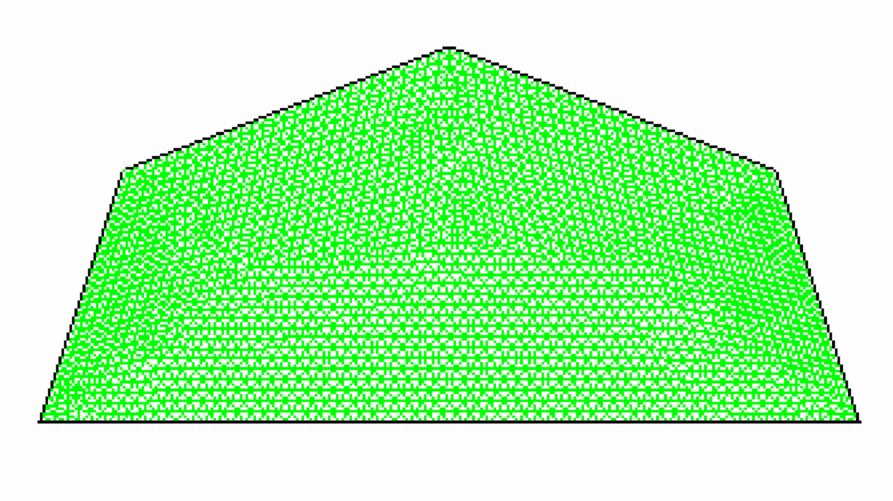

Figure 5.11 Initial flow field domain discretized in unstructured tri-grids

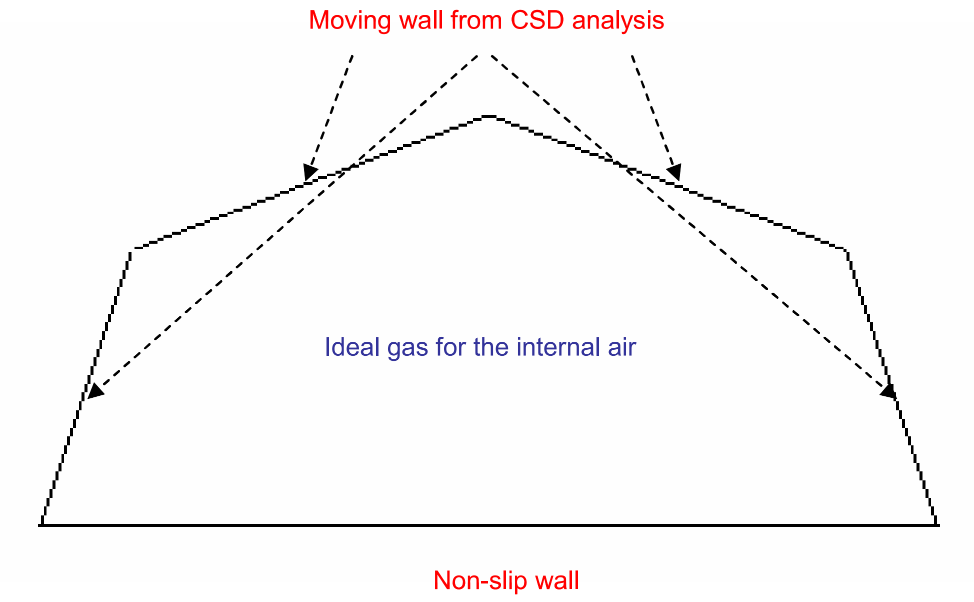

Figure 5.12 Problem geometry and initial/boundary conditions

5.2.4 Results

As the FSI time step marches forward, the surrounding wall is deformed in a short time as computed in the CSD analysis using the resultant pressure loading. With this movement, a high velocity shock front departs from the moving wall into the neighboring air. These transmitted blast waves are determined using the CFD at each FSI time step as the Euler/Navier-Stokes equations are solved for the coupled, implicit, unsteady motion of the internal air in the discretized flow field domain. Figure 5.13 shows the fluid-structure interaction at different time steps. Figure 5.13(a) shows that the structural deformation develops the transmitted weak waves, and Figure 5.13(b) and (c) show the reflection of the transmitted blast waves. This FSI analysis was repeated until the transmitted blast waves reflected against the wall of side 4 and lost their impact energy so that the overpressure showed the tendency of reduction. Figure 5.13(b) and (c) also show the structural motion, in which the deformation on the front side wall is going backward due to the elasticity of the structure and the resisting internal pressure.

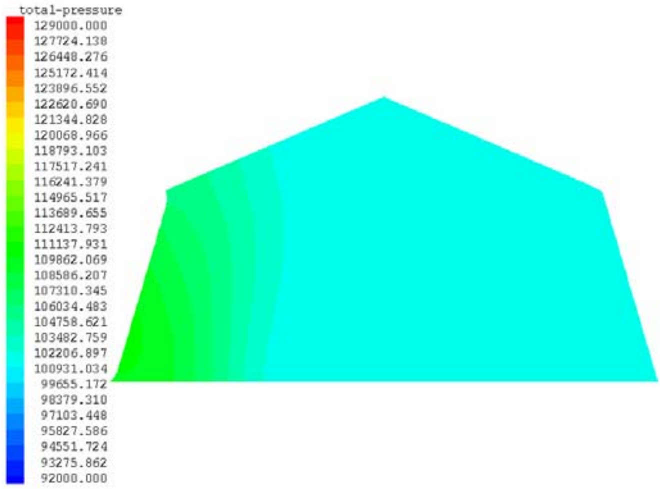

(a) 0.0048 sec

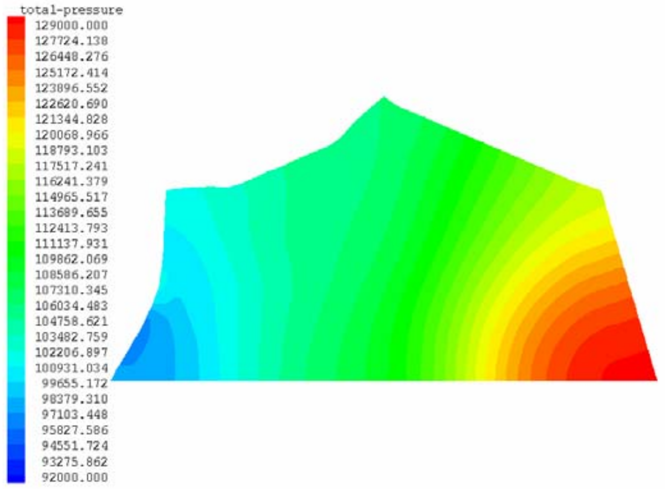

(b) 0.023 sec

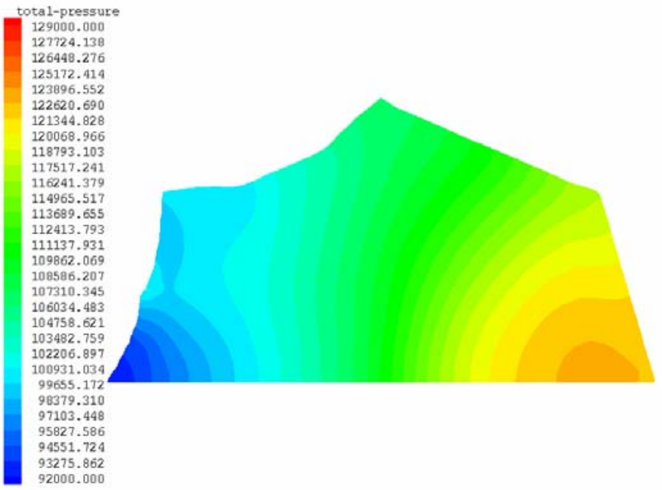

(c) 0.025 sec

Figure 5.13 Total pressure contours inside a tent structure at different instants; total pressure unit is psi.

Subsequently, the blast loading on the interior side of the wall of side 4 (see Figure 5.1) was obtained from this solution, and the results were compared with the field test data and the result from the reduction factor method, as shown in Figure 5.14. This comparison shows that the two methods (the methods of the reduction factor and the FSI analysis) are capable of estimating the transmitted wave pressure loading, and that the FSI analysis using a staggered algorithm can be a useful tool to model the unsteady motion inside a flexible structure reacting to an external explosive blast.

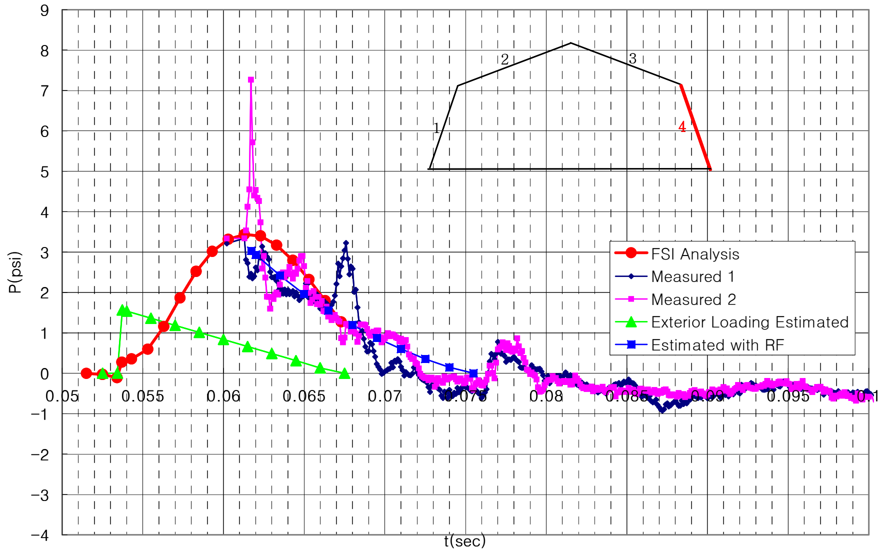

Figure 5.14 Comparison of transmitted blast wave loadings inside a tent

5.3 Blast Wave Propagation over a Flexible Structure

In this section, the dynamic flow field outside a rigid structure, simulating the expansion of the explosive wave over the structure, is solved numerically using a commercial CFD code, Fluent, that can solve various kinds of fluid dynamic problems. This CFD code is particularly suited for this work due to the dynamic mesh model[11] implemented in the most recent version. The dynamic mesh model is updated at each time step by the motion of chosen moving boundaries which are defined as functions of time and location before the computation. The motion of this boundary is sought by comparing the blast loading over the structure calculated from the CFD solution with the blast loading estimated by BLAST2.f.

The case treated in this example is the same as that solved in the calculation of blast loading using BLAST2.f in Section 2.6; the TEMPER tent (Figure 1.1) is subjected to an external explosion of 25 kg (55.1 lb) TNT, 65 ft away from the explosion origin as shown in Figure 2.10.

To compute the blast wave propagation over a flexible structure and the blast loading on a flexible structure, the CFD application done in Chapter 3 should be combined with the non-linear transient dynamic analysis and the transmitted blast wave loading analysis using the FSI analysis as mentioned in Section 5.1.1. The whole methodology for this FSI problem was explained with Scherbatiuk's simplified numerical method[137] in Section 5.2.1. However, in the present research, instead of solving the FSI problems in two different flow fields separated by the flexible structure at the same time, the CFD application done in Section 3.3 is combined with the deflection of the flexible structure obtained in the transmitted blast loading analysis in Section 5.2.4. The inclusion of the FSI effect in the blast wave propagation is implemented by pre-defining the motion of the flexible wall due to the FSI effect using the user-defined motion of walls and the dynamic mesh method in Fluent.

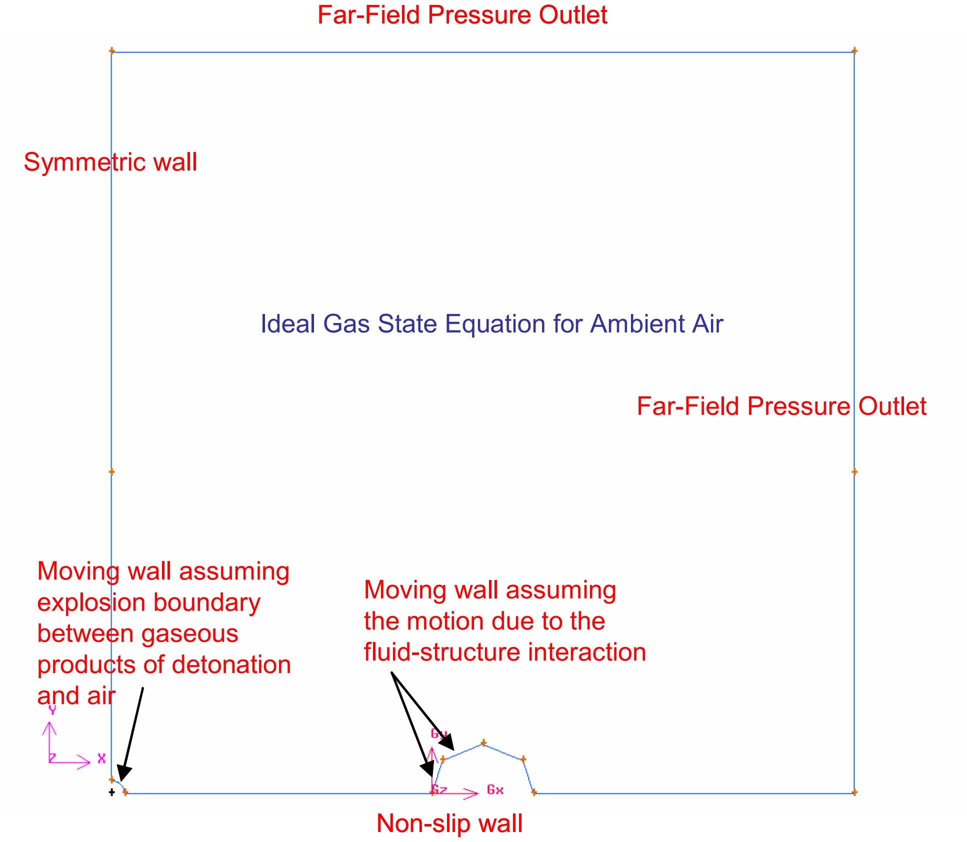

Figure 5.15 Problem geometry and initial/boundary conditions

Figure 5.15 shows the computational domain of the flow field, and the boundary conditions. The defined moving walls are the key concept in simulating this blast wave propagation over the flexible structure. The moving wall is a circular shape as shown in the lower-left corner of Figure 5.15, and models the high explosive charge (refer to Section 3.3 for details). In addition, the front side walls of the tent structure were defined as the moving wall. The motions of those front side walls due to the FSI effect are programmed based on the deflection rate of the flexible structure obtained in the transmitted blast loading analysis. The synchronization problem involving two analyses based on the different time domains was solved by matching the start of the deflection of the flexible structure obtained in the transmitted blast loading analysis with the time when the peak overpressure in numerical simulation of the blast wave propagation over a rigid body arrives at the center of the surface.

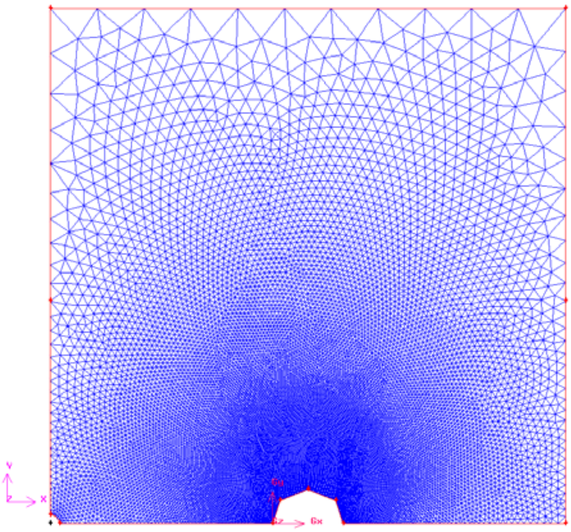

Figure 5.16 Initial flow field domain discretized in unstructured tri-grids

The high explosive charge and the flexible structure are surrounded with unstructured conformal dynamic meshes discretizing the flow field as shown in Figure 5.16. To save computational time, refinement of the mesh is focused near the structure which experiences the blast loading, as shown in Figure 5.16. As the time goes on, the moving walls vary the shape in pre-defined ways and the dynamic meshes also change the shape according to the varying shape of the moving walls.

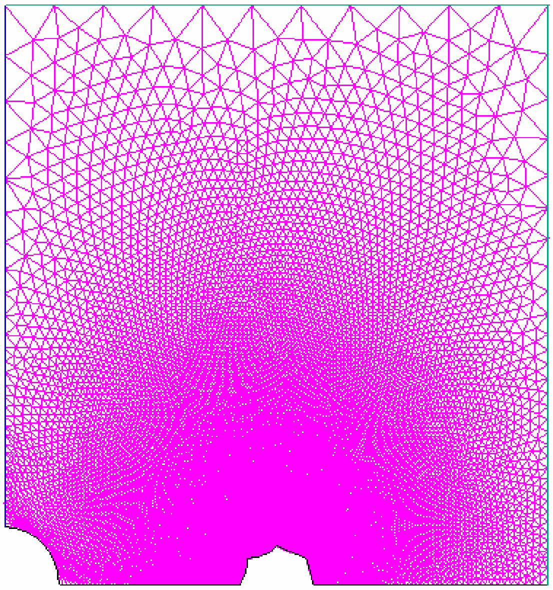

Figure 5.17 The discretized flow field at t = 0.065695 sec showing the changed shape of the moving wall and the dynamics meshes

As the computation is performed, the circular moving wall expands rapidly as shown in Figure 5.17 which is a discretized flow field at an instant of time, which clearly shows the changed shape of the moving walls and the dynamic meshes. The movement of the high explosive charge is defined in detail in Figure 5.18 which (a) shows a pre-defined rate of the change of the radius of a circular moving wall with the maximum Mach number of 1.225, and (b) shows the radius of a circular moving wall varying over time, obtained through the numerical integration of the pre-defined rate of change of the radius of a circular moving wall. With this movement, a high-velocity shock front departs from the moving wall into the surrounding air.

Since the rear side walls do not have as much influence from the FSI effect as the front side walls as the test pressure load data shows, only the front side walls of the tent structure were defined as the moving wall and the FSI effect on the pressure loads was examined in this numerical calculation of blast wave propagation over the flexible structure. The motion of those front side walls due to the FSI effect are programmed based on the deflection rate of the flexible structure obtained in the transmitted blast loading analysis as shown in Figure 5.18 and Figure 5.19. These programmed deflection rates in the form of X and Y components are calculated at each time step for the iterative FSI analysis. In this calculation process, it is assumed that while the deflection rates are varied along the surface, they are averaged over the period of each time step and are constant at each point of the surface over each period of the time step in the CFD calculation. These deflection rates are carefully synchronized in the explicit CFD calculation by matching the start of the deflection of the flexible structure obtained in the transmitted blast loading analysis with the time when the peak overpressure in numerical simulation of the blast wave propagation over a rigid body arrives at the center of the surface. Then, when the explicit time marching in the CFD calculation arrives at the matching time, the moving walls are incorporated to simulate the FSI effect on the front side walls.

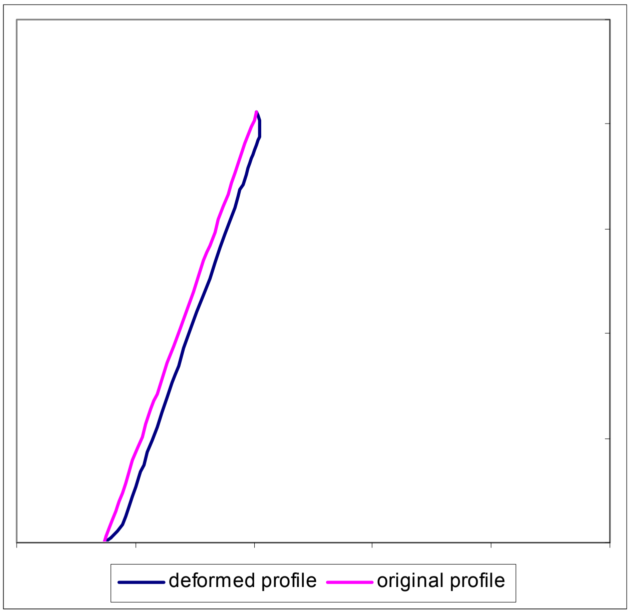

(a) deformed profile shape

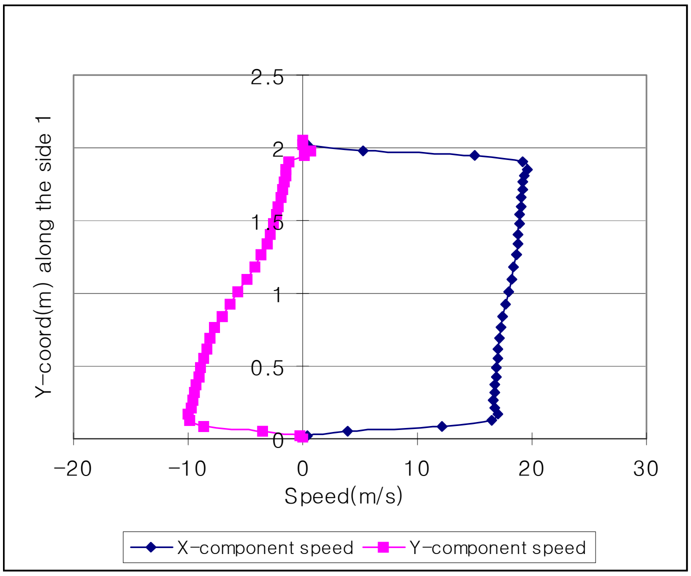

(b) average speed along the deformed profile shape

Figure 5.18 An example of the deformed profile shape and the average speed of the moving wall on Side 1 during a time step in the iterative FSI analysis.

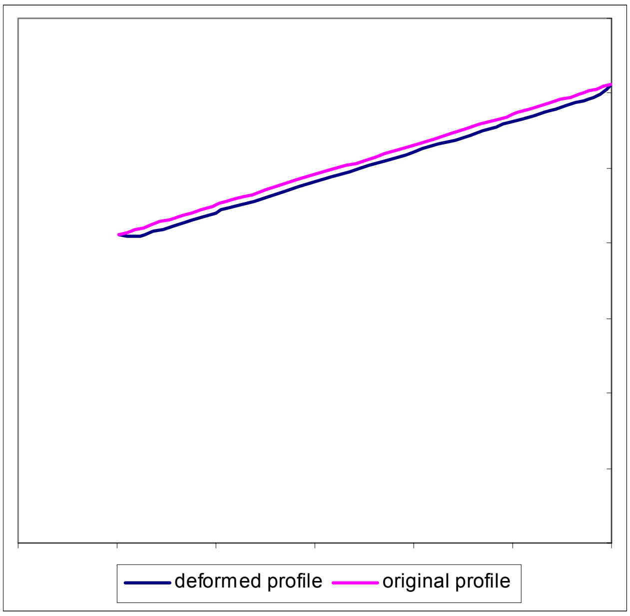

(a) deformed profile shape

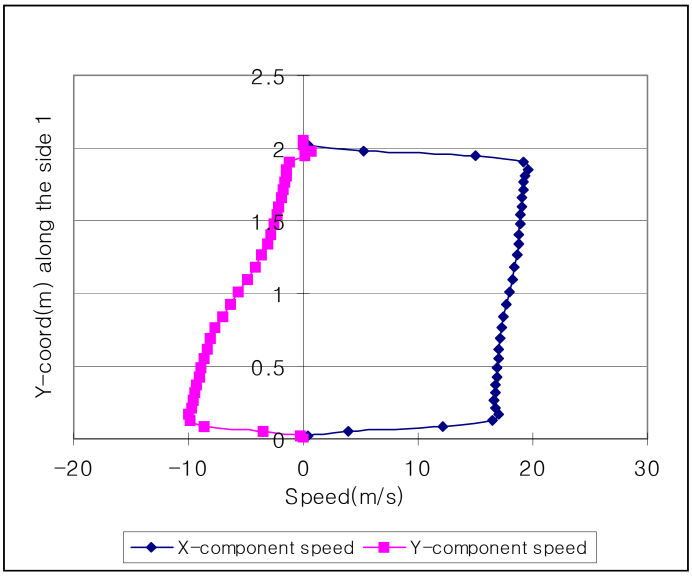

(b) average speed along the deformed profile shape

Figure 5.19 An example of the deformed profile shape and the average speed of the moving wall on Side 2 during a time step in the iterative FSI analysis.

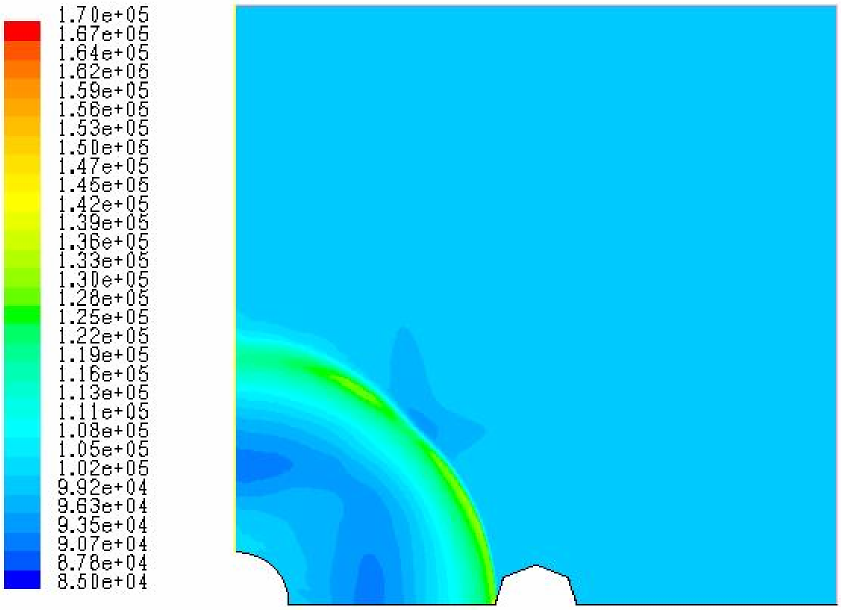

(a) 0.0428 sec

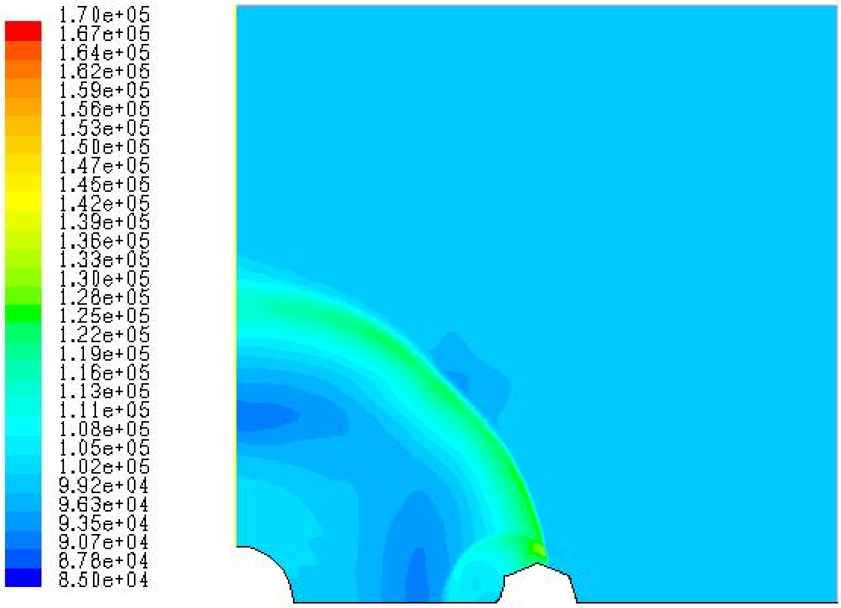

(b) 0.0536 sec

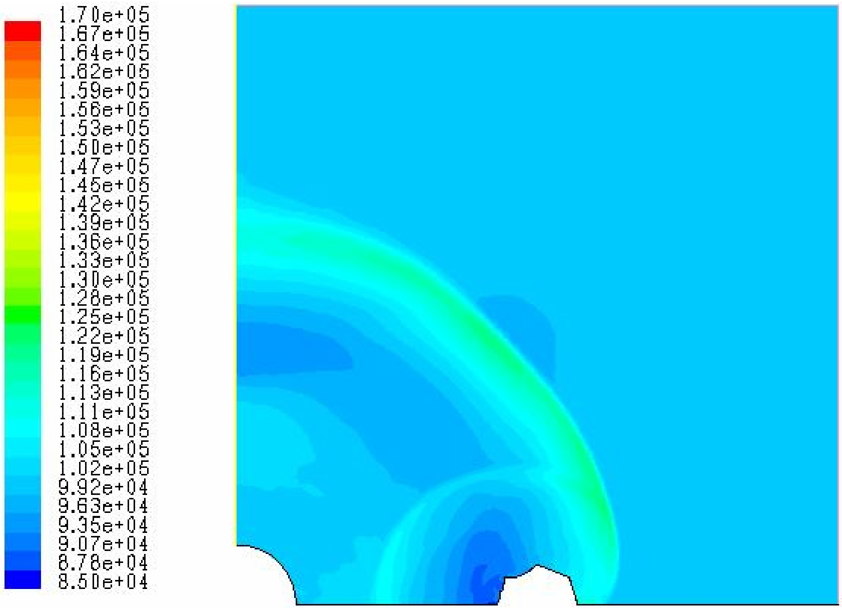

(c) 0.0682 sec

Figure 5.20 Total pressure contours induced by a blast-wave interaction with a tent-shaped flexible structure at different instants; total pressure unit is psi.

Then, Euler/Navier-Stokes equations were solved for the coupled, explicit, unsteady motion of the ambient air in the discretized flow field domain over the period during which the FSI analysis methods are applied for the transmitted blast wave loading in Section 5.2. A second-order, upwind scheme was chosen in the flow discretization and the Courant number was set to 0.1 as was done in Section 3.3. The propagation and the reflection of the airblast wave against the moving walls are shown in the results from this numerical solution; Figure 5.20 (a) shows the flow field before the blast wave is reflected against the front wall, and Figure 5.20 (b) and (c) show the flow field after the blast wave passed over the flexible structure. This numerical simulation result of the blast wave propagation is almost the same as shown in Figure 3.5. Since the convergence of the numerical calculations was examined and verified in Section 3.3, this numerical result is accepted as properly solved.

Finally, the blast loading over the moving walls were obtained from this CFD solution. The pressure loads, *i.e.,* the overpressure profiles obtained at the center of each wall, were plotted with the pressure loads obtained from other calculation methods and the field tests in Figure 5.21 and Figure 5.22. Comparison of overpressure profiles in Figure 5.21 shows that the overpressure profiles of the CFD solution with the FSI effect decrease more rapidly than the overpressure profiles of the CFD solution without the FSI effect. This tendency clearly shows that the results of the CFD solution with the FSI effect includes the wall flexibility effect on the overpressure profiles. In Figure 5.21, the estimated overpressure profiles are obtained with R=S=1.0, which means that no flexibility is considered (see Section 2.3 about the values of R and S). The comparison of the overpressure profiles between the CFD solution and the estimation in Figure 5.21 was already explained in Section 3.3 and Figure 3.7, where the CFD solution was performed with the rigid structure.

Comparison of overpressure profiles in Figure 5.22 shows that the overpressure profiles of the CFD solution with the FSI effect are closer to the field test data and the estimation with the values of R and S. This comparion clearly shows that the proposed FSI analysis can include the flexibility effect on the pressure loads obtained using the CFD solution. Therefore, the FSI effect should be considered in the pressure load calculation on the structure where the structural deflection rate can influence the solution of the flow field surrounding the structure.

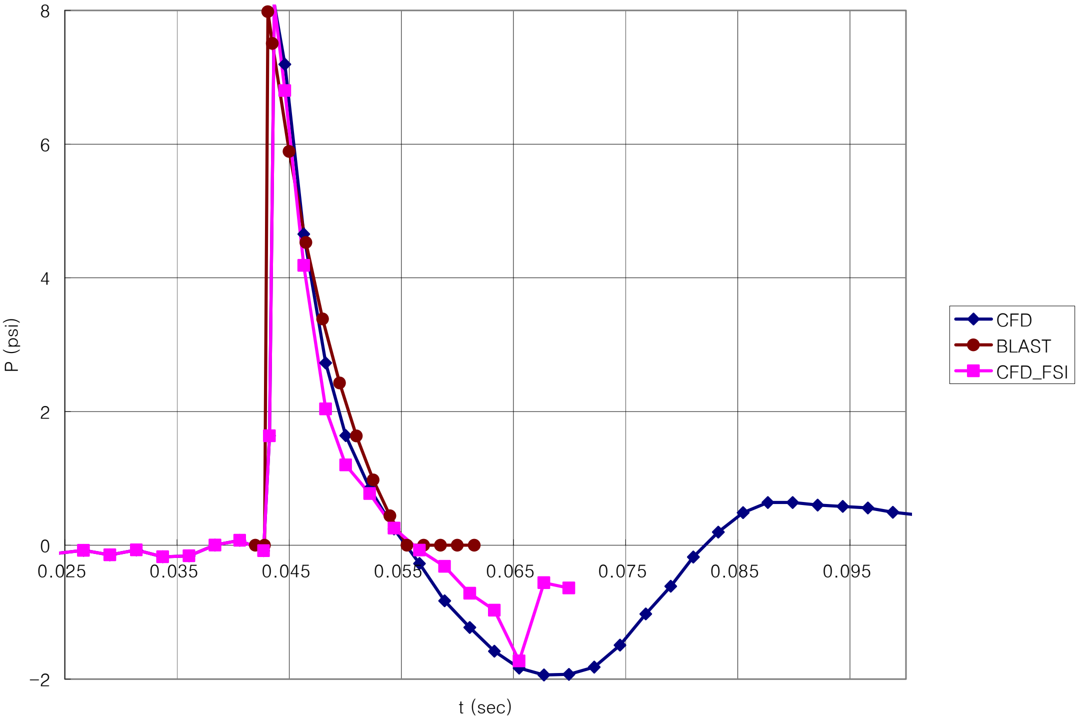
8
6
4
2
0
−2
P (psi)
0.025
0.035
0.045
0.055
0.065
0.075
0.085
0.095
t (sec)
CFD
BLAST
CFD_FSI

(a) side 1

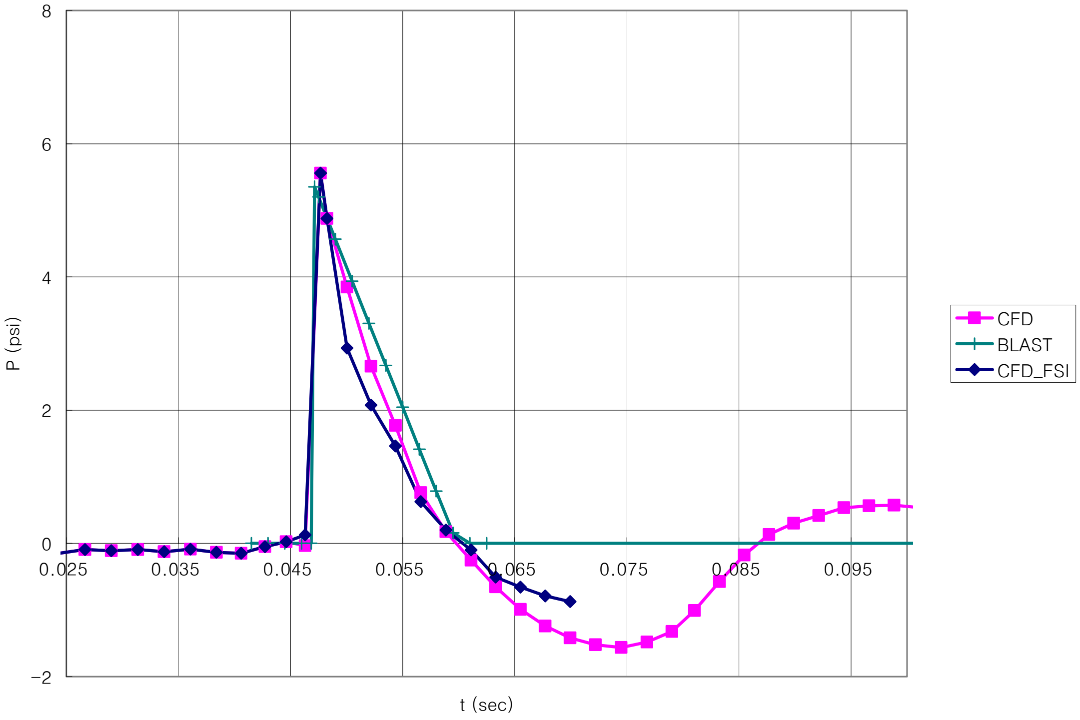

(b) side 2

Figure 5.21 Comparison of overpressure profiles; BLAST is a result estimated using the BLAST2.f program for a rigid structure, CFD is a result obtained from the numerical simulation using Fluent for a rigid structure, and CFD_FSI is a result obtained from the numerical simulation using Fluent for a flexible structure

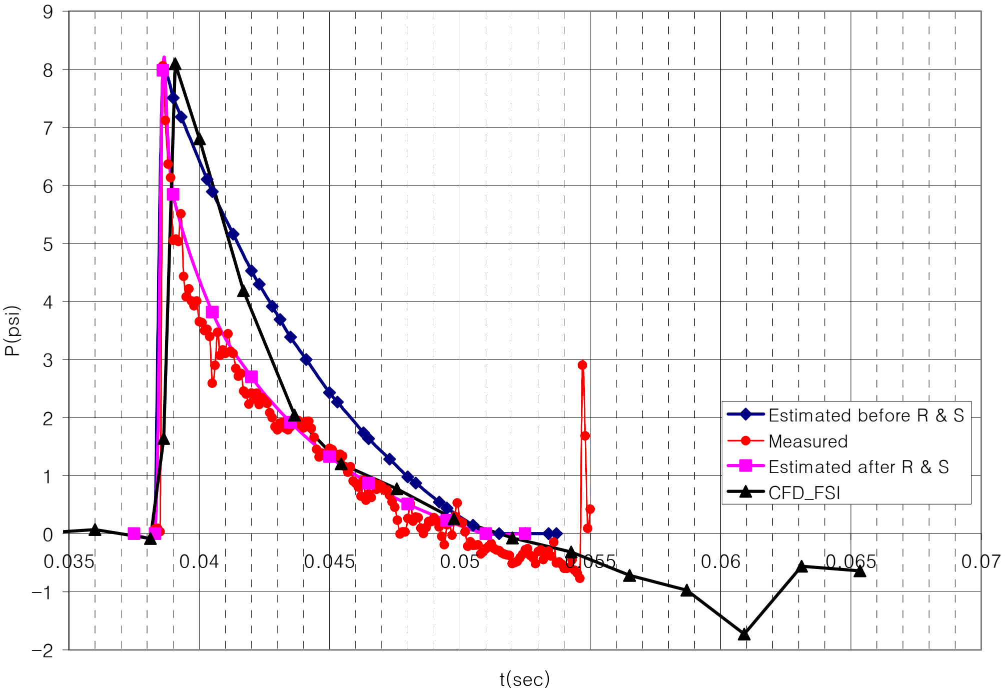
P(psi)
t(sec)
9
8
7
6
5
4
3
2
1
0
−1
−2
0.035
0.04
0.045
0.05
0.055
0.06
0.065
0.07
Estimated before R & S
Measured
Estimated after R & S
CFD_FSI

(a) side 1

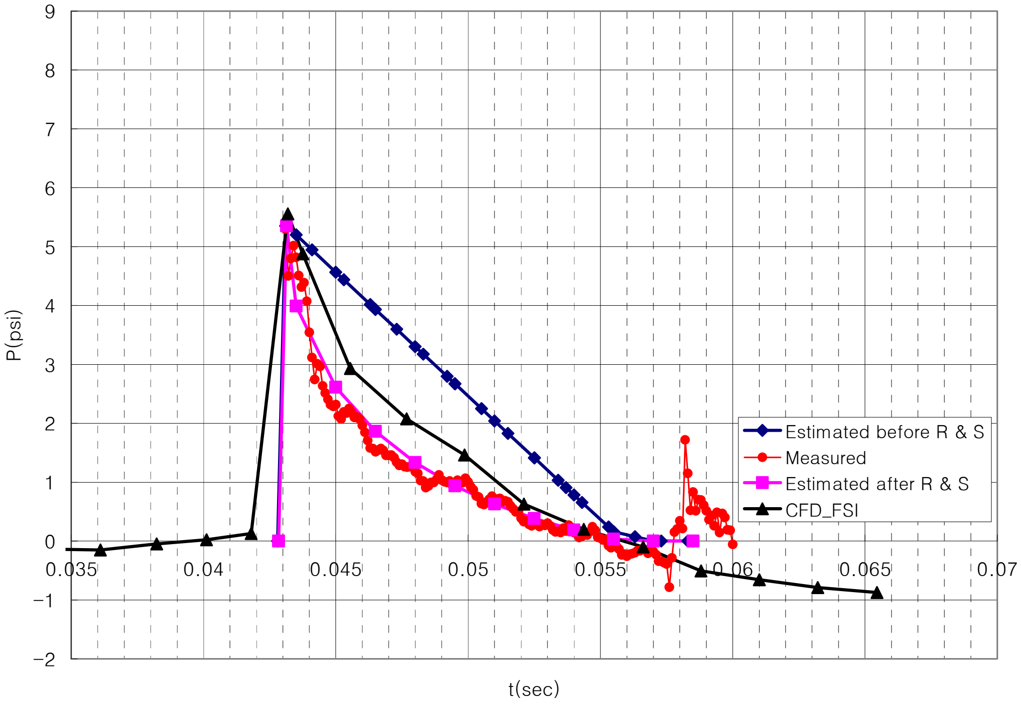

(b) side 2

Figure 5.22 Comparison of overpressure profiles; Estimated before R & S is a result estimated using the BLAST2.f program for a rigid structure, Measured is a result obtained from the field test, Estimated after R & S is a result estimated using the BLAST2.f program for a flexible structure, and CFD_FSI is a result obtained from the numerical simulation using Fluent for a flexible structure

Chapter 6

6.1 Conclusions

Recently, numerous flexible structures have been employed in various fields of industry for both governmental and civilian purposes. In many cases, however, loading conditions sustained by these flexible structures are not described qualitatively nor quantitatively for engineering analyses even though these conditions are important design criteria. One of those cases is analyzed in the present work, where a flexible tent with a Collective Protection System (CPS) is subjected to an explosion. Collective protection has become an important aspect of military shelters. The objective of the CPS is to protect personnel from biological and chemical agents with a pressurized liner inside the tent as an environmental barrier. Field tests involving explosive blast pressures on the tent showed unexpected damage to the liner, and most of the damage occurred on the side of the tent opposite to the blast location, due largely to internal pressure waves. To solve this problem, various tests and analyses have been performed, involving material characteristics of the liner, canvas, and zip seals, modeling of the blast loading over the tent and the resulting dynamic pressure loading inside the tent, structural analysis of the tent under the blast loading, and the characteristics of the structural response to the blast. It was found that the blast loading and the structural response can not be analyzed separately due to the interaction between the flexible structure and the dynamic pressure loading.

In this dissertation, loading conditions sustained by a typical flexible structures, a flexible tent with a CPS, under airblast explosions were analyzed qualitatively and quantitatively. The dynamic loadings imposed on both interior and exterior sides of the tent structure due to the airblasts, and the following dynamic responses, were mainly explored with the BLAST2.f program of simple analytical/empirical methods and a numerical method of an iterative fluid-structure interaction using Computational Fluid Dynamics (CFD) and Computational Structural Dynamics (CSD). All the numerical results and estimations were compared with the field test data conducted by the Air Force Research Laboratory. The experimental pressure data were gathered from pressure gauges attached to the tent surfaces at different locations. The comparison shows that the methods proposed in the present work can be a good design tool to analyze the loading conditions for rigid or flexible structures under an explosive situation. In particular, the causes of the failure of the liner on the leeward were explained with the blast loading on the internal and external surface in the leeward side of the tent . Also, the results showed that the effect of fluid-structure interaction should be considered in the pressure load calculation on the structure where the structural deflection rate can influence the solution of the flow field surrounding the structure. Finally, through these comparisons, the analytical/empirical methods and the numerical methods of the FSI analysis using CFD and CSD was validated.

The achievements in the present research can be summarized as follows: First, the program BLAST2.f was developed to estimate the external blast wave loading over rigid or flexible structures. Overpressure profiles over the whole structure were modeled based on the Friedlander's equation. In this modeling process, a modified profile for reflected overpressures was proposed for different parts of the cross section and the flexibility of the structure was taken into account. The newly proposed equation for the overpressure profile for the flexible structure involves two parameters, and proper choices of these parameters led to good agreement between pressures from the numerical model and from the field test data. The explosion is assumed to occur on one side (the front, or windward, side).

Second, a numerical method using a CFD code with a moving-wall boundary condition and dynamic mesh model was applied to simulate the propagation of the airblast wave and then to calculate the airblast loading over a structure in 2-D cross section. In this numerical simulation of the blast wave propagation over a structure, a new method for the explosion charge was suggested by modeling the explosion charge using the moving wall boundary conditions. It was also verified in this solution that the selection of a viscous solver (Navier-Stokes) or an inviscid solver (Euler) did not make a significant difference to the results. Through this simulation, the blast loading in the negative phase and the second shock could be predicted. Therefore, this numerical simulation and the corresponding blast loading prediction can complement the estimation of the blast loading by the BLAST2.f program.

Third, the transmitted blast wave loading inside the flexible structure was estimated using a proposed empirical method of the reduction factor which was proposed in the present work based on the examination of the similar field test data, and also using the Fluid-Structure Interaction (FSI) analysis (a staggered algorithm using more complicated finite element and CFD codes). The empirical method and the numerical simulation using the FSI analysis showed that the interior transmitted blast wave loading could produce large dynamic loads on the liner inside the leeward surfaces of the tent.

Finally, the numerical simulation of the blast wave propagation using the CFD and the deflection rates calculated through the transmitted blast wave loading analysis were combined to simulate the blast wave propagation over the flexible structure and to calculate the pressure loads on the flexible structure. The results show that the FSI effect should be considered in the pressure load calculation on the structure where the structural deflection rate can influence the solution of the flow field surrounding the structure.

6.2 Recommendations for Future Work

The estimation models for the pressure loads on the flexible structure under the airblast loading should be compared with various field tests so that the newly introduced parameters for the FSI effect could be established.

The numerical modeling of the airblast and the structural response can be extended. For example, the dynamic pressure loading was considered for a cross section of the tent. Extension to a three-dimensional pressure model would provide improved results, and could utilize the 3-D finite element model of the frame.

The numerical modeling of the airblast and the structural response and the calculation of pressure loading on the deforming structure showing the FSI effect could be extended and applied to various design problems. For example, the blast wave pressure loading was considered for a cross section of the tent and needs to be applied to a three-dimensional pressure model so that the proposed numerical methodology using the FSI effect would produce a good example for the well-established numerical process considering the FSI problems and show the practical problems to be resolved for the simplified application of the FSI analysis.

Then, this method can be extended to various design problems such as non-linear aeroelasticity problems, specially for morphing wings, low Reynolds number unmanned air vehicles (UAVs) or structural analysis in which unsteady response is a dominant effect.

This application of the FSI analysis is also a good example for taking advantage of parallel processing since the flow field domain can be divided by the flexible structure and so the application of parallel processing for the divided flow fields can save the computational time needed for the iterative FSI analysis.

References

1. Otto, F., Tensile Structures: Design, Structure, and Calculation of Building of Cables, Nets, and Membranes, The MIT Press, Cambridge, MA, 1973.

2. Heki, K., ed., Shells, Membranes, and Space Frames, Proceedings of the IASS Symposium on Membrane Structures and Space Frames, Osaka, Japan, September 15-19, 1986.

3. Crawford, J. E. and Morill, K. B., ”Development of a Lightweight, Portable Airblast Barrier*”,* 16th International Symposium on Military Aspects of Blast and Shock (MABS16), Keble College, Oxford, UK, September 10-15, 2000

4. Cadogan, D. P. and Scarborough, S. E., “Rigidizable Materials for Use in Gossamer Space Inflatable Structures,” *Proceedings of the 42nd AIAA/ASME/ASCE/AHS/ASC Structures, Structural Dynamics and Materials Conference & Exhibit, AIAA Gossamer Spacecraft Forum*, Seattle, WA, AIAA Paper 2001-1417, April 2001.

5. Cadogan, D. P., Smith, T., Lee, R., Scarborough, S. E., and Graziosi, D., “Inflatable and Rigidizable Wing Components for Unmanned Aerial Vehicles,” *Proceedings of the 44th AIAA/ASME/ASCE/AHS/ASC Structures, Structural Dynamics and Materials Conference*, Norfolk, VA, AIAA Paper 2003-1801, April 2003.

6. Manfield, P., “A Comparative Study of Temporary Shelters used in Cold Climates,” Ph.D. Dissertation, Department of Architecture, Cambridge University, February 2000.

7. http://www.natick.army.mil/soldier/jocotas/ColPro_Papers/Porter.pdf

8. http://www.natick.army.mil/soldier/media/fact/shelter/lams.htm

9. Chun, S., Kapoor, H., Kapania, R. K., Motley, M. R., and Plaut, R. H., “Modeling the Response of Collective Protection Systems to Airblasts,” VPI-AOE-290 Report to U.S. Air Force Research Laboratory, Tyndall Air Force Base, Florida, June, 2004

10. Chock, J. M. K., “Review of Methods for Calculating Pressure Profiles of Explosive Airblast and its Sample Application,” M.S. Thesis, Aerospace Engineering, Virginia Tech, April 1999.

11. Fluent 6.1 User’s Guide, February 2003.

12. Morand, H. J. P. and Ohayon, R., *Fluid Structure Interaction – Applied Numerical Methods*, Wiley, New York, 1995.

13. Schafer, M., “Coupled Fluid-Solid Problems: Survey on Numerical Approaches and Applications,” Emerging Technology in Fluids, Structures and Fluid-Structure Interactions, Cheng, W and Itoh, S., eds., PVP-VOL. 460, PVP2003-1942, ASME, New York, 2003.

14. Bendiksen, O. O., “A New Approach to Computational Aeroelasticity,” Proceedings of *32nd AIAA/ASME/ASCE/AHS/ASC Structures, Structural Dynamics, and Materials Conference*, Baltimore, MD, AIAA Paper 9100939, April. 1991, pp. 1712-1727.

15. Park, K. C., Felippa, C. A. and DeRuntz, J. A., “Stabilization of Staggered Solution Procedures for Fluid-Structure Interaction Analysis,” Computational Methods in Fluid-Structure Interaction Problems, Proceedings of the Winter Annual Meeting, Atlanta, GA, 1977, pp. 95-124.

16. Doolittle, C., “Blast Phenomena,” in Shock and Vibration Computer Programs: Reviews and Summaries, Pilkey, W. and Pilkey, B., eds., Booz Allen & Hamilton, Arlington, VA, 1995, pp. 55 – 103.

17. Norris, C. H., Hansen, R. J., Holley, M. J., Biggs, J. M., Namyet, S., and Minami, J. K., *Structural Design for Dynamic Loads*, McGraw-Hill, New York, 1959, pp. 239 – 278.

18. Baker, W. E., *Explosions in Air*, University of Texas Press, Austin, 1973.

19. Baker, W. E., Cox, P. A., Westine, P. S., Kulesz, J. J., and Strehlow, R. A., *Explosion Hazards and Evaluation*, Elsevier, New York, 1983.

20. Smith, P. D. and Hetherington, J. G., *Blast and Ballistic Loading of Structures*, Butterworth-Heinemann, Oxford, U.K., 1994.

21. Bulson, P. S., *Explosive Loading of Engineering Structures*, E & FN Spon, London, 1997.

22. Tedesco, J. W., McDougal, W. G., and Ross, A. C., *Structural Dynamics*, Addison-Wesley, Menlo Park, CA, 1999.

23. Srivastava, R. S., *Interaction of Shock Waves*, Kluwer, Dordrecht, The Netherlands, 1994.

24. Hinman, E. E. and Hammond, D. J., *Lessons From the Oklahoma City Bombing: Defensive Design Techniques*, ASCE, New York, 1997.

25. U.S. Army Materiel Command, *Engineering Design Handbook: Explosions in Air Part One* AD/A-003 817 (AMC Pamphlet AMCP 706-181), Alexandria, VA, 1974.

26. Kingery, C. N. and Bulmash, G., “Airblast Parameters from TNT Spherical Air Burst and Hemispherical Surface Burst,” Technical Report ARBRL-TR-02555, AD-B082 713, U.S. Army Ballistic Research Laboratory, Aberdeen Proving Grounds, MD, April 1984.

27. Department of the Army, “Fundamentals of Protective Design for Conventional Weapons,” Technical Manual TM 5-855-1, November 1986, pp. 3-1 - 3-29.

28. Belotserkovskii, O. M. and Chushkin, P. I., “The Numerical Solution of Problems in Gas Dynamics,” in Basic Developments in Fluid Dynamics, Holt, M., ed., vol. 1, Academic Press, New York, 1965.

29. Courant, R., Friedrichs, K. O., and Lewy, H., “Uber die partielle Differentialgleichungen der mathematischen Physik,” Mathematische Annalen, vol. 100, pp. 32-74, 1928.

30. Richtmyer, R. D., Difference Methods for Initial Value Problems, Interscience Publishers, New York, 1957.

31. Godunov, S. K. and Ryaben’kii, V. S., *Theory of Difference Schemes, An Introduction*, Interscience Publishers, New York, 1964.

32. Dorodnitsyn, A. A., *Method of the Integral Relations of the Numerical Solution of Partial Differential Equations*, The Academy of Sciences of the USSR, Moscow, 1958.

33. Dorodnitsyn, A. A. and Chushkin, P. I., *Modern Problems in Computational Aerohydrodynamics*, CRC Press, Boca Raton, FL, 1992.

34. Courant, R. and Friedrichs, K. O., *Supersonic Flow and Shock Waves*, Wiley, New York, 1948.

35. Holt, M., "The Method of Characteristics for Steady Supersonic Rotational Flow in Three Dimensions," Journal of Fluid Mechanics, vol. 1, pp. 409-423, 1956.

36. von Neumann, J. and Richtmyer, R. D., "A Method for the Numerical Calculations of Hydrodynamic Shock," Journal of Applied Physics, vol. 21, pp. 232-237, 1950.

37. Lax, P. D., "Weak Solution of Non-linear Hyperbolic Equations and its Numerical Computations," Communications on Pure and Applied Mathematics, vol. 7, pp. 159-193, 1954.

38. Goldstine, H. H. and von Neumann, J., "Blast Wave Calculation," Communications on Pure and Applied Mathematics, vol. 8, pp. 327-354, 1955.

39. Brode, H., "Numerical Solutions of Spherical Blast Waves," Journal of Applied Physics, vol. 26, pp. 766-775, 1955.

40. Brode, H. L, "Blast waves from a spherical charge," The Physics of Fluids, vol. 2, pp. 217-229, 1959.

41. Sedov, L. I., *Similarity and Dimensional Methods in Mechanics*, Academic Press, New York, 1959.

42. Sakurai, A., "Blast Wave Theory," in Basic Developments in Fluid Dynamics, Holt, M., ed., vol. 1, Academic Press, New York, pp. 309-375, 1965.

43. Chou, P. C., Karpp, R. R., and Huang, S. L., "Numerical Calculation of Blast Waves by the Method of Characteristics," AIAA Journal, vol. 5, pp. 618-623, 1967.

44. Thompson, B. W., “Some Semi-Analytical Methods in Numerical Fluid Dynamics”, Proceedings of the Second International Conference on Numerical Methods in Fluid Dynamics, Springer-Verlag, New York, pp. 73-77, 1971.

45. Oppenheim, A. K., Kuhl, A. L., and Kamel, M. M., “On Self-Similar Blast Waves headed by the Chapman-Jouguet Detonation,” Journal of Fluid Mechanics, vol. 55, pp. 257-270, 1972.

46. Ransom, V. H., Thompson, H. D., and Hoffman, J. D., “Stability and Accuracy Studies on a Second-Order Method of Characteristics Scheme for Three-Dimensional, Steady, Supersonic Flow”, Proceedings of the Second International Conference on Numerical Methods in Fluid Dynamics, Springer-Verlag, New York, pp. 236-242, 1971.

47. Tyler, L. D., “Heuristic Analysis of Convective Finite Difference Techniques”, Proceedings of the Second International Conference on Numerical Methods in Fluid Dynamics, Springer-Verlag, New York, pp. 314-319, 1971.

48. Brode, H. L., Glass, I. I. and Oppenheim, A. K., “Gasdynamics of Explosions Today,” Proceedings of the Eighth International Shock Tube Symposium, Imperial College of Science and Technology, Stollery, J. L., Gaydon, A. G., and Owen, P. R., eds., London, England, July 1971, pp. 2/1-2/56.

49. Hicks, D. L., “One-Dimensional Lagrangian Hydrodynamics and the IDLH Hydrocode,” Mathematical Computing Services Division, 9422, Sandia Laboratories, Albuquerque, NASA Report N70-28044, December 1969.

50. Richtmyer, R. D. and Morton, K. W., *Difference Method for Initial Value Problems,* 2nd edition, Interscience Publishers, New York, 1967.

51. Hicks, D. L. and Walsh, R. T., “Numerical and Computational Analysis of the Partial Differential Equations in Hydrocodes and Wavecodes,” NASA Report N77-19811, 1976.

52. Hicks, D. L., Lauson, H. S., and Madsen, M. M., “Development of THREEDY: A Three Dimensional Wavecode using Operator Splitting and Wavefitting on a Movable Mesh,” NASA Report N75-17129, 1974.

53. Hicks, D. L., and Madsen, M. M., “SKTWO: A Two-Dimensional Lagrangean Wavecode with Shock Fitting,” NASA Report N79-28933, 1979.

54. Mader, C. L., “Fortran BKW – A code for computing the detonation properties of explosives,” NASA Report N67-38188, 1967.

55. Gage, W. R., and Mader, C. L., “TwoDE – A Two-Dimensional Eulerian Hydrodynamic Code for Computing One Component Reactive Hydrodynamic Problems,” NASA Report N67-25433, 1967.

56. Mader, C. L., *Numerical Modeling of Explosives and Propellants*, 2nd edition, CRC Press, New York, 1998.

57. Zukas, J. A., Segletes, S. B., and Furlong, J. R., “Hydrocodes Support Visualization of Shock-Wave Phenomena,” Computers in Physics. vol. 6, pp. 146-154, 1992.

58. Mair, H. U., “Review: Hydrocodes for Structural Response to Underwater Explosions,” Shock and Vibration, vol. 6, 1999, pp. 81-96

59. Mahmadi, K., Aquelet, N. O., and Souli, M., “High Explosion Impact Analysis using LS-DYNA,” PVP-Vol. 460, Emerging Technology in Fluids, Structures and Fluid-Structure Interactions, PVP2003-1942, ASME, 2003, pp. 243-251.

60. Richtmyer, R. D., "Methods for (Generally Unsteady) Flows with Shocks: A Brief Review," 3rd International Conference on Numerical Methods in Fluid Mechanics, vol.1, Paris, France, July 1972, pp. 72-81.

61. Korobeinikov, V. P., Markov, V. V., Chushkin, P. I., Shurshalov, L. V., "Numerical Solutions of Blast Wave Propagation Problems," 3rd International Conference on Numerical Methods in Fluid Mechanics, vol. 2, Paris, France, 1972, pp. 169-175.

62. Erdos, J. I., and Del Guidice, P. D., "Gas Dynamics of Muzzle Blast," Proceedings of 7th AIAA Fluid and Plasma Dynamics Conference, Palo Alto, CA, June 1974, AIAA Paper 74-532.

63. Glaz, H. M., "Development of Random Choice Numerical Methods for Blast Wave Problems," NASA Report N79-32439, 1979.

64. Eidelman, S. and Burcat, A., "Numerical Solution of a Nonsteady Blast Wave Propagation in Two-Phase/Separated Flow/Reactive Medium," Journal of Computational Physics. vol. 39, pp. 456-472, 1981.

65. Colella, P., Ferguson, R. E., Glaz, H. M., and Kuhl, A. L., "Mach Reflection from an HE-Driven Blast Wave," Dynamics of Explosions, Bowen, J. R., Leyer, J. C., and Soloukhin, R. I., eds., vol. 106, Progress in Astronautics and Aeronautics, New York, 1986, pp. 388-421

66. Glaz, H. M., Walter, P. A., Glass, I. I., and Hu, T. C. J., "Oblique Shock Wave Reflections in SF6: A Comparison of Calculation and Experiment," Dynamics of Explosions, Bowen, J. R., Leyer, J. C., and Soloukhin, R. I., eds., vol. 106, Progress in Astronautics and Aeronautics, New York, 1986, pp. 359-387

67. Glaz, H., Colella, P., Glass, I. I., and Deschambault, R. L., "A Numerical Study of Oblique Shock-Wave Reflections with Experimental Comparisons," Proceedings of the Royal Society of London, A 398, 1985, pp. 117-140.

68. Harten, A., Engquist, B., Osher, S., and Chakravarthy, S., "Uniformly High Order Accurate Essentially Non-Oscillatory Schemes. III," Journal of Computational Physics, vol. 71, pp. 231-303, 1987.

69. Jiang, G. S. and Shu, C. W., "Efficient Implementation of Weighted ENO Schemes," Journal of Computational Physics, vol. 126, 1996, pp. 202-228.

70. Ofengeim, D. K., and Drikakis, D., "Simulation of Blast Wave Propagation over a Cylinder," Shock Waves, vol. 7, 1997, pp. 305-317.

71. Jiang, Z., Takayama, K., Moosad, K. P. B., Onodera, O., and Sun, M., "Numerical and Experimental Study of a Micro-Blast Wave Generated by Pulsed-Laser Beamfocusing," Shock Waves, vol. 8, 1998, pp. 337-349.

72. Liang, S. M., Hsu, J. L., and Wang, J. S., "Numerical Study of Cylindrical Blast-Wave Propagation and Reflection," AIAA Journal, vol. 39, 2001, pp. 1152-1158.

73. Liang, S. M. and Weng, K. C., "Numerical Study of Blast-Wave Propagation in a Double-Bent Duct," AIAA Journal, vol. 40, 2002, pp. 1796-1802.

74. Flaherty, J.E., Krivodonova, L., Remacle, J.F., and Shephard, M.S., "Aspects of Discontinuous Galerkin Methods for Hyperbolic Conservation Laws," Finite Elements in Analysis and Design, vol. 38, pp. 889-908, 2002.

75. Cler, D., Chevaugeon, N, Shephard, M S, and Remacle, J F, "CFD Application to Gun Muzzle Blast - A Validation Case Study," 41st AIAA Aerospace Sciences Meeting & Exhibit, Reno, NV, 2003, AIAA Paper 2003-1142.

76. Nurick, G. N. and Shave, G. C., "The Deformation and Tearing of Thin Square Plates Subjected to Impulsive Loads - An Experimental Study," *International Journal of Impact Engineering*, vol. 18, 1996, pp. 99-116.

77. Nurick, G. N., Gelman, M. E., and Marshall, N. S., "Tearing of Blast Loaded Plates with Clamped Boundary Conditions," *International Journal of Impact Engineering*, Vol. 18, 1996, pp. 803-827.

78. Wierzbicki, T. and Nurick, G. N., "Large Deformation of Thin Plates Under Localised Impulsive Loading," *International Journal of Impact Engineering*, Vol. 18, 1996, pp. 899-918.

79. Bland, S. M. And Kapania, R. K., "Transient Geometrically Nonlinear Analysis of Polar Orthotropic Circular Plates using the Rayleich-Ritz Method," 45th AIAA/ASME/ASCE/AHS/ASC Structures, Structural Dynamics and Materials Conference, Palm Springs, CA, April 2004.

80. Liu, D. and Stronge, W. J., "Shear and Bending Deformation of Rigid-Plastic Circular Plates by Central Pressure Pulse," *International Journal of Impact Engineering*, Vol. 18, 1996, pp. 383-402.

81. Turkmen, H. S., "Structural Response of Isotropic Plates Subject to Blast Loading," Advances in Computational Structural Mechanics, Civil-Comp Press, Edinburgh, 1998, pp. 101-107.

82. Chock, J. M. K. And Kapania, R. K., "Load Updating for Finite Element Models," AIAA Journal, Vol 41, No. 9, September 2003, pp. 1667-1673.

83. Turkmen, H. S. and Mecitoglu, Z., "Nonlinear Structural Response of Laminated Composite Plates Subjected to Blast Loading," AIAA Journal, vol. 37, 1999, pp. 1639-1647.

84. Jacinto, A. C., Ambrosini, R. D., and Danesi, R. F., “Experimental and Computational Analysis of Plates Under Airblast Loading,” International Journal of Impact Engineering, vol. 25, 2001, pp. 927-947.

85. Ramajeyathilagam, K., Vendhan, C. P., and Rao, V. B., “Non-Linear Transient Dynamic Response of Rectangular Plates Under Shock Loading,” International Journal of Impact Engineering, vol. 24, 2000, pp. 999-1015.

86. Wu, H. Y. T. and Chang, F. K., “Transient Dynamic Analysis of Laminated Composite Plates Subjected to Transverse Impact,” Computers & Structures, vol. 31, 1989, pp. 453-466.

87. Zhu, L., “Transient Deformation Modes of Square Plate Subjected to Explosive Loading,” International Journal of Solids and Structures, vol. 33, 1996, pp. 301-314.

88. Louca, L. A. and Harding, J. E., “Non-Linear Analysis of Imperfect Plates Under Transient Lateral Pressure Loading,” Computers & Structures, vol. 63, 1997, pp. 27-37.

89. Louca, L. A. and Pan, Y. G., “Response of Stiffened and Unstiffened Plates Subjected to Blast Loading,” Engineering Structures, vol. 20, 1998, pp. 1079-1086.

90. Rudrapatna, N. S., Vaziri, R., and Olson, M. D., “Deformation and Failure of Blast-Loaded Square Plate,” International Journal of Impact Engineering, vol. 22, 1999, pp. 449-467.

91. Yakupov, R. G., "Plastic Strains in a Cylindrical Shell Under the Effect of a Spherical Blast Wave," *Strength of Materials*, vol. 14, 1982, pp. 52-56.

92. Salvatorelli-D'Angelo, F., "Dynamic Response and Failure of Single and Sandwich Cylindrical Shells Under Lateral Blast Loading," *Structures Under Shock and Impact*, Bulson P. S., ed., Elsevier, Amsterdam, 1989, pp. 381-395.

93. Wierzbicki, T. and Hoo Fatt, M. S., "Damage Assessment of Cylinders Due to Impact and Explosive Loading," *International Journal of Impact Engineering*, vol. 13, 1993, pp. 215-241.

94. Hoo Fatt, M. S., "Rigid-Plastic Deformation of a Ring-Stiffened Shell Under Blast Loading," *Journal of Pressure Vessel Technology*, vol. 119, 1997, pp. 467-474.

95. Redekop, D., "Dynamic Response of a Toroidal Shell Panel to Blast Loading," *Computers & Structures*, vol. 51, 1994, pp. 235-239.

96. Mohan, P. and Kapania, R. K., “Analysis of General Shells Under Deformation Dependent Loads Using a Flat Triangular Shell Element,” Proceedings of the 39th AIAA/ASME/ASCE/AHS/ASC Structures, Structural Dynamics and Materials Conference, April 1998, AIAA-98-1764.

97. Gangadhara Prusty, B., and Satsangi, S. K., “Finite Element Transient Dynamic Analysis of Laminated Stiffened Shells,” Journal of Sound and Vibration, vol. 248, 2001, pp. 215-233.

98. Koh, C. G., Ang, K. K., and Chan, P. F., “Dynamic Analysis of Shell Structures with Application to Blast Resistant Doors,” Shock and Vibration, vol. 10, 2003, pp. 269-279.

99. Jenkins, C. H. and Leonard, J. W., "Nonlinear Dynamic Response of Membranes: State of the Art," *Applied Mechanics Reviews*, Vol. 44, 1991, pp. 319-328.

100. Naik, N. K., *Woven Fabric Composites*, Technomic, Lancaster, PA, 1994.

101. Portanova, M. A., *Evaluation of the Impact Response of Textile Composites,* NASA Contractor Report 198265, Langley Research Center, Hampton, VA, 1995.

102. Suherman, S., *A Survey of Research on the Behavior and Mechanical Properties of Textile Composites*, Report No. CE/VPI-ST 96/8, Department of Civil Engineering, Virginia Polytechnic Institute and State University, Blacksburg, VA, 1996.

103. Cox, B. N. and Flanagan, G., *Handbook of Analytical Methods for Textile Composites*, NASA Contractor Report 4750, Langley Research Center, Hampton, VA, 1997.

104. Farrar, C. L., "Impact Response of a Circular Membrane," *Experimental Mechanics*, vol. 24, 1984, pp. 144-149.

105. Ghosh, S. K., Reid, S. R. and Johnson, W., "The Large Deflection Impulsive Loading of Clamped Circular Membranes," *Structural Impact and Crashworthiness*, vol. 2, J. Morton, ed., Elsevier, London, 1984, pp. 471-481.

106. Mutallimov, S. M., "Transverse Impact by a Cone on an Elastic Membrane Accompanied by Destruction of the Membrane," *Soviet Applied Mechanics*, vol. 21, 1985, pp. 959-964.

107. Nuriev, B. R., "Distribution of Plastic Strains in a Membrane Subjected to Transverse Impact," *Soviet Applied Mechanics*, vol. 12, 1991, pp. 1201-1206.

108. Haddow, J. B., Wegner, J. L. and Jiang, L., "The Dynamic Response of a Stretched Circular Hyperelastic Membrane Subjected to Normal Impact," *Wave Motion*, vol. 16, 1992, pp. 137-150.

109. Tait, R. J. and Zhong, J. L., "An Impact Problem for a Non-Linear Elastic Membrane with Nonconstant Boundary Conditions," *Zeitschrift für angewandte Mathematik und Mechanik*, vol. 75, 1995, pp. 605-613.

110. Tabarrok, B. and Qin, Z., "Dynamic Analysis of Tension Structures," *Computers & Structures*, vol. 62, 1997, pp. 467-474.

111. Bonet, J., Wood, R. D., Mahaney, J., and Heywood, P., "Finite Element Analysis of Air Supported Membrane Structures," Computer Methods in Applied Mechanics and Engineering, vol. 190, 2000, pp. 579-595.

112. Stanuszek, M., "FE Analysis of Large Deformation of Membranes with Wrinkling," Finite Elements in Analysis and Design, vol. 39, 2003, pp. 599-618.

113. Blom, F. J., "A Monolithical Fluid-Structure Interaction Algorithm Applied to the Piston Problem," Computer Methods in Applied Mechanics and Engineering, vol. 167, 1998, pp. 369-391.

114. Pranata, B. B., Hounjet, M. H. L. and Zwaan, R. J., "Thin layer Navier Stokes Solver and its Application for Aeroelastic Analysis of an Airfoil in Transonic Flow," International Forum on Aeroelasticity and Structural Dynamics, Manchester, UK, 1995.

115. Piperno, S., "Staggered Time-Integration Methods for a One-Dimensional Euler Aeroelastic Problem, Rapport de Recherche, CERMICS 94-33, Sophia-Antipolis, Fr, 1994.

116. Blom, F. J. and Leyland, P., "Analysis of Fluid-Structure Interaction on Moving Airfoils by Means of an Improved ALE-Method, AIAA paper 97-1770, 1997.

117. Blom, F. J. and Leyland, P., "Analysis of Fluid-Structure Interaction by Means of Dynamic Unstructured Meshes," in Proceedings of 4th international symposium on fluid-structure interaction, Aeroelasticity, Flow-Induced Vibrations and Noise, ASME, Dallas, 1997, pp. 3-10.

118. Piperno, S., Farhat, C., and Larrouturou, B., "Partitioned Procedures for the Transient Solutions of Coupled Aeroelastic Problems. Part I: Model Problem and Two-Dimensional Application, Computer Methods in Applied Mechanics and Engineering, vol. 124, 1995, pp. 79-112.

119. Paranta, B. B., and Hounjet, M. H. L., "Large Time Step Aero-Structural Coupling Procedures for Aeroelastic Simulation," Proceedings of 1997 International Forum on Aeroelasticity and Structural Dynamics, vol. II, AIDAA. Rome, 1997, pp. 63-70.

120. Giles, M. B., "Stability and Accuracy of Numerical Boundary Conditions in Aeroelastic Analysis," International Journal for Numerical Methods in Fluids, vol. 24, 1997, pp. 739-757.

121. He, L., "Integration of 2-D Fluid/Structure Coupled System for Calculations of Turbomachinery Aerodynamic/Aeroelastic Instabilities," International Journal of Computational Fluid Dynamics, vol. 3, 1994, pp. 217-231.

122. Alonso, J. J., and Jameson, A., "Fully-Implicit Time-Marching Aeroelastic Solutions," AIAA Paper 94-0056, 1994.

123. Melville, R. B., Morton, S. A., and Rizzetta, D. P., "Implementation of a Fully-Implicit Aeroelastic Navier-Stokes Solutions on Deforming Meshes," AIAA Paper 97-1085, 1997.

124. Schafer, M. and Teschauer, I., "Numerical Simulation of Coupled Fluid-Solid Problems," Computer Methods in Applied Mechanics and Engineering, vol. 190, 2001, pp. 3645-3667.

125. Souli, M., Ouahsine, A., and Lewin, L., "Arbitrary Largrangian Eulerian Formulation for Fluid-Structure Interaction Problems," Computer Methods in Applied Mechanics and Engineering, vol. 190, 2000, pp. 659-675.

126. Chapelle, D. and Bathe, K. J., *The Finite Element Analysis of Shells – Fundamentals*, Springer-Verlag, Berlin, 2003.

127. Zienkiewicz, O. C. and Taylor, R. L., *Finite Element Method - Solid Mechanics*, 5th edition, vol. 2, McGraw Hill, 2000.

128. Allman, D.J., "Evaluation of the Constant Strain Triangle with Drilling Rotations," International Journal for Numerical Methods in Engineering, vol. 26, 1988, pp. 2645-2655.

129. Cook, R. D., "Further Development of a Three Node Triangular Shell Element," International Journal for Numerical Methods in Engineering, vol. 36, 1993, pp. 1413-1425.

130. Dhatt, G., Marcotte, L., and Matte, Y., "A New Triangular Discrete Kirchhoff Plate/Shell Element," International Journal for Numerical Methods in Engineering, vol. 23, 1986, pp. 453-470.

131. Allman, D. J., "A Basic Flat Facet Finite Element for the Analysis of General Shell," International Journal for Numerical Methods in Engineering, vol. 37, 1994, pp. 19-35.

132. Mohan, P., “Development and Application of a Flat Triangular Element for Thin Laminated Shells,” Ph.D. Dissertation, Aerospace Engineering, Virginia Tech, 1997.

133. Nour-Omid, B. and Rankin, C. C., "Finite Rotation Analysis and Consistent Linearization Using Projectors,” Computer Methods in Applied Mechanics and Engineering, vol. 93, 1991, pp. 353-384.

134. ANSYS Release 8.0 Documentation, SAS IP, Inc., 2003.

135. Newmark, N. M., “A Method of Computation for Structural Dynamics,” *Journal of the Engineering Mechanics Div.*, ASCE, Vol. 85, No. EM3, pp. 67-94.

136. Tessler, A., Sleight, D. W., and Wang, J. T., “Nonlinear Shell Modeling of Thin Membranes with Emphasis on Structural Wrinkling,” Proceedings of 44*th* AIAA/ASME/ASCE/AHS Structures, Structural Dynamics, and Materials Conference, Norfolk, VA, April 2003.

137. Scherbatiuk, K. D., “Effect of a Flexural Membrane on Blast Transmission and Mitigation,” Proceedings of Response of Structures to Extreme Loading Conference, Toronto, Canada, August 3-6, 2003.

138. Meyer, R. F., “The Impact of a Shock Wave on a Movable Wall,” Journal of Fluid Mechanics, vol. 3, 1958, pp. 309-323.

139. Chun S., Kapoor H., Kapania R. K., Motley M. R., and Plaut R. H., “Modeling the Response of Collective Protection Systems to Airblasts,” VPI-AOE-290 Report to U.S. Air Force Research Laboratory, Tyndall Air Force Base, Florida, June 2004.

140. Beshara, F. B. A., "Model of Blast Loading on Aboveground Structures - II. Internal Blast and Ground Shock," Computers & Structures vol. 51, no. 5, pp. 597-606, 1994.

141. Hammons, M. I., "Antiterrorism/Force Protection Criteria Validation Test," Quick Look Report for Air Force Civil Engineer Support Agency, March 2000.

142. Knox, K. J., Donovan, P. T., Dass, W. C., and Hammons, M. I., "Explosive Tests on Lightweight, Deployable Shelters," Final Report for The U.S. Air Force–Force Protection Battlelab, December 1998.

143. Anderson, J.D., *Modern Compressible Flow with Historical Perspective*, 2nd edition, McGraw-Hill, New York, 1990.

144. Karamcheti, K., *Principles of Ideal-Fluid Aerodynamics*, Krieger, Malabar, FL, 1980.

145. Patankar, S.V., *Numerical Heat Transfer and Fluid Flow*, Hemisphere, New York, 1980.

146. Anderson, D.A., Tannehill, J.C., and Pletcher, R.H., *Computational Fluid Mechanics and Heat Transfer*, Taylor and Francis, Bristol, PA, 1984.

147. Ferzinger, J.H. and Peric, M., *Computational Methods for Fluid Dynamics*, Springer, Berlin, 1997.

Vita

Saneon Chun was born on May 4, 1970 in Pusan, Korea. He received a Bachelor of Science in Aerospace Engineering in 1993, from Pusan National University. He graduated in 1995 with an M.S. degree in Aerospace Engineering with a specialty in Computational Fluid Dynamics from Pusan National University. He had worked as a research engineer for 5 years in aerospace industry like Daewoo Heavy Industries, Ltd and Korea Aerospace Industries, Ltd. He began his Ph.D. degree at Virginia Tech in the fall of 2000. During his time at Virginia Tech, he was involved in research topics and projects such as (i) Spanload Optimization for Minimum Induced Drag in Formation Flight, (ii) Structural Wing Design and Weight Optimization, (iii) Hybrid Genetic Algorithms for Inverse Problems in Optical Medical Imaging, and (iv) Blast Wave Loading and Fluid-Structure Interaction of a Flexible Structure using CFD & CSD. Upon completion of his doctoral studies, he palns to perform academic and industrial research.